

Jorge Rafael Nogueira Raposo

EXTREME FIRE BEHAVIOUR ASSOCIATED WITH THE MERGING OF TWO LINEAR FIRE FRONTS

Doctoral Thesis in Mechanical Engineering - Natural and Technological Hazards, supervised by Professor Domingos Xavier Filomeno Carlos Viegas and Doctor Miguel Abrantes de Figueiredo Bernardo de Almeida, submitted to the Department of Mechanical Engineering, Faculty of Sciences and Technology of the University of Coimbra

April, 2016



UNIVERSIDADE DE COIMBRA



Extreme Fire Behaviour Associated with the Merging of Two Linear Fire Fronts

A dissertation submitted to the Department of Mechanical Engineering of the
University of Coimbra in partial fulfilment to the requirements for
degree of Doctor of Philosophy in Mechanical Engineering

Jorge Rafael Nogueira Raposo

Scientific advisers:

Prof. **Domingos Xavier Filomeno Carlos Viegas**, University of Coimbra, Portugal

Doctor **Miguel Abrantes de Figueiredo Bernardo de Almeida**, University of Coimbra, Portugal

Department of Mechanical Engineering
Faculty of Sciences and Technology
University of Coimbra

Coimbra, April 2016

To Catarina and my family

“Start doing what is necessary, then do what is possible, and suddenly you are doing the impossible.”

St. Francis of Assisi

Acknowledgements

The research work present in this PhD thesis has been carried out in the last four years at the Association for Development of Industrial Aerodynamics (ADAI). These four years of research were a very fruitful period in my engineering education, as well as in my personal development. The freedom in the investigation accompanied by a wise guidance of my scientific advisers allowed me to improve the knowledge in the field of forest fire behaviour in particular the problem of the junction fires.

I particularly wish to express my sincere gratitude to my scientific advisers Professor Domingos Xavier Filomeno Carlos Viegas and Doctor Miguel Abrantes de Figueiredo Bernardo de Almeida, for the valuable guidance, support and consistent encouragement during my PhD thesis. I highly appreciate their outstanding scientific expertise and experience (shared with me), as well as the trust and incessant care to provide me with the best possible working conditions. Their drive for scientific rigor have been indispensable to the successful conclusion of this thesis and, at the same time, a great source of inspiration for me. I also want to express my appreciation for the effort expended in this work and for the critical and suggestive reading of the text.

I would like to express my thanks to Professor Rui Figueiredo for the fruitful discussions and critical remarks concerning the heat transfer mechanisms his expertise, insightful comments and suggestions on the research direction were crucial for the fulfilment of this part of the work.

I also would like to express my thanks to Professor Jorge André for the availability, the precious teachings about the statistical analyses as well insightful comments of the work.

My thank you to my colleague Xiaodong for the insights about laboratorial research, measurement techniques as well as for his friendship. To Leonardo Rocha by the help in the numerical implementation of the code for the radiation calculation.

I am grateful for the excellent support given within the ADAI chaired by Professor Domingos Xavier Viegas and the opportunity that was given to me to develop my research work, as well as the financial support. I also wish to thank all members of ADAI for the friendly and scientifically inspiring atmosphere at the research centre. In special I would like to thank my colleagues/friends that worked with me in ADAI, Eng. Teresa Viegas, Luis Mário Ribeiro, Nuno Luis, Ricardo Oliveira, Joel Teixeira, Sérgio Lopes, Xiaodong Xie, Fátima Guedes, Ana Rosa, Joana Cardoso, António Trindade and António Cardoso.

To my friends of the university in particular Luís Reis and Diogo Neto who helped me in carrying out this work and also to Bruno Ferreira, Diogo Emídio, Henrique Santos, Álvaro Mendes, Pedro Barros, Eduardo Cardoso, Pedro Correia and Vasco Simões for their friendship and the many inspiring (scientific and several non-scientific) discussions we had. I wish to thank all my friends for their encouragement.

To my dear fiancé Catarina for her love, dreams, sweetness and happiness that she always gives to me and also her patience; to my family for the affection and support they gave me, in particular to my wise and sweet parents (David Raposo and Ana Isabel Raposo) that always supported me, my grandfather (José Nogueira), my nephew (Bernardo Raposo) and my brother (Hugo Raposo) that incentivise me to choose Mechanical Engineering course. To my cousin (Nuno Carvalho) and my grandmother (Júlia Raposo) who have passed way. I want to say thank to all of them for the already referred reasons and for their encouragement, personal sacrifice and understanding through these years. Without them it would not be possible to finish this work. As I am a man of faith I thank God for all the opportunities that always gives me.

The financial support of this work has been provided by the Portuguese Foundation for Science and Technology (FCT) through the PhD Grant SFRH/BD/85557/2012, which is greatly acknowledged.

Coimbra, April 2016



Abstract

In this work the concept of extreme forest fire behaviour denominated as Junction Fire is analysed. The junction fire consists in the interaction between two linear fire fronts which in their propagation intersect at a single point making a small angle between them. In their merging process, the phenomena of heat transfer by radiation and convection are extremely enlarged due to the concentration of energy at the intersection point. The concentration of energy and consequently the development of the strong heat transfer mechanism induce an extremely high and sudden increase of the rate of spread value of the intersection point until it reaches a maximum value after which the rate of spread starts to decrease. This maximum values of the rate of spread is among highest ever measured; this can create serious safety and management problems to those dealing with this type of forest fires.

The research program addressed the problem of the junction fires taking into account the essential parameters that affect the pattern of behaviour of this type of extreme fire behaviour. These parameters are the initial angle between the fire fronts θ_0 , the angle of slope of the fuel bed α and the kind of fuel burned. The fuels used in this study were dead pine needles of *Pinus pinaster*, shrubs composed by a mixture of *Erica umbelatta*, *Erica australis*, *Ulex minor e Chamaespartium tridentatum* and straw of *Avena sativa*. The fuel load was kept constant in the value of 0.6 kg.m^{-2} , which is widely used in this type of research programs once it is easily extrapolated to the fuel load found in the forests.

The analysis of Junction Fire was made in the laboratory facilities of ADAI in Lousã in centre of Portugal, but also other scales were tested to validate the results obtained at different scales; to achieve this experimental fires with merging fire fronts were performed in the shrubs fields of ADAI, in the mountain of Lousã recreating the conditions for the

occurrence of junction fires. In these experiments it was noticed that the junction fires are a source of instability that conducts to the occurrence of fire whirls. The average scale of the experiments performed in the field is around ten times greater than the laboratory experiments.

The results of the laboratory and field tests are finally compared with a real occurrence of a junction fire in Canberra, Australia, in 2003 where two massive fires merged creating a tongue of fire between them with an extremely high rate of spread which destroyed the surroundings of Canberra. In these events the occurrence of a fire whirl due to junction fire phenomena was registered as well.

During the research program it was realised that the junction fire is very similar to an eruptive fire with the particularity that the rate of spread did not increase indefinitely. Contrary to the eruptive fires after reaching the peak value that is dependent on the initial angle between the fire fronts θ_0 and of the slope angle, junction fires start a decreasing phase. For this reason the initial acceleration phase is modelled using the eruptive fire model. Like in the eruptive fires in canyons the junction fire acceleration is attributed to the flow generated by the fire which creates extremely high rates of spread. During the evolution of the fire the initial conditions are shifted especial the angle between the fire fronts that tend to increase until the limit of creating a single straight line fire front. In this process the convection/flow loses its primacy and the behaviour of the fire starts to be ruled by the radiative process that has decreasing trends, thus explaining the deceleration of the fire.

Finally an empirical model to estimate the main parameters of jump fires and to predict their evolution in the course of space and time is proposed. The main properties of the model are presented in non-dimensional form to generalize its formulation as a function of the parameters that govern junction fires in the range covered by the present work.

Keywords: junction fire, fire behaviour, merging fire , dynamic effect , fire modelling, forest fires.

Resumo

Neste trabalho é analisado o conceito de comportamento extremo fogo denominado como fogo de junção. O fogo de junção consiste na interação entre duas frentes de fogo lineares que, na sua propagação, convergem num único ponto, formando um pequeno ângulo entre si. Neste processo de convergência os fenômenos de transferência de calor por radiação e convecção desenvolvem-se de forma extrema, devido à concentração de energia no ponto de convergência. A concentração de energia e consequentes mecanismos de transferência de calor induzem uma variação da velocidade de propagação, extremamente elevada e repentina, do ponto de encontro entre as duas frentes de fogo, até que seja atingido o valor máximo. Depois do valor máximo ser atingido a velocidade de propagação começa a decrescer. Os valores máximos da velocidade de propagação são os mais elevados alguma vez medidos nos estudos desenvolvidos pela nossa equipa. Este fenómeno de comportamento extremo do fogo pode causar sérios problemas de gestão de meios e de segurança pessoal ou coletiva daqueles que lidam com este tipo de incêndios florestais.

No programa de investigação desenvolvido é abordado o problema dos fogos de junção tendo em conta os parâmetros essenciais que afetam o padrão de comportamento deste tipo de fenómeno extremo de fogo. Os parâmetros que condicionam o desenvolvimento do fogo de junção são o ângulo inicial entre as duas frentes de fogo θ_0 , o ângulo de declive do leito de combustível α , e o tipo de combustível florestal. Os combustíveis utilizados neste estudo foram a caruma de *Pinus pinaster*, palha de *Avena sativa* e mato constituído essencialmente por ramos de *Erica umbellata*, *Erica australis*, *Ulex minor* e *Chamaespartium tridentatum*. A carga de combustível manteve-se constante, com o valor de 0.6 kg.m^{-2} , o qual é vulgarmente usado neste tipo de ensaios, uma vez que corresponde a

uma carga que facilmente pode ser extrapolada e comparada com a carga de combustível encontrado nas florestas.

O estudo experimental do fogo salto realizou-se, na sua maioria, no Laboratório de Estudos sobre Incêndios Florestais (LEIF) da ADAI, na Lousã. Contudo outras escalas foram testadas para validar os resultados obtidos. Para tal, ensaios de campo experimentais com encontro de frentes de fogo foram realizadas no campo de testes da ADAI, na serra da Lousã, recriando as condições necessárias à ocorrência de fogos de junção. Durante estes ensaios de campo experimentais observou-se que, os fogos de junção são uma fonte de instabilidade que, conduzem à ocorrência de turbilhões de fogo. A dimensão média dos ensaios de campo foi cerca de dez vezes superior à dos ensaios de laboratório.

Os resultados obtidos através dos ensaios de laboratório e de campo foram comparados com um incêndio no qual ocorreu o comportamento de fogo de junção, em *Canberra*, Austrália, 2003, onde dois grandes incêndios encontraram-se criando uma língua de fogo entre eles com uma velocidade de propagação muito alta que destruiu os subúrbios da cidade de *Canberra*. Neste grande incêndio foi registado e documentado a ocorrência de um turbilhão de fogo com origem na junção das frentes de fogo.

Durante o programa investigação realizado percebeu-se que o comportamento do fogo de junção é muito semelhante ao comportamento de fogo eruptivo, com a particularidade de que a sua velocidade de propagação não aumentou indefinidamente. Contrariamente ao que acontece nos fogos eruptivos, depois de atingir o valor máximo da velocidade de propagação, que é dependente do ângulo inicial entre as frentes de fogo θ_0 e do ângulo de declive α , os fogos de junção manifestam uma fase decrescente da velocidade de propagação. Por esta razão, apenas a fase de aceleração inicial foi modelada recorrendo ao modelo de comportamento eruptivo do fogo. Tal como nos fogos eruptivos, em *canyons*, a aceleração do fogo de junção é atribuída ao escoamento convectivo induzido pelo fogo que conduz a velocidades de propagação muito elevadas. Durante a evolução dos fogos de junção as condições iniciais alteram-se rapidamente especialmente o ângulo formado entre as frentes de fogo, que tendem a aumentar até se tornarem numa única frente de fogo linear. Neste processo os fenómenos convectivos perdem a predominância inicial e o comportamento do fogo começa a ser governado por processos radiativos, que tendem também a diminuir a taxa de transferência de calor à medida que o ângulo entre as frentes

aumenta, o que explica a desaceleração do fogo. A fase final de desaceleração foi simulada através de modelos radiativos.

Finalmente é proposto um modelo empírico para a estimação da evolução do fogo de junção ao longo do espaço e do tempo. O modelo faz uso da análise não-dimensional o que possibilita a sua aplicação aos diferentes casos com inerentes diferentes parâmetros iniciais que influenciam o comportamento dos fogos de junção estudados no presente trabalho e sua posterior generalização.

Palavras-chave: fogo de junção, comportamento do fogo, encontro de frentes, comportamento dinâmico, modelação do fogo, incêndios florestais.

Contents

Acknowledgements	iii
Abstract	v
Resumo	vii
Contents	xi
List of Figures	xiii
List of Tables.....	xvii
Acronyms and Symbology	xviii
Acronyms	xviii
Symbology.....	xviii
Chapter 1. General Introduction.....	1
1.1. Background and Motivation.....	1
1.2. Objectives and Achievements	3
1.3. Thesis Outline	4
Chapter 2. Junction Fires.....	7
2.1. Fundamental concepts.....	7
2.1.1. Notion of junction fire.....	7
2.1.2. Heat transfer mechanisms	14
2.2. Physical Modelling	17
2.2.1. Energy concentration concept	17
2.2.2. Convection Processes	24
2.2.3. Radiation Processes.....	25
Chapter 3. Methodology.....	31
3.1. Experimental Analysis	31
3.2. Laboratory Experiments.....	31
3.3. Field Experiments	42
3.4. Real Fire.....	44
3.5. Measurement of Radiative heat flux	45
3.6. Parameters of experimental tests.....	46
Chapter 4. Results and Discussion	49
4.1. Fire Front Evolution.....	49
4.1.1. Overall evolution.....	49
4.1.2. Fire Line Rotation	53
4.1.3. Evolution of intersection point	56
4.2. Role of Slope	58
4.3. Role of Fuel	60
4.4. Role of initial angle between the fire fronts	63

4.5.	Scale effect.....	65
4.6.	Acceleration phase.....	67
4.7.	Deceleration phase.....	72
4.8.	Predictive Mathematical Models	76
4.8.1.	Maximum ROS (R_M) analysis	76
4.8.2.	Time t'_M taken until R_M is reached	84
4.8.3.	Distance x'_M until R'_M is reached	86
4.8.4.	Analytical Model Formulation	88
4.9.	General discussion	99
Chapter 5.	Conclusion.....	103
References	105

List of Figures

Figure 2.1: Evolution of McIntyres Hut and Bendora fires on the 18 th January between 15.00h and 15.45h. Plates from Cheney report.	9
Figure 2.2: Schematic representation of the tests performed with the basic parameters.	9
Figure 2.3: Rate of spread R_D as a function of the distance in case a) and as a function of time in b) for tests with shrubs, including laboratory, field and a real case.	12
Figure 2.4: Schematic view of the geometry of two oblique fire lines in symmetrical conditions. The dotted lines in this figure correspond to the limits of the energy distribution.	18
Figure 2.5: a) Representation of axis Y_1 crossing the fire line. b) Conceptual sketch of the variation of energy density along the axis perpendicular to fire line L_1 . The parameter d is a reference length of the order of the flame depth.....	20
Figure 2.6: Simplified model of energy density variation along axis Y_1	22
Figure 2.7: Simplified model of energy density variation along axis Y_2	23
Figure 2.8: Non dimensional energy in the control area as a function of the angle between the fire lines evaluated using the present model for values of $\theta > 5^\circ$. The curves show the contributions E_1 and E_2 of L_1 , of L_2 respectively and the total energy E_T	24
Figure 2.9: Schematic representation of the calculus of the radiative heat flux.	27
Figure 2.10: Evolution of the incident radiative heat flux q as a function of the angle θ between the flames for the three fuels considered in the present study.	29
Figure 3.1: photo of the Canyon Table DE4.....	32
Figure 3.2: Preparation of the tests.	33
Figure 3.3: Moisture analyser A&D ML50.	34
Figure 3.4: Example of measurement of the residence time t_0	35
Figure 3.5: General view of Combustion Table DE4 during the preparation and the performance of test CF63. (a) Reference image before the test. The Pitot tubes can be seen on the left side of the table. (b) At ignition: t=0s; (c) t=2s; (d) t=18s.....	37
Figure 3.6: System of 25 K type thermocouples.	38
Figure 3.7: Infrared Camera.	38
Figure 3.8: Infrared frames from a junction fire test. CF 01 (30°, 30°) PP. The time between frames is of 4s.	39
Figure 3.9: Determination of the basic rate of spread R_0 in a fuel bed of pine needles.	40

Figure 3.10: linear relation between The value of the flow speed and the squared root of the signal, in voltage, of the pressure transducers.	41
Figure 3.11: Photography of the pitot tubes and schematic representation.	42
Figure 3.12: Overview of Gestosa field experiments in 2012. (a) General view (b) Dimensions of the plots.	43
Figure 3.13: Ignition of the two fire fronts along their entire length with the pyrotechnic system in the field.	43
Figure 3.14: Digital photos in the experimental tests in the field of junction fires with formation of firewhirls.	44
Figure 3.15: 18th January 2003, Junction fire phenomenon between the flanks of Bendora and McIntyres large fires. Schematic view of Canberra 2003 fires (Adapted from Cheney (2005))	45
Figure 3.16: Bench test with the black heat plates.	45
Figure 4.1. Evolution of the fire perimeter according to data obtained with IR images: Tests (a) CF 05 PP ($\alpha=0^\circ$); (a) CF 44 PP ($\alpha=20^\circ$) (c) CF 01 PP ($\alpha=30^\circ$). With the angle θ_0 fixed in the value of 30° The time corresponding to each perimeter line is indicated in the figure.	50
Figure 4.2: Evolution of the fire perimeter according to the images obtained with IR camera for tests with $\theta_0=30^\circ$ and $\alpha = 30^\circ$. (a) CF 70 PP ; (b) CF 38 ST ; (c) CF 50 SH . The time corresponding to each perimeter is indicated on figure.	51
Figure 4.3: Evolution of the fire perimeter according to the images obtained with IR camera for tests with $\alpha=0^\circ$ and θ_0 changing from 10 to 20° , 30° and 45° . The time corresponding to each perimeter is indicated in the figures.	52
Figure 4.4: Fire line perimeters plots at laboratory scale and at field scale for $\alpha=30^\circ$ and $\theta_0=30^\circ$ with fuel SH.	53
Figure 4.5: The evolution of the instantaneous angle between the fire fronts θ as a function of the time for the three fuels (PP, ST and SH). Case a) with a slope angle $\alpha=0^\circ$; Case b) Case a) with a slope angle $\alpha=30^\circ$	54
Figure 4.6: Schematic representation of the angle β that represents the average angle between the fire fronts and the OY axis.	55
Figure 4.7: Variation of the reference rotational velocity ω' of the fire lines as a function of the inclination angle β , for the three fuels. Data points corresponding to tests with PP fuel beds with various values of slope angle are marked with lines.	56
Figure 4.8 Comparison between the evolution of displacement distance x_D as a function of time measured by IR and by TC techniques for tests with PP fuel bed for three different fuel bed slopes, a) 0° of slope, b) 20° of slope and c) 30° of slope. With fix value of initial angle of the fire fronts $\theta_0 = 30^\circ$	57
Figure 4.9 Characteristic curves showing the evolution of the non-dimensional rate of spread of junction fire PP fuel bed for three different fuel bed slopes, a) 0° of slope, b) 20° of slope and c) 30° of slope. With fix value of initial angle of the fire fronts $\theta_0 = 30^\circ$	58
Figure 4.10: Evolution of the values of R_D for three different fuels and slope values as a function of time and (● PP; ■ ST; ▲ SH)	59
Figure 4.11: Evolution of the values of R_D for three different fuels and slope values as a function of distance. (● PP; ■ ST; ▲ SH)	60
Figure 4.12: Non-dimensional rate of spread R' as function of non-dimensional time t' , for the three different fuels with the initial angle between the fire fronts θ_0 of 30° and the value of the angle of slope α varies, from 0° in a), 20° in b) and 30° in c).	62
Figure 4.13: Non-dimensional rate of spread R'_2 as function of non-dimensional time t' , for the three different fuels with the initial angle between the fire fronts θ_0 of 30° and the value of angle of slope α varies, from 0° in a), 20° in b) and 30° in c).	62

Figure 4.14: Non-dimensional rate of spread $R^*=R_D/R_{DM}$ as function of non-dimensional time $t^*=t/t_M$, for the three different fuels with the initial angle between the fire fronts θ_o of 30° and the value of angle of slope α varies, from 0° in a), 20° in b) and 30° in c).....	63
Figure 4.15: Rate of spread R_D as function of the initial angle between the fire fronts θ_o , for different conditions of slope angle, a) 0° , b) 10° , c) 20° , d) 30° and e) 40° . All the experiments are performed with PP	64
Figure 4.16: Rate of spread R_D as function of the distance (a) and as function of time (b) for tests with shrubs, including laboratory, field and a real case.	65
Figure 4.17: Evolution of R'_M in non-dimensional form for test with shrub vegetation at laboratory, field and real fire scales (a) as a function of t^* and (b) as a function of x^*	67
Figure 4.18: Evolution of the non-dimensional ROS R' as a function of t' during the acceleration phase for some tests. The full line corresponds to the eruptive model of Viegas (2006) for PP fuel beds. ...	68
Figure 4.19: Convective flows in junction fires for different angles between the fire fronts in the course of time.....	69
Figure 4.20: Flow velocity measured at each Pitot tube as a function of the distance $s_F=x_D-x_i$ between the fire front and the Pitot tube position for tests with PP for: (a) $\alpha=0^\circ$, (b) $\alpha=20^\circ$, (c) $\alpha=30^\circ$ and (d) $\alpha=40^\circ$	70
Figure 4.21: Flow velocity U^* measured when the fire front passed by the Pitot tube as a function of the relative distance in relation to the position x_i/x_M . The line is only indicative of the trend to the overall distribution of flow velocity for each set of slope.	71
Figure 4.22: Evolution of the angle between the fire fronts as a function of time for tests performed with different fuels in zero slope conditions ($\alpha=0^\circ$).	73
Figure 4.23: Comparison of the values of q by experimental measurements and by simulation. The angle between the two surfaces is indicated in the legend.	74
Figure 4.24: Rate of spread in the deceleration phase as a function of the calculated density of radiant heat flux for tests performed with different fuels in zero slope conditions ($\alpha=0^\circ$).	74
Figure 4.25: Values of R'_M as function of the initial angle between the fire fronts for series in which the slope value remains fixed ($\alpha=0, 10, 20$ or 30°).	77
Figure 4.26: The evolution of $R'_{M\theta}$ with α	78
Figure 4.27: Evolution parameter b_I of the Model 1 with the slope angle α	79
Figure 4.28: Evolution of ψ_1 with the initial angle between the fire fronts θ_o , for PP , fitted with a negative exponential law.....	79
Figure 4.29: Perfect fitting of the values of the model with the ψ_1 experimental data.	80
Figure 4.30: Values of R'_M as function of the angle of slope α for series in which initial angle between the value remains fixed ($\theta_o=15^\circ, 20^\circ, 30^\circ$ or 45°).	81
Figure 4.31: $R_{M\alpha}$ as function of θ_o	81
Figure 4.32: Evolution of ψ_2 as function of the initial angle slope α . For series with a fixed initial angle between the fronts ($\theta_o=15, 20, 30$ and 45°), with fuel PP . Fitted with a Power law model.....	82
Figure 4.33: Perfect fitting analysis of the models and relative Error assessment.	84
Figure 4.34: Time t'_M as a function of the angle θ_o and the models for this parameter. Models a, b and c corresponds to the parameters of Table 9 used in Equation 64 as following described.....	85
Figure 4.35: Model for the distance x'_M as function of the angle θ_o and experimental data.....	87
Figure 4.36: Exemplificative figures of the evolution of R^* as function of t^* or x^*	88
Figure 4.37: Tuning of the mathematical model for different values of the parameter a	89

Figure 4.38: Fitting of the model curve, for different values of slope (0, 10, 20, 30 and 40°), for the case of tests with initial angle θ_0 fixed in 30° and with fuel **PP**, as function of the non-dimensional time t^* 90

Figure 4.39: Fitting of the model curve, for different values of slope (0, 10, 20, 30 and 40°), for the case of tests with initial angle θ_0 , fixed in 30° and with fuel **PP**, as function of the non-dimensional time x^* 91

Figure 4.40: Comparison of the fitting parameters values of **A** and **B** as function of the slope (0, 10, 20, 30 and 40°) for plots in function of t^* and x^* respectively 92

Figure 4.41: Fitting of the model curve with fuel type **PP** and the slope angle fixed in 0° for different values of initial angle between the fire fronts, ($\theta_0 = 10, 15, 20, 30$ and 45°) respectively from left to right and from top to down. As function of t^* 94

Figure 4.42: Fitting of the model curve with fuel type **PP** and the slope angle fixed in 0°, for different values of initial angle between the fire fronts, θ_0 , (10, 15, 20, 30 and 45°) respectively from left to right and from top to down. As function of x^* 94

Figure 4.43: Comparison of the values of **A** and **B** for the curves with fuel type **PP**, the slope angle fixed in 0°, for different values of initial angle between the fire fronts, θ_0 95

Figure 4.44: Fitting of Model of R^* for the slope angle $\alpha=20^\circ$ with $\theta_0=30^\circ$ as function of t^* for the three fuels: a) **PP**, b) **ST** and c) **SH**. 96

Figure 4.45: Comparison of the values of **A** as function of the slope (0, 10, 20, 30 and 40°) for the case of tests with initial angle, θ_0 , fixed in 30° for the 3 different fuels. The average values are represented in a dotted line 97

Figure 4.46: Comparison of the values of **B** as function of the slope (0, 10, 20, 30 and 40°) for the case of tests with initial angle θ_0 fixed in 30° for the 3 different fuels. The average values are represented in a dotted line. 97

Figure 4.47: Fitting parameter **A** evolution for different scale lengths with **SH** as fuel. 99

Figure 4.48: Fitting parameter **B** evolution for different scale lengths with **SH** as fuel. 99

List of Tables

Table 1: Characteristic Properties of the different fuels	33
Table 2: Characteristic Residence time for the different fuels	35
Table 3.3 Characteristic rate of spread R_2 for different slopes and fuels.....	40
Table 4: Tests performed under the work program.	46
Table 5: Values of Parameters for each fuelbed.	75
Table 6: Parameters a_1 , b_1 , and $R'_{M\theta}$ for the exponential functions of R'_M	77
Table 7: R^2 for each model for different values of α	84
Table 8: Parameters a_3 and b_3 for different values of α	85
Table 9: Parameters a_3 and b_3 for the three groups of data.	85
Table 10: Variation of A, B and statistical parameters for the cases presented in the Figure 4.38 and Figure 4.39.....	92
Table 11: Variation of A, B and statistical parameters for the cases presented in the Figure 4.41 and Figure 4.42.....	95
Table 12: Parameters A and B for each fuel and statistical data.	97
Table 13: Fitting parameters A and B and statistical parameters.	98

Acronyms and Symbology

Acronyms

ADAI	Association for Development of Industrial Aerodynamics
LEIF	Forest Fire Research Laboratory
FCT	Portuguese Foundation for Science and Technology
FCTUC	Faculty of Science and Technology of University of Coimbra
UC	University of Coimbra

Symbology

Symbol	Units	Description
α	-	Inclination angle
α_w	-	Equivalent slope angle
β	-	Angle in relation to OX axis
β_f	-	Packing ratio
γ_1	-	Angle between r and the normal vectors to dA_1
γ_2	-	Angle between r and the normal vectors to dA_2
ε	-	Emissivity

ϵ_R	-	Heating number
σ_f	cm^{-1}	Average fuel particle surface to volume ratio
θ	-	Angle between the fire fronts
θ_0	-	Initial angle between the fire fronts
ρ_b	$kg.m^{-3}$	Bulk density
ρ_p	$g.cm^{-3}$	Fuel particle density
σ	$W.m^{-2}.K^4$	Stefan Boltzmann constant
ψ_2	-	Normalized function ψ_2 for R'_M
ψ_1	-	Normalized function ψ_1 for R'_M
ω'	-	Normalized fire line rotational velocity
a'_1	-	Parameter of the eruptive model for Pinus pinaster according to (Viegas 2006b)
a'_2	-	Parameter of the eruptive model for Pinus pinaster according to (Viegas 2006b)
A_1	m^2	Flame surface area
A_2	m^2	Element fuelbed area
b_1	-	Parameter of the eruptive model for Pinus pinaster according to (Viegas 2006b).
b_{1G}	-	Parameter of the model ψ_1
b_2	-	Parameter of the eruptive model for Pinus pinaster according to (Viegas 2006b).
D	-	Intersection point D of the two fire lines
dA_1	m^2	Infinitesimal surface element of flame
dA_2	m^2	Infinitesimal surface element of fuel
D_F	cm	Depth of the flaming zone of the fire front
dh	$J.kg^{-1}$	difference between total and ambient specific enthalpy of combustion gases
dV	V	Signal in voltage
e	$J.m^{-2}$	density of energy produced by fire line
E_1	$W.m^{-2}$	Hemispheric emissive power of the flame
E_1	J	Total energy distribution in the control area produced by fire line L_1
e_{11}	$J.m^{-2}$	Density of energy produced by fire line L_1 for $-a < y_1 < b$
e_{12}	$J.m^{-2}$	Density of energy produced by fire line L_1 for $b < y_1 < c$
E_2	J	Total energy distribution in the control area produced by fire line L_2

e_{21}	$J.m^{-2}$	Density of energy produced by fire line L_2 for $-b < y_2 < a$
e_{22}	$J.m^{-2}$	Density of energy produced by fire line L_2 for $-b < y_2 < -c$
E_o	$J.m^{-1}$	Reference energy produced by each fire line per unit length
e_o	$J.m^{-2}$	Peak value of energy density produced by each fire line (see Fig. 2.5)
E_T	J	Total energy distribution in the control area
f	-	Ratio between burned mass and available fuel mass defined in Eq. 17
F_{12}	-	View factor
h	$W.m^{-2}.K$	Convection heat transfer coefficient
h	$J.kg^{-1}$	Specific enthalpy of combustion gases
h_a	$J.kg^{-1}$	Ambient specific enthalpy of combustion gases
H_c	m	Characteristic fuel bed height
H_f	m	Flame Height
H_{fc}	$J.kg^{-1}$	Specific heat of combustion of the fuel
I	$J.m^{-1}.s^{-1}$	Fireline intensity
I_P	$kW.m^{-2}$	Propagating flux
IR	-	Infrared image
k	$W.m^{-1}.K^{-1}$	Thermal conductivity
k_1	*	Linear coefficient obtained multiplying k_1 by h_f
k_2	*	Linear coefficient of each trendline for the relation of the RD as function of q
L_1	-	Linear fire front 1
L_2	-	Linear fire front 2
L_f	m	Length of the flame surface
m_c	$Kg.m^{-2}$	Fuel load
m_f	%	Fuel Moisture Content (or FMC)
O	-	Origin of reference Cartesian system
OX	-	Reference axis
OX_o	-	X axis that is the axis of symmetry between the fire lines on the plane of the fuel bed
OY	-	Reference axis
OY_o	-	Y axis coincident with OY_o .
P_i	-	Pitot tube at position i
PP	-	Fuel bed of <i>Pinus pinaster</i> dead needles

q_{12}	$W.m^{-2}$	Density of incident radiation flux between one of the flames surface A_1 and an element of the fuelbed surface A_2 per unit of area(also expressed as q or q_r)
Q_{12}	W	Incident radiation flux between one of the flames surface A_1 and an element of the fuelbed surface A_2
q_c	$W.m^{-2}$	density of heat flux transfer by convection
Q_{ig}	$J.kg^{-1}$	Heat of pre-ignition
q_x	$W.m^{-2}$	density of heat flux transfer by conduction
r	m	Vector linking the centers of the two elements of area dA_1 and dA_2
R	$cm.s^{-1}$	Rate of spread (ROS) (also expressed in m/s)
R'	-	Non-dimensional rate of spread (NDROS)
R'_2	-	Non-dimensional rate of spread of a linear fire front in a slope condition
R'_i	-	The initial value of the non-dimensional rate of spread for Pinus pinaster according to (Viegas 2006b).
$R'_{M\alpha}$	-	Value of R'_M for $\alpha=0^\circ$, for each θ_0
R'_{M0}	-	Value of R'_M when $\theta_0 \rightarrow 0$, for each value of the slope angle
R_2	$cm.s^{-1}$	Rate of spread of a linear fire front in a slope condition
R_D	$cm.s^{-1}$	Rate of spread of the point D, as well mentioned as R (in $cm.s^{-1}$ or $m.s^{-1}$)
R_{DM}	$cm.s^{-1}$	Maximum rate of spread of the point D(also expressed in $m.s^{-1}$)
R_o	$cm.s^{-1}$	Basic rate of spread of linear fire in the absence of slope and wind
s_F	cm	Distance between the Pitot tube position i and the fire front
SH	-	Fuel bed of dead shrubs
ST	-	Fuel bed of straw
t	s	Chronological time
T	K	Temperature (also can be expresses in $^\circ C$)
T_∞	K	Temperature of the fluid
t^*	-	Non-Dimensional time referred to the maximum rate of spread R_D
t'	-	Reference time
T_a	K	Ambient temperature
TC	-	Thermocouple
T_i	K	Initial temperature
t_M	s	Chronological time elapsed until to the maximum value of R_D be registered
t_o		Residence time

T_s	K	Temperature of the hot surface
U^*	-	Non-dimensional flow velocity
U_i	$m.s^{-1}$	Flow velocity measured by Pitot Pi
U_o	$m.s^{-1}$	Reference wind velocity in the area of the fire
U_α	$m.s^{-1}$	Equivalent wind
V	-	Shape of the fire fronts
x	m	Coordinate along reference OX axis
x^*	-	Non-Dimensional distance referred to the maximum rate of spread R
x'	-	Non-Dimensional distance
x_D	cm	Distance travelled by the intersection point along OX axis
x_i	cm	Pitot tube i position
x_M	cm	Distance travelled by the intersection point along OX axis for the maximum value of R_D registered

Chapter 1.

General Introduction

This chapter introduces the overall framework of the study of the junction fire phenomena. The objectives of this work are hereby presented and defined considering the approach to the problem from the awareness to the comprehension of the physical processes and modelling of the junction fire behaviour. To facilitate the readability and comprehension of the thesis, the structure and the main topics addressed in each chapter are presented as well.

1.1. Background and Motivation

Forest fires are a phenomenon that occur in many regions of the World sometimes due to natural cases but quite often due to human activity. Although the presence of fire is necessary and required it may be the cause of important damages to the environment and to socio-economical life. Unfortunately, due to improper policies of fire management and firefighting, added to other conditions like climate change, the occurrence of many large fires with massive and destructive impacts has increased during the past decades. These fire events cause the loss of assets and the loss of human lives (Schemel *et al.* 2008), which are not acceptable in a modern society. As forest fires are the only one natural hazard in which the Human Being can act and modify their impacts (Viegas *et al.* 2011) it is important to

improve the knowledge about forest fires namely how they behave. This knowledge is possibly the main tool which Mankind has to deal with this complex problem.

Some fire events that present a low rate of spread and fire intensity, are not very dependent on time, and do not offer a great danger, are classified in Viegas *et al.* (2011). On the other hand it is remarked by several authors (Brown and Davis 1973; Chandler *et al.* 1983; Pyne 1984) that in many occasions forest fires behave in a surprising way, changing suddenly from moderate behaviour, characterized by a relatively low rate of spread, to an explosive propagation with a much faster velocity and heat release. These events that can behave differently with significant dynamic changes of their rate of spread and/or intensity in the course of time are classified as “extreme fire behaviour”.

This dynamic fire behaviour, that was formulated by Viegas (2004), Viegas (2006a), Viegas and Simeoni (2011), is characterised by sudden changes if its properties and does not fit with the classical approach from Rothermel (1972) that supports the existence of unique value of the rate of spread for a given set of fuel characteristics and environmental conditions. The dynamic fire episodes are of particular interest since they are commonly related to personal accidents as well as to important loss of assets. In Viegas (2012) the following definition of extreme fire behaviour (EFB) is proposed: EFB is defined as *the set of forest fire spread characteristics and properties that preclude the possibility of controlling it safely using available present day technology and knowledge*. Examples of EFB manifestations are conflagrations, eruptive fires, crown fires, spot fires, vortex structures and junction fires, among others. This list is not definitive nor complete as it may be changed if other processes become known.

The present study is focused on the specific EFB mechanism of the merging of two linear fire fronts, called in this work as “Junction fires”. The research on this topic was mainly motivated by the fire event that occurred in the vicinity of Canberra on 18 January 2003, where two merging fire fronts – MacIntyre Hut Fire and Bendora Fire – caused the destruction of part of the city of Canberra and several hectares of burned land. This event challenged our knowledge on fire behaviour as it brought us in contact with processes and phenomena that were not well understood or even studied. According to testimonies and ground evidences (cf. Doogan 2006), fire spread associated with these merging fires was very fast, and a tornado was formed ahead of the advancing fire front in the space between

the two main fires. This episode occurred in a situation characterised by: non-flat terrain, non-uniform vegetation cover, very strong wind and the influence of other very intense fires.

The identification and the initial study of this problem was carried out by ADAI team and performed in great part in the scope of the present thesis. Since the publication of our first papers on this topic (Viegas *et al.* 2012) the problem of junction fire has raised interest of the scientific community and other studies on the subject have appeared (Sharples *et al.* 2013; Thomas *et al.* 2015). At the beginning the designation for this type of fire behaviour was “**Jump Fire**” but after some discussion with the scientific and operational communities was decided to change the designation to “**Junction Fire**” to avoid confusion with spot fires that are also sometimes designated as fire jumps.

1.2. Objectives and Achievements

The purposes of this thesis is the analysis of the processes of merging of two linear fire fronts of a forest fire with the goal of bringing a better understanding of fire spread in the particular case of EFB called junction fire. With particular attention given to the evolution of the point of the intersection of the two fire fronts through the analysis of its rate of spread. The work the characterization of the phases of evolution of the rate of spread in junction fires and the definition of the influence of the radiation and of the convection in each phase is the objectives.

A study program based on laboratory experiments, field tests and real case fire events analysis was designed in which the effect of slope, fuel, initial angle between the fire fronts and scale is study was designed.

Models for the maximum rate of spread, model for the time taken by the fire front, and a model for the distance both for the maximum rate of spread were achieved. To close the problem a model for the entire evolution of the rate of spread as function of a single parameter will be introduced.

The last achievement is the design of a model that allows describing the overall fire spread of the intersection point in the case of fire fronts merging conditions with a single parameter.

1.3. Thesis Outline

The contents of the thesis is organized into five chapters. In order to facilitate its readability and comprehension this section presents a brief summary of the topics covered in each chapter.

Chapter 2 presents the concept of the Junction fire through the real fire that motivates the study of the phenomena and then the idealization and formulation of the problem are defined. The different scales in which the analysis of the problem is made are presented. In this chapter the main heat transfer modes related to fire propagation that are conduction, convection, radiation, and mass transport will be presented. The physical modelling of the problem of the junction fires are introduced through three models that were basis of the understanding of the problem and were used to the development to more complex and refined models about the junction fire.

Chapter 3 is devoted to the experimental work carried out at laboratory scale and extended to field and wildfire scales. In this Chapter the methodology applied and the parameters under control on the studied as the angle between the fire fronts, the slope angle of the fuel bed, type of fuel used and scale will be presented.

Measurements of radiation heat flux for validation of the numeric calculation of density of incident radiation flux was made through a bench test in laboratory were presented in this chapter. The characteristics of the tests performed in the experimental program and the principal parameters of the tests are given.

Chapter 4 addressed the overall evolution of the fire front during tests, the rotation of the fire lines, and the evolution of the point of intersection of the fire lines that is of particular interest along the study. The effect of the angle of slope, the fuel, the initial angle between the fire fronts and the scale in the results achieved are discussed. In order to analyse the evolution of the fire spread during the acceleration phase an approach of the problem through the eruptive model is made. A model of radiation to explain the variation of the rate of spread for the final deceleration phase of the fire the deceleration phase is proposed. Models for the maximum rate of spread reached, model for the time taken by the fire front until the maximum rate of spread, a model for the distance for the maximum rate of spread is developed in this chapter. To close the problem a model for the entire evolution of the rate of spread as function of a single parameter will be introduce. Finally as a synthesis the

aspects that affect the junction fires behaviour and the result achieved in which topic are discussed in the section of general discussion.

Chapter 5 summarizes the main issues addressed in the thesis, emphasizing the main contributions brought with the present work. Some recommendations for future work in the research of junction fires in the experimental work at laboratory and field scale as well the analysis of real scale fires are given. Some topics on the computational simulation of the junction fires and improvements on the modelling of the problem are suggested.

Chapter 2.

Junction Fires

In this chapter it is intended to familiarize the reader with the concept of junction fire as well to present models that allow the description of the phenomena. Although they are very simple models or adapted models is an aim of this work seed the basis of the understanding of the problem and for the growth of the future more complex and refined models about the junction fire.

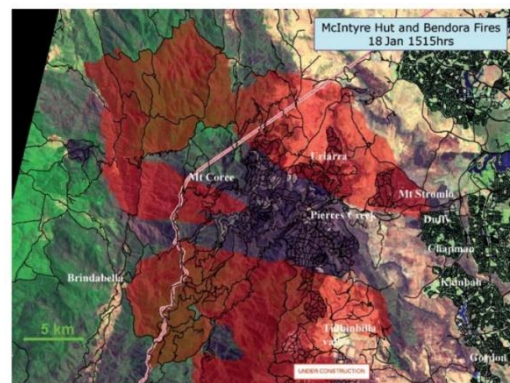
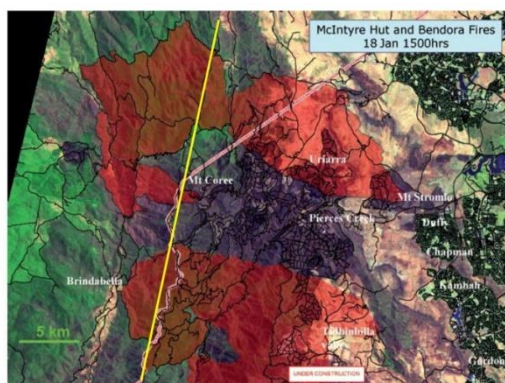
2.1. Fundamental concepts

2.1.1. Notion of junction fire

The interaction between fires or parts of fires has been observed and studied in the past. The increase in intensity at junction zones have been documented empirically (McRae *et al.* 2005; Brown and Davis 1973) when dealing with prescribed burning refer to interactions of fire fronts and mention that large areas or even small areas of high energy fuels near edges are unsafe, because dangerous runs against one side may develop. In Johansen (1984) is observed that in prescribed burns with spot fires in pine stands in the Georgia coastal plain, early flank merger caused a rapid increase in width of the flame zone at the moving fire front and an attendant to increase in flame height. Although this description does not correspond strictly to our definition of ‘Junction Fire’, it is very likely that the situations observed by Johansen (1987) were similar to the ones described in the

present work. Pyne (1984) say that in large fires are normal to have a proliferation of heads or columns but against this process of divergence, there is also a process of convergence: large fires absorb small fires; large columns incorporate small columns; multiple heads burn out intervening fuels and merge. Morvan *et al.*(2011)studied the interaction between two parallel fire fronts and concluded that their interaction is felt only at a relatively short distance. In a very detailed and exhaustive work about the interaction of fires Finney and McAllister (2011), it is noted that despite the relevance of the topic, there is no unified theory to explain fire interactions and much of the research on fire interactions comes from laboratory experiments with artificial fuel sources.

As referred in Chapter 1 the merging if two large fires in the vicinity of Canberra in January 2003, brought the motivation to better understand the problem of the interaction of fires. As documented in Doogan (2006) in mid-afternoon of the 18th January 2003 the merging of that fire fronts creates extraordinary junction fire phenomenon. The flanks of Bendora and McIntyre Hut’s large fires merged (Figure 2.1) on the undulating ground covered by grass, shrubs and groups of trees under a strong wind of the order of $25\text{m}\cdot\text{s}^{-1}$. The merging of these fires developed very rapidly ($27\text{ km}\cdot\text{h}^{-1}$) towards Canberra and even produced a tornado near one of its flanks and a “tongue” of fire. More details on this fire can be found in Sharples *et al.* (2012).



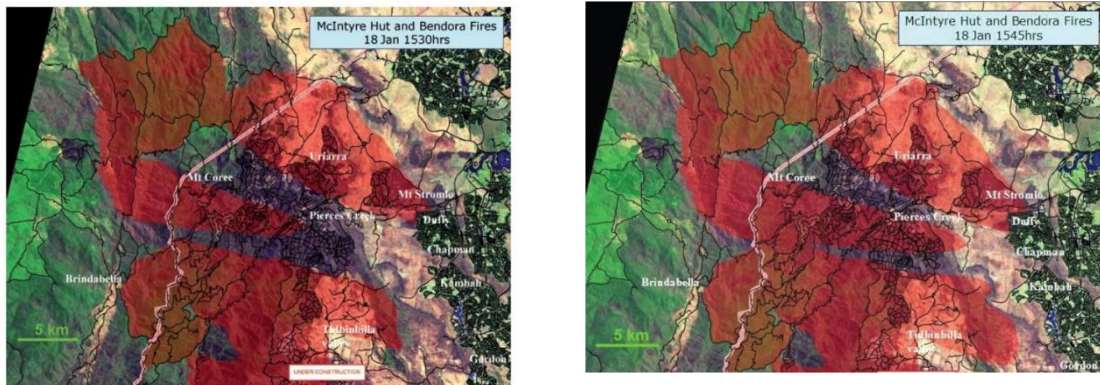


Figure 2.1: Evolution of McIntyres Hut and Bendora fires on the 18th January between 15.00h and 15.45h. Plates from Cheney report.

The idealization of the problem in a general and simple form, that can be studied, consists in a formulation in which two linear fire fronts that intersect at point D and making an angle θ_0 between them spreading on a uniform fuel bed making an angle α with the horizontal reference plane, spread in such a form that the area between them burns entirely. In Figure 2.2 a general idea about the geometry of the problem and the fundamental parameters in study (θ_0 , α , point D and the main axis system) are presented.

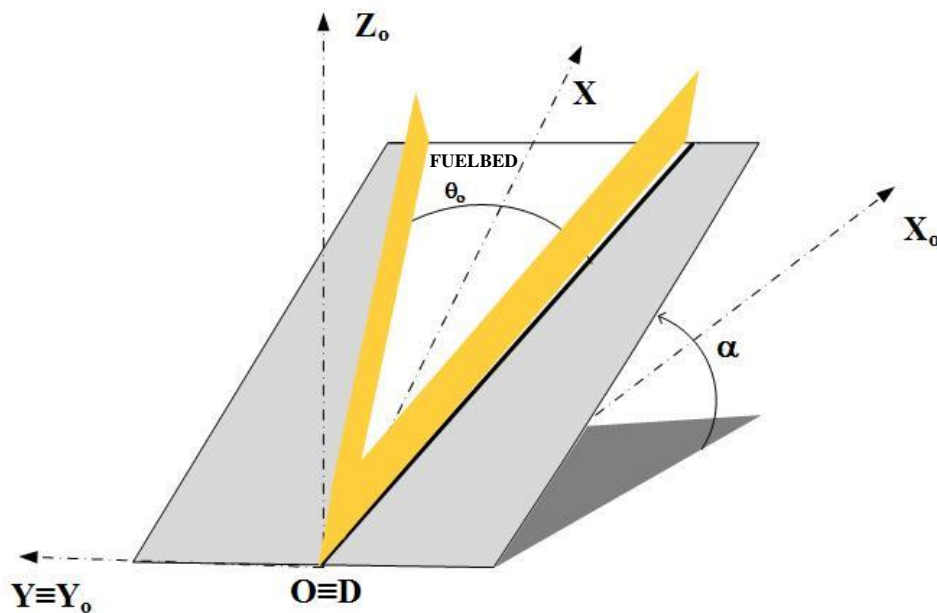


Figure 2.2: Schematic view of the tests performed with the basic parameters.

The process of merging of these fires in such cases is not one of the closure of the space between the fire lines by a reduction of their respective angle similar to the closure of scissors. On the contrary, it is their intersection point, defined here as point *D* that advances, tending to form a single straight fire line resulting from the two original ones. At the start of the merging process, the rate of spread of the intersection point *D* increases very rapidly, inducing what we will call a ‘Junction fire’, given the very high values of rate of spread that it can reach, in which is considered the acceleration phase. Even on a horizontal fuel bed, the displacement velocity can reach very high values that were not measured by our team in experiments in previous tests on horizontal fuel beds. The behaviour of the fire can be linked to a quick jump of the intersection point that is followed by a gradual decrease of its displacement velocity in the course of time that is denominated in this work as deceleration phase. This process is enhanced by the reduction of the initial angle between the two fire lines or by the presence of aligned slope or wind. The merging of two fire lines under the conditions described may occur not only in wildfires but also in prescribed burns or when the fire is used as a suppression tool.

To provide a better understanding of the process, non-dimensional representations will be used in Chapter 4. This non-dimensional analysis will be done by using the following non-dimensional variables, with the formulation presented:

Non-Dimensional time t' , here t_o is the residence time that will be defined in the following section.

$$t' = \frac{t}{t_o} \tag{1}$$

Non-Dimensional time t^* , here t_M is the time up to the maximum rate of spread *R* is registered.

$$t^* = \frac{t}{t_M} \tag{2}$$

Non-Dimensional distance x'

$$x' = \frac{x}{R_o \cdot 1s} \tag{3}$$

In this equation R_o is the basic rate of spread of a linear fire front spreading on a given fuelbed under no slope and no wind conditions.

Non-Dimensional distance x^* :

$$x^* = \frac{x}{x_M} \quad 4$$

In this equation x_M is the distance along OX axis where the maximum rate of spread R_M is registered

Non-Dimensional rate of spread R' , here R_o is the basic rate of spread.

$$R' = \frac{R}{R_o} \quad 5$$

Maximum non-dimensional rate of spread R'_M , here R_M is the maximum rate of spread registered in each test.

$$R'_M = \frac{R_M}{R_o} \quad 6$$

Non-dimensional rate of spread R^* , here R_M is the maximum rate of spread registered in each test.

$$R^* = \frac{R}{R_M} \quad 7$$

Non-Dimensional rate of spread R'_2 .

$$R'_2 = \frac{R}{R_2} \quad 8$$

In this equation R_2 is the rate of spread of a linear fire front in a same slope condition, the values of R_2 will be tabled in the following section.

The present research program contains sets of tests performed at three different scales. Tests from the small-medium scale in the laboratory, the large scale of the field experiments and the very large scale of real fire events analysis were used. Partial

descriptions of the experimental work performed can be found in the works Viegas *et al.* (2012), Viegas *et al.* (2013), Raposo *et al.* (2014). In Figure 2.3 the different ranges of analysis of this study are evident. The laboratory work which involves distances of few meters, the field experiments which scale up the problem to dimensions of dozens of meters, and finally the fire events of Australia, in 2003, with the dimension of thousands of meters.

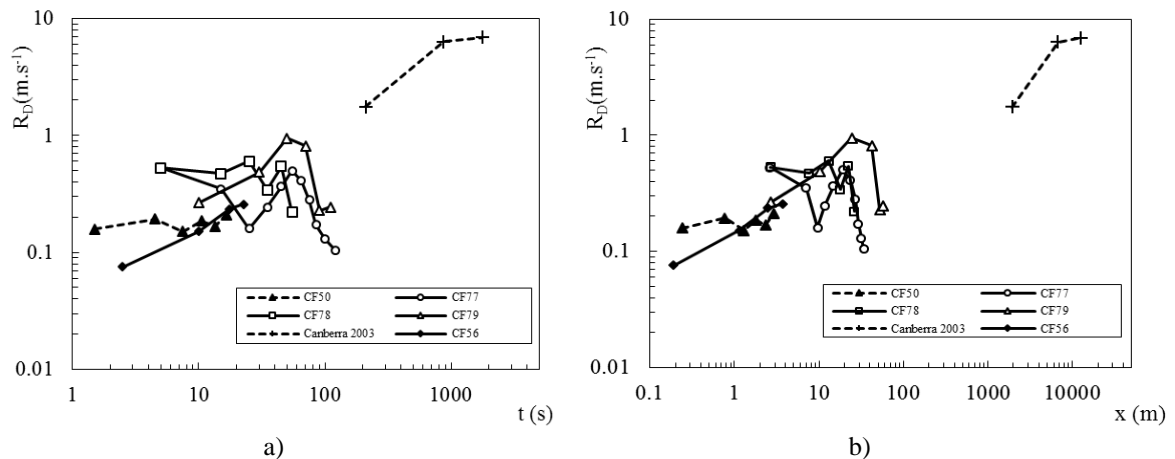


Figure 2.3: Rate of spread R_D as a function of the distance in case a) and as a function of time in b) for tests with shrubs, including laboratory, field and a real case.

Taking into the account the rate of spread of the fire fronts R_D , in $\text{m}\cdot\text{s}^{-1}$, a large range of values was observed considering the different space and time scales involved. In Figure 2.3 it is important to refer that the fuel of the cases represented is shrubs in all the cases, due to the consideration that in the fires events of the Australia, the fuels that were supporting fire propagation were mainly shrubs. Also, the initial angle between the fire fronts θ_0 in the representation was fixed in the value of 30° for the same reason.

In addition, the study will introduce a parametric analysis of the natural parameters, imposed at the beginning of each test, shifting them from test to test. More specifically were different fuels, different slopes of the fuel bed α , and different initial angles between the fire fronts θ_0 and scales were studied.

As referred in the idealization of the problem in the study on junction fires we dedicate our attention to the particular case of two linear fires making a relatively small angle between them, in nominally symmetrical boundary conditions. Particular attention is given in this study to the displacement of the intersection point D of the two fire lines that has a velocity or rate of spread R_D .

In the general case the rate of spread R_D of the fire in the vicinity of point D will possess the following functional dependence:

$$R_D = f(\theta_o, \alpha, U_o, \beta, m_f, \sigma_f, \dots, t) \quad 9$$

In this equation U_o is the reference wind velocity in the area of the fire, β its angle in relation to OX axis, m_f is the moisture content of the fuel, σ_f is the average fuel particle surface to volume ratio and the dots are in the place of the wide set of parameters that are required to define the fuel bed properties. In equation 9 time is shown as an explicit variable as we are in the presence of an essentially dynamic fire behaviour process in which the overall geometry and fire spread conditions change in the course of time even if the initial environmental conditions remain constant.

An alternative variable that can be used to describe the movement of the fire front is the angle θ between the fire fronts assuming that they can be approximated by straight lines and by the distance x_D travelled by the intersection point along OX axis. The angle of the fire fronts can then be written as:

$$\theta = f(\theta_o, \alpha, U_o, \beta, m_f, \sigma_f, \dots, t) \quad 10$$

The distance x_D travelled by the intersection point at a given time t is given by:

$$x_D = \int_0^t R_D \cdot dt \quad 11$$

Given (11) x and t cannot be considered as independent variables but we can use x alternatively as variable instead of t and express (9) in the following alternative form:

$$R_D = f(\theta_o, \alpha, U_o, \beta, m_f, \sigma_f, \dots, x) \quad 12$$

Through these relations the aim of the study and the most important parameters that were in the scope of the study were defined.

2.1.2. Heat transfer mechanisms

In this section the main heat transfer modes related to fire propagation that are, according to Anderson (1969) conduction, convection, radiation, and mass transport will be presented.

Conduction

Conduction is the heat transfer mode within the material itself by gradients of temperature. The density of heat flux transfer by conduction $q_x(\text{W}\cdot\text{m}^{-2})$ in a one-dimensional plane with a distribution of temperature $T(x)$ can be quantified by the expression (13) known as Fourier law (Incropera *et al.* 2011):

$$q_x = -k \cdot \frac{\partial T}{\partial x} \quad 13$$

The thermal conductivity k ($\text{W}\cdot\text{m}^{-1}\cdot\text{K}^{-1}$) is defined for each material. For vegetal/wooden materials as forest fuels the value of k is very low ($0.12 \text{ W}\cdot\text{m}^{-1}\cdot\text{K}^{-1}$ for softwoods) compared with other materials as for example carbon steel ($60.5 \text{ W}\cdot\text{m}^{-1}\cdot\text{K}^{-1}$ for carbon steel AISI 10). So in forest fires the mechanism of heat transfer by conduction is commonly discounted as being too slow to be of importance in transferring heat through a porous fuel bed (Van Wagner 1968; Chandler *et al.* 1983).

Convection

The heat transfer mode of convection is characterised by the transport of heat by a fluid in motion and can be classified by the nature of the flow. Commonly we speak of natural convection when the movement of a gas or liquid is induced by the buoyancy forces due to the differences of density caused by the difference of temperature. Forced convection corresponds to the transport of heat by the movement of a gas or a liquid caused by external means as the presence of wind or a difference of pressure. The transference of heat by convection is expressed by Equation (14) that is known as Newton law of cooling (Incropera *et al.* 2011):

$$q = h(T_s - T_\infty) \quad 14$$

In the equation q ($\text{W}\cdot\text{m}^{-2}$) is the density of heat flux transfer by convection, h ($\text{W}\cdot\text{m}^{-2}\cdot\text{K}$) is the convection heat transfer coefficient, T_s is the temperature of the surface and T_∞ is the temperature of the fluid.

The role of convection induced by the fire, eventually enhanced by terrain configuration and its interaction with the combustion process and the fire front shape, is sometimes overlooked, making it difficult to explain some features that are observed in forest fire propagation in complex terrain (Viegas and Pita 2004). Many times the major heat transfer mechanism considered is radiation (Chandler *et al.* 1983). However due to the key role played by convection in several types of fire behavior especially in large and very intense fires this mechanism should not be underestimated.

It is true that in small surface fires convection is usually associated with the surface atmospheric winds or to buoyancy induced flows due to the low density of the combustion products released in the reaction zone these hot gases rise from the fire and their effect on the fire spread is quite low. In large fires these convective flows interact with the upper layers of the atmosphere creating a feedback process (Viegas 1997). These convective flows are a source of extreme high rate of spread and sudden changes its value. This remarks the importance of the role played by the heat transfer mechanism of convection on the EFB manifestations.

The convective induced flows can increase even more the rate of spread in situations in which these flows are aligned with main direction of propagation due either to the effect of slope or to the angle formed between the flow and the terrain. In this way a larger amount of heat produced will be released in the fuel ahead that will increase the rate of burning of the fuel and consequentially increasing the rate of spread of the fire front.

Convection on the junction fires is an important factor that was taken into account in this work. The configuration of the junction fires creates very strong flows that are developed inside the burning area, due to the concentration of energy created by the merging of the fire fronts that is favourable to the main fire propagation. These induced flows are more effective in incrementing the rate of spread with the increase of the angle of slope that causes an approach of the generated flow to the fuelbed, and with the narrowing of the angle between the fire fronts.

The acceleration of the junction fires is comparable to the fire acceleration registered in eruptive fires as will be discussed in this document in sub-section 2.2.2.

The deceleration phase is also dependent of the convection activity due to a gradual change of the flame configuration that allows the entrance of a contrary flow that decreases

the rate of spread of these fires and after that the radiation take places as the main mechanism of this phase of propagation.

Radiation

Thermal radiation is energy emitted by matter at a given temperature above the absolute zero temperature. The emitted radiation flux per unit area q ($\text{W}\cdot\text{m}^{-2}$) is given by Stefan Boltzman law, Equation (15) (Quintiere 2006):

$$q_r = \varepsilon \cdot \sigma \cdot T_s^4 \quad 15$$

In this equation ε is the emissivity of the surface, σ is the Stefan Boltzmann constant ($\text{W}\cdot\text{m}^{-2}\cdot\text{K}^{-4}$) and T_s is the absolute temperature of the surface (K)

According to several authors namely Viegas (2002a); Chandler *et al.* (1983); Frankman *et al.* (2013) the thermal radiation is an important mechanism in forest fire spread, given the very high temperatures that are reached in the reaction zones of the fire. There are two main combustion zones at the fire front: one inside the solid porous fuel bed and the other in the gaseous phase, in the flame above the fuel bed. The radiation from the solid phase, inside the fuel bed, has a relatively short range given the attenuation produced by the solid fuel particles, therefore, its heat flux causes a relatively slow rate of spread of the fire front and will be not taken into account in this work. Radiation from the flame surface depends significantly on the size and shape of the flame, namely on its inclination angle in relation to the fuel.

If the flame is inclined towards the already burned fuel the contribution of the flame for the advance of the fire will be relatively low. Therefore for contrary wind or slope, the rate of spread will be very low and practically constant as the shape of the reaction zone is not very much affected in this case.

If the fire front is propagating with a favourable wind or up slope, the flame will be inclined towards the unburned fuel and its distance to the fuel bed will be smaller and its shape factor in relation to the fuel bed will be much larger, increasing substantially the rate of spread.

Sometimes the distinction of the effect due to convection or radiation is not easy to make because they act together. For example the favourable convective flow, due to wind or

slope, will enrich the combustion process and the size of the flames will be enlarged contributing to a more intense radiation flux to the fuelbed, and that will increase the rate of spread.

Due to the particular geometry of the junction fires the fire fronts will suffer a strong inclination towards the fuel bed inside the V shape created by the junction of the two fire fronts. In the deceleration phase in the initial stage the convection plays an important role but on the other hand in the final stage radiation is the main driver of fire propagation. A relationship between the rate of spread and density of incident heat flux will be presented in sub-section 2.2.3

Mass Transport

The mechanism of mass transport is the process of removal, transportation and release of burning particles from the fire front which are lofted by the convection column and dropped at considerable distances from the main fire (Sardoy *et al.* 2007). If these burning embers, transported by convection and wind, fall on the ignitable material new fires can be ignited, with the associated danger to the fire control process (Almeida 2011; Ellis 2000). These burning embers (spotfires) are particularly common and dangerous in large fires with strong convective activity (Tarifa *et al.* 1965). Due to its complexity this still an open problem on the research of forest fires. Despite of its importance in the present study the mechanism of mass transportation was not taken in account.

2.2. Physical Modelling

2.2.1. Energy concentration concept

In (Viegas *et al.* 2012) a conceptual model based on the concentration of energy that is associated to two linear fire fronts, L_1 and L_2 , was proposed as an initial explanation of the rapid change of rate of spread with the modification of the fire geometry. This model proposed a relationship between the total energy E_T , in the control area and the rate of spread R of the intersection point D . This model is focused in the prediction of the decreasing phase of the junction fire phenomena associated to the change of the fire front geometry during its development. However during this study an additional explanation for this phase was developed due to insufficient description provided by this preliminary model.

To explain this concept of energy distribution and accumulation let us consider a uniform linear fire front that has associated with it a coordinate system OX_1Y_1 , as shown Figure 2.4

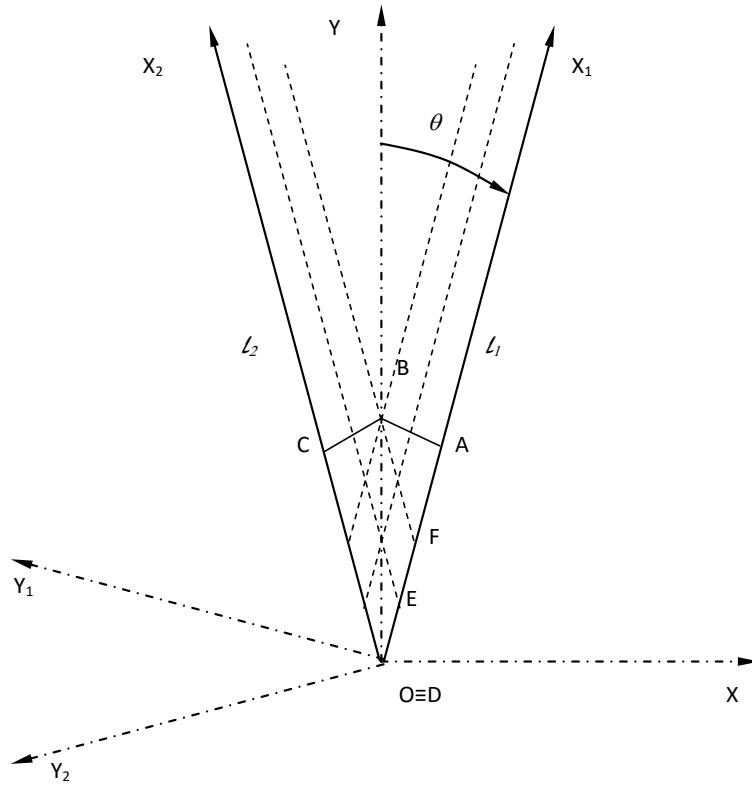


Figure 2.4: Schematic view of the geometry of two oblique fire lines in symmetrical conditions. The dotted lines in this figure correspond to the limits of the energy distribution.

The overall energy that is released by this fire line per unit of time and of fire line length is given by the Byram's fire line intensity (Byram 1959):

$$I = M_c \cdot H_{fc} \cdot R \tag{16}$$

In this equation M_c ($\text{kg}\cdot\text{m}^{-2}$) is the fuel load that is consumed in the unit of time, H_c ($\text{J}\cdot\text{kg}^{-1}$) is the net heat that is released by the combustion of a unit mass of fuel and R is the rate of spread of the fire line. The fuel consumed M_c will be a fraction of the total fuel load M_{oc} available in the area:

$$M_c = f \cdot M_{oc} \tag{17}$$

For a fire line spreading in a given fuel bed under well-defined slope and wind conditions, we can assume that M_{oc} , Hf_c and f are practically constant and according to Equation (16) the total energy released will depend linearly on the value of the rate of spread R .

The energy released in a unit of time will be available in the matter above the ground as an excess of enthalpy and of kinetic energy in relation to ambient conditions that are assumed to be of stagnant air (no wind conditions). The excess of enthalpy per unit of mass is then:

$$\Delta h = h + \frac{v^2}{2} - h_a \quad 18$$

In Equation (18) v is the velocity of the flow and h_a is the enthalpy of the air in the initial ambient conditions. If we neglect the contribution of solid and liquid matter in the balance of energy and assume that the entire matter in the vicinity of the fire line is a perfect gas then the enthalpy will depend solely on the absolute temperature and equation 19 can be written:

$$\Delta h = C_p(T - T_a) + \frac{v^2}{2} \quad 19$$

If we consider a section or slice of the fire line with an infinitesimal length dx_1 , the fraction of energy released per unit of time in the volume defined by two planes perpendicular to Ox_1Y_1 separated by a distance dx_1 is:

$$dE = I \cdot dt \cdot dx_1 \quad 20$$

The available energy will vary with the coordinate y_1 along the fire spread direction as it is indicated in Figure 2.5. In this figure the origin of OY_1 axis is taken at the end (trailing edge) of the flaming zone that has a depth D_F . For a given value of y_1 the energy available in the volume above an infinitesimal element of area $dx_1 \cdot dy_1$ can be obtained by the following equation:

$$de = \int_{z_1=0}^{\infty} \rho \cdot [C_p(T - T_a) + \frac{v^2}{2}] dx_1 \cdot dy_1 \cdot dz_1 = e \cdot dx_1 \cdot dy_1 \quad 21$$

The parameter e ($J \cdot m^{-2}$) is the density of energy available above the ground per unit of area and per unit of time.

$$dE = \int_{y_1=-\infty}^{\infty} e \, dx_1 \cdot dy_1 = I \cdot dt \cdot dx_1 \quad 22$$

Energy Density Distribution

In the general case e will be a function of both x_1 and y_1 . In the present case as we assume a linear fire front of infinite length with uniform properties e will not depend on x_1 .

The density of available energy per unit area is therefore a non-negative function of y_1 , with a maximum value e_0 . Taking into account Equation (19) and the well-known variation of air temperature at a given height measured by a thermocouple during the passage of a fire front (Mendes-Lopes *et al.* 2003; Cruz *et al.* 2006; Alexander and Cruz 2011) it is reasonable to accept that the function $e(y_1)$ has a shape similar to the curve that is shown in Figure 2.5. In this figure the coordinate was made non dimensional as y_1/d .

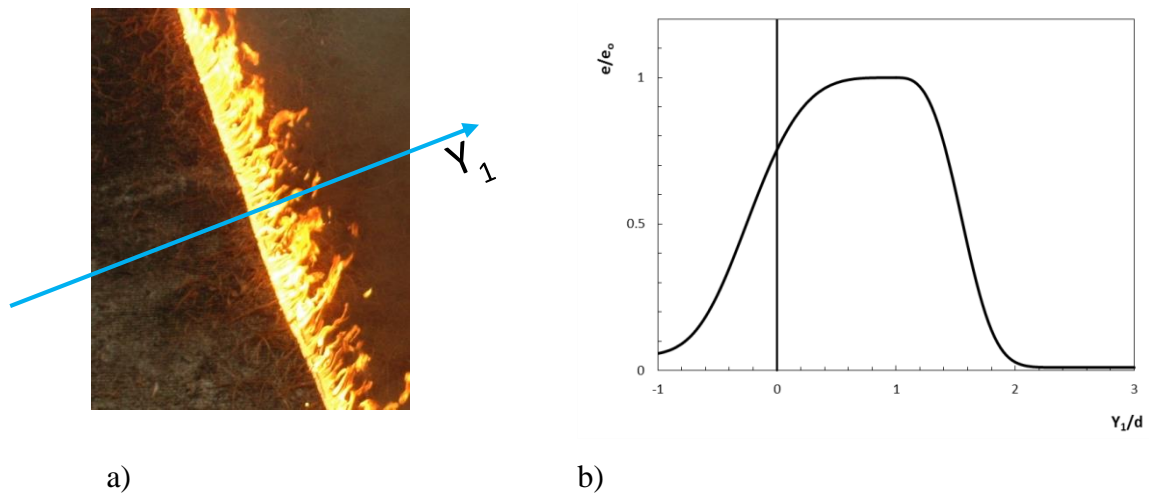


Figure 2.5: a) Representation of axis Y_1 crossing the fire line. b) Conceptual sketch of the variation of energy density along the axis perpendicular to fire line L_1 . The parameter d is a reference length of the order of the flame depth.

Quasi steady conditions

Although we are in the face of a dynamic process that is intrinsically dependent on time we shall assume that it is possible to break it into steps of time in which we have quasi-

steady conditions associated to the geometrical configuration of the fire lines that is defined by angle θ at each time step.

In order to assess the influence of one fire line on the other and consequently on the spread of both, for a given configuration, we shall compute the total energy E_T in the volume above the control area defined by the polygon $ABCD$ that is shown in Figure 2.4. This energy is given by the following expression:

$$E_T = E_1 + E_2 \tag{23}$$

Where E_1 and E_2 are the contributions given respectively by fire lines L_1 and L_2 to the total energy in that area.

Relationship with rate of spread

As it was implied in the considerations that were made above we assume that there is relationship between the total energy in the control area and the non-dimensional rate of spread R' of the intersection point. As a first step we assume a linear relationship between these two quantities expressed in the following form:

$$R' = k \cdot \frac{E_T}{E_o} \tag{24}$$

In this Equation E_o (J) is a reference value of the available energy per unit length of the fire line that is computed below and the proportionality factor k has no dimensions. The assumption of a linear relationship between the amount of energy available in the reference area and the rate of spread is supported by Equation (16), which is quite accurate if M_c and H_c are constant, as we are assuming.

Simplified analytical model

To facilitate the development of the analytical model we shall assume that the energy density distribution along OY_1 is different from zero only for $-a < y_1 < c$. We consider that it can be represented by the following analytical functions involving four parameters. These parameters will be adjusted to comply with the fire line properties. As a matter of fact given the strong dependence of the reference area on the angle θ any plausible non negative function similar to that described above should provide similar results.

Although in a real fire the properties at the fire front change due to fire dynamics, for the sake of simplicity we shall assume that the model parameters remain constant during the evolution of the fire lines. This approach corresponds to a quasi-steady description of fire evolution assuming that its properties are greatly associated to the geometry of the firelines.

$$\text{For } -a < y_1 < b: \quad e_{11} = e_o \cdot \sin\left(\frac{\pi}{2} \cdot \frac{y_1 + a}{b + a}\right) = e_o \cdot \sin(k_{11} \cdot (y_1 + a)) \quad 25$$

$$\text{For } b < y_1 < c: \quad e_{12} = e_o \cdot \cos\left(\frac{\pi}{2} \cdot \frac{y_1 - b}{c - b}\right) = e_o \cdot \cos(k_{12} \cdot (y_1 - b)) \quad 26$$

with:

$$k_{11} = \frac{\pi}{2 \cdot (b + a)} \quad 27$$

$$k_{12} = \frac{\pi}{2 \cdot (c - b)} \quad 28$$

The linear distances **a**, **b** and **c** depend on the properties of the fire line and must be adjusted for each case. The following values for the model parameters were considered in its application to laboratory scale tests: a=0.2m, b=0.1m and c=0.2m. The value b=0.1m corresponds roughly to the flame depth for the fuel bed that was used. Pine needles have a flame residence time of the order of 54 seconds, with a basic rate of spread $R_o=0.2 \text{ cm} \cdot \text{s}^{-1}$ we obtain a flame depth of 0.12m. The other distances were set with the same order of magnitude.

The functions represented by Equations (25) and (26) are shown in Figure 2.6.

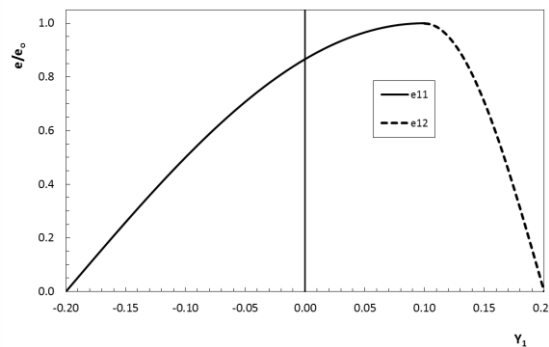


Figure 2.6: Simplified model of energy density variation along axis Y_1 .

For line L_2 we associate the reference system OX_2Y_2 the corresponding energy density distribution is given by the following set of equations:

$$\text{For } -b < y_2 < a: \quad e_{21} = e_o \cdot \sin\left(\frac{\pi}{2} \cdot \frac{y_2 - a}{-b - a}\right) = e_o \cdot \sin(k_{21} \cdot (y_2 - a)) \quad 29$$

$$\text{For } -c < y_2 < -b : \quad e_{22} = e_o \cos\left(\frac{\pi}{2} \cdot \frac{y_2 + b}{b - c}\right) = e_o \cdot \cos(k_{22} \cdot (y_2 + b)) \quad 30$$

With:

$$k_{21} = \frac{\pi}{2 \cdot (-b - a)} \quad 31$$

$$k_{22} = \frac{\pi}{2 \cdot (b - c)} \quad 32$$

The functions represented by equations (29) and (30) are shown in Figure 2.7.

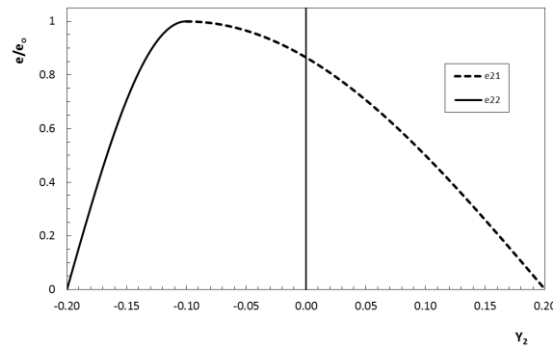


Figure 2.7: Simplified model of energy density variation along axis Y_2 .

Given the symmetry of the problem and the form adopted for the density of energy distribution we can decompose each one of those functions in the following form:

$$E_1 = 2 \cdot (E_{11} + E_{12}) \quad 33$$

$$E_2 = 2 \cdot (E_{21} + E_{22}) \quad 34$$

Reference Energy

In order to have a physical meaning of the parameters of the model we estimate the total energy E_o (J) of the fire line for a reference area A_o of unit width ($\Delta x_I = 1\text{m}$). The value of E_o is obtained integrating (22) along OY_I making $\Delta x_I = 1\text{m}$. The value of E_o is given by:

$$E_o = \int_{-a}^b e_{11} dy_1 + \int_b^c e_{12} dy_1 = \frac{2 \cdot e_o \cdot (a + c)}{\pi} \quad 35$$

For the present values of a and c this is equal to $0.8 \cdot e_o / \pi \approx 0.255 \cdot e_o$ (J).

Analytical Solutions

The analytical solutions to determine E_2 in each range of values of θ are given below:

$$0^\circ < \theta < 45^\circ$$

$$E_2 = 2 \cdot e_0 \left[\frac{1}{k_{21}^2} [\sin(k_{21} \cdot a) + 1] \cdot \left(\frac{1}{\tan 2\theta} - \frac{1}{\tan \theta} \right) + \frac{1}{k_{22}^2 \cdot \tan \theta} \cdot \left(\frac{\pi}{2} - 1 \right) - \frac{2 \cdot e_0}{k_{22}} \left[\frac{b}{\tan \theta} - \frac{c}{\tan 2\theta} \right] \right] \quad 36$$

$$45^\circ < \theta < 90^\circ$$

$$E_2 = 2 \cdot e_0 \left[\frac{1}{k_{21}^2 \cdot \tan \theta} [\sin(k_{21} \cdot a) + 1] - \frac{\tan 2\theta}{k_{22}^2} \left[\cos \left(k_{22} \cdot \left(b - c \left(1 + \frac{1}{\tan \theta \cdot \tan 2\theta} \right) \right) \right) \right] - \frac{1}{k_{22}^2 \cdot \tan \theta} \right] \quad 37$$

The results obtained with the analytical model are shown graphically in Figure 2.8 in the form of E_T/E_0 as a function of θ_0 , for values of $\theta_0 > 10^\circ$.

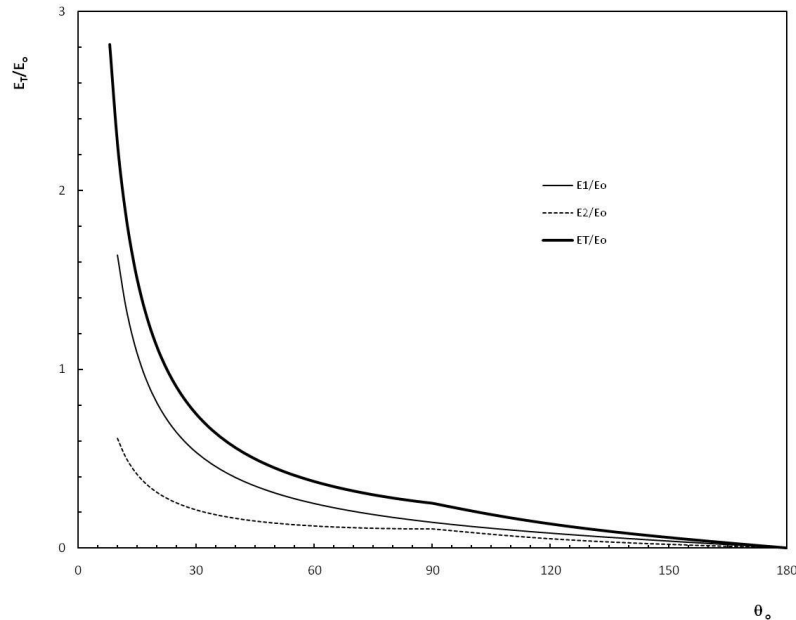


Figure 2.8: Non dimensional energy in the control area as a function of the angle between the fire lines evaluated using the present model for values of $\theta > 5^\circ$. The curves show the contributions E_1 and E_2 of L_1 , of L_2 respectively and the total energy E_T .

2.2.2. Convection Processes

The acceleration phase observed in the junction fires is so pronounced and sudden that it can only be explained through convective processes induced by the concentration of energy at the interception point of the fire lines. The referred acceleration is comparable to that observed in the eruptive fires that leads us to make a similarity between these two types of fire behaviour.

For this reason the model of eruptive fires, that was proposed by Viegas (2006b), to predict the rate of spread of fires in canyons and steep slopes as a function of time, will be applied to the acceleration phase of the junction fire. For this a brief presentation of this model will be made here.

The eruptive fires model is based on two hypothesis: (i) the existence of a univocal relationship between the reference wind velocity U and the rate of spread R . (ii) the existence of a univocal relationship between the increment of the fire induced flow velocity dU and the increment of the rate of spread dR in a given period of time dt .

These two hypothesis are the basis of the convective process of feedback that create the acceleration of the fire and that is expressed in non-dimensional form by the differential Equation of the model (38). The non-dimensional rate of spread R' is defined in Equation (5) and the other non-dimensional parameters (a'_1 , a'_2 , b_1 and b_2) can be determined experimentally for each type of fuel as described in Viegas (2006b).

$$\frac{dR'}{dt} = a'_1{}^{\frac{1}{b_1}} \cdot b_1 \cdot a'_2 (R'-1)^{1-\frac{1}{b_1}} R'^{b_2} \quad 38$$

The application of the model to the junction fires was made using the following values of the model parameters $a'_1=1.1$, $a'_2=0.5$, $b_1=2.2$ and $b_2=1.16$ for *Pinus pinaster* according to (Viegas 2006b).

The Equation (38) can be integrated numerically from 0 until to the instant t' , taking the form of the expression (39) for which the rate of spread is equal to R' . The initial value of the non-dimensional rate of spread depends of the initial boundary conditions and for this case the value of $R'_i = 1.1$ was used.

$$R' = R'_i + \int_0^{t'} \frac{dR'}{dt} \quad 39$$

2.2.3. Radiation Processes

In order to assess the role of radiation in the propagation of the fire front in the vicinity of point D we shall use the results and correlations developed by Rothermel that are based on a very extended and comprehensive experimental program. In Rothermel (1972) the concept of propagating flux expressed in the Equation (40) is proposed:

$$R = \frac{I_p \cdot \xi}{\varepsilon_R \cdot \rho_b \cdot Q_{ig}} \quad 40$$

In this equation the propagating flux I_p ($\text{kW} \cdot \text{m}^{-2}$) is the energy received by the fuel bed per unit of area and per unit of time. This flux is derived essentially from the radiation of the fire front and from convection due to the flow around the fuel element.

The fuel bed bulk density ρ_b ($\text{kg} \cdot \text{m}^{-3}$) is defined by the mass of fuel divided by its volume or by the fuel load m_c ($\text{kg} \cdot \text{m}^{-2}$) divided by height of the fuelbed layer h_c (m) (Equation 41):

$$\rho_b = \frac{m_c}{h_c} \quad 41$$

The effective heating number ε_R measures the proportion of fuel mass that participates in the propagation phase. According to Rothermel (1972) ε_R depends on the fuel characteristic surface-volume relation σ_f .

The propagation flux ratio ξ is a function of σ_f and of the packing ratio β_f that is given by the quotient of the fuel bed bulk density ρ_b by the fuel particle density ρ_p .

The heat of pre-ignition Q_{ig} ($\text{J} \cdot \text{kg}^{-1}$) is the energy required to raise the temperature of a unit of mass of fuel from ambient to ignition temperature plus the energy required to heat the water content of the fuel from ambient to the boiling temperature and the latent heat to vaporize it. Thus, the value of Q_{ig} is a function of the fuel load and moisture content (Almeida 2011).

For a given fuel we can assume that:

$$R = k_1 \cdot I_p \quad 42$$

In the present study some parameters were kept constant in all the experiments, like for example the fuel load m_c . So it is possible to decompose k_1 in a part k_2 that should be constant for the tested fuel beds and another one involving h_f , ξ , ε_R and Q_{ig} that varies from one fuel to another. Therefore we can write equation (42) as:

$$R = k_2 \cdot \frac{h_f \cdot \xi}{\varepsilon_R \cdot Q_{ig}} \cdot I_p \quad 43$$

We used this Equation (43) which expresses a linear relationship between the rate of spread (ROS) and the propagation flux I_P to test the hypothesis of the propagation flux energy coming only from the flame incident radiation flux: $I_P=q$.

In order to estimate the flame density of radiation flux q ($\text{W}\cdot\text{m}^{-2}$) we consider the simplified case of a horizontal fuel bed with two fire fronts with vertical flames making an angle θ between them as shown in Figure 2.9. In a general form the radiation flux Q_{12} (W) emitted by a surface with an area A_1 and that reaches a surface A_2 is given by (cf. Incropera *et al.* 2011; Figueiredo *et al.* 2015):

$$Q_{12} = \frac{A_1 \cdot E_1}{A_2} \iint_{A_1 A_2} \frac{\cos(\gamma_1) \cdot \cos(\gamma_2)}{\pi \cdot r^2} dA_1 \cdot dA_2 = A_1 \cdot E_1 \cdot F_{12} \quad 44$$

In this equation E_1 is the hemispheric emissive power emitted by the flame surface (equation 45), F_{12} is the view factor, r is the vector linking the centres of the two elements of area dA_1 and dA_2 , γ_1 and γ_2 are the angles between r and the normal vectors to dA_1 and dA_2 , n_1 and n_2 respectively.

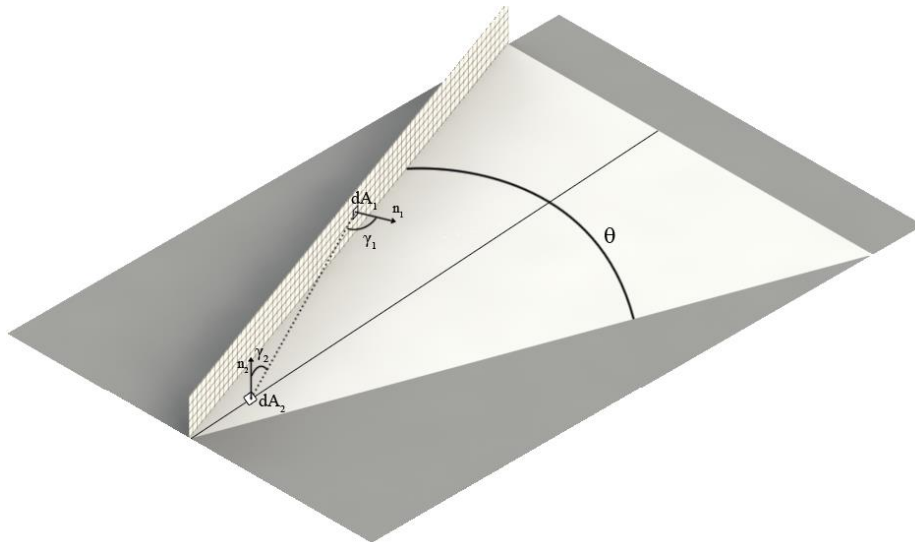


Figure 2.9: Schematic representation of the calculus of the radiative heat flux.

The hemispheric emissive power of the of the flame surface E_1 ($\text{W}\cdot\text{m}^{-2}$) is given by:

$$E_1 = \varepsilon \cdot \sigma \cdot T^4 \quad 45$$

In Equation (45) ε is the surface emissivity, σ the Stefan Boltzmann constant ($\sigma = 5.67 \times 10^{-8} \text{ (W.m}^{-2}.\text{K}^{-4})$) and T is the absolute temperature of the surface A_1 .

The view factor F_{12} can be evaluated for each geometrical configuration calculating the double integral of Equation (44). This calculation is simplified if we consider the surface that is receiving as an infinitesimal element dA_2 . According to Wong (2003) in this case the view factor is reduced to:

$$F_{12} = \frac{dA_2}{A_1} \int_{A_1} \frac{\cos(\gamma_1) \cdot \cos(\gamma_2)}{\pi \cdot r^2} dA_1 \quad 46$$

and so the density of flux radiation q_{12} (W.m^{-2}) that corresponds to the radiation flux is given by the following expression:

$$q_{12} = \frac{A_1 E_1}{A_2} F_{12} = E_1 \int_{A_1} \frac{\cos(\gamma_1) \cdot \cos(\gamma_2)}{\pi \cdot r^2} dA_1 \quad 47$$

In order to calculate the value of q_{12} for each case of flame configuration the following simplifying assumptions were made:

The flames are considered to be rectangles perpendicular to the fuelbed surface, with a fixed fire front length L_f of 5.1 m and a constant flame height H_f .

The flame surface is the emitter at a constant temperature T_1 of 1021K and is considered as a blackbody with a value of $\varepsilon=1$.

The value of the flame height H_f was taken for each fuel from the experiments performed on a horizontal fuelbed ($\alpha=0^\circ$) as this configuration is the one that is closer to the simplifications that were made in the present analysis. The corresponding values of H_f were: 0.3m for *Pinus pinaster PP*, 0.7m for straw *ST* and 1.2m for shrubs *SH* (see Table 2).

We now consider that the element of fuel surface dA_2 is placed on the OX axis at a distance $x=0.10$ m from the intersection point D . Given the symmetry of this configuration the incident radiative heat flux q received on the fuelbed surface is the double of that emitted by a single flame and given by Equation (47). The numeric calculation of $q=2 \cdot q_{12}$ was

performed using an algorithm implemented in Python 2.7 in which the surface of the flame was divided in 500x500 panels for values of θ between 30 and 180° for each fuel. Typical results of q are shown in Figure 2.10 as a function of θ for each fuel type employed in the experiments.

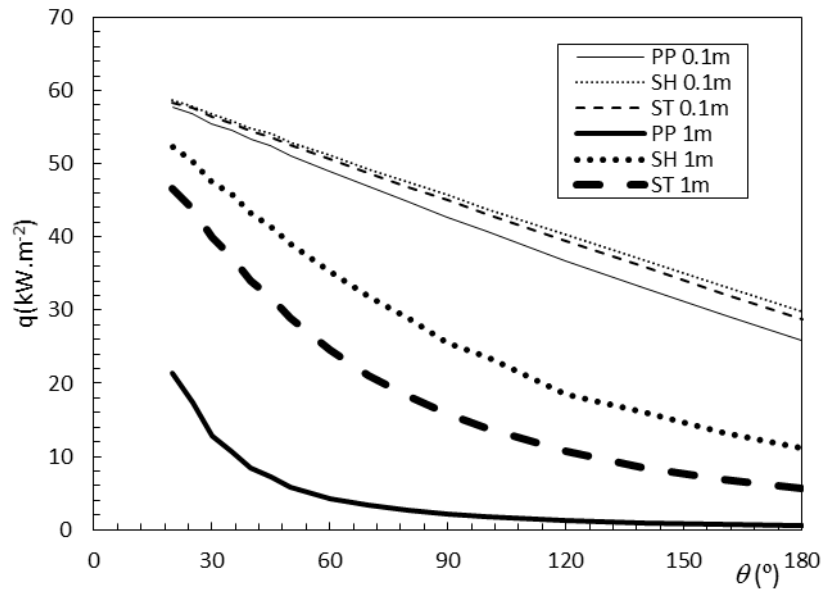


Figure 2.10: Evolution of the incident radiative heat flux q as a function of the angle θ between the flames for the three fuels considered in the present study.

Validation of the numeric calculation of q was made through a bench test in the laboratory of ADAI for different angles between the fire fronts θ_0 . The results of these tests will be presented in Chapter 4.

Chapter 3.

Methodology

3.1. Experimental Analysis

The study presented was strongly supported by experimental work carried out at laboratory scale and extended to field and wildfire scales. The experimental work progress during the doctoral program was important to better understand the phenomena of junction fires. In this Chapter the methodology applied and the parameters under control on the studied phenomena such as the angle between the fire fronts θ , the slope angle of the fuel bed α , type of fuel used and scale will be presented. The description of the test rigs and equipment used and developed in the research program progress will be the scope of this chapter.

3.2. Laboratory Experiments

The laboratory experiments were performed at the Forest Fire Research Laboratory (LEIF) of the University of Coimbra, in Lousã that is possibly one of largest facilities and better equipped in the world applied to Forest Fires research. The major part of the work has as its source the laboratory scale experiments, one of the reason for this was the possibility of collecting valid, reliable and controlled data about the phenomena during all the year, in any season, simulating the conditions observed in the real cases of the phenomena

occurrence. In laboratory it is possible to fix the values of several parameters such as fuel load, bulk density and slope and choose one of them, for instance the geometry of the fire front to change. In this form it is easier to draw conclusions about the effect of the chosen parameter. To make all the work carried out more reliable and repeatable the LEIF procedure for tests performance was followed. To avoid any bias of the data in relation to any parameter the experiments were performed randomly.

Test rig and fuel bed preparation

The main test rig used was the Canyon Table DE4, which has a useful area of $6 \times 8 \text{m}^2$ with a slope (α) that can be hydraulically changed in the range of 0 to 40° (see Figure 3.1). More details about this test rig can be found in Viegas and Rossa (2009).



Figure 3.1: Photo of the Canyon Table DE4.

For all the tests the fuel bed was designed with the desired shape of the fuel bed defined by the angle between the fire fronts θ_o for a fixed length of 5m. To do so lines were placed on the surface of the table and then this space was filled with the fuel as can be seen in Figure 3.2.

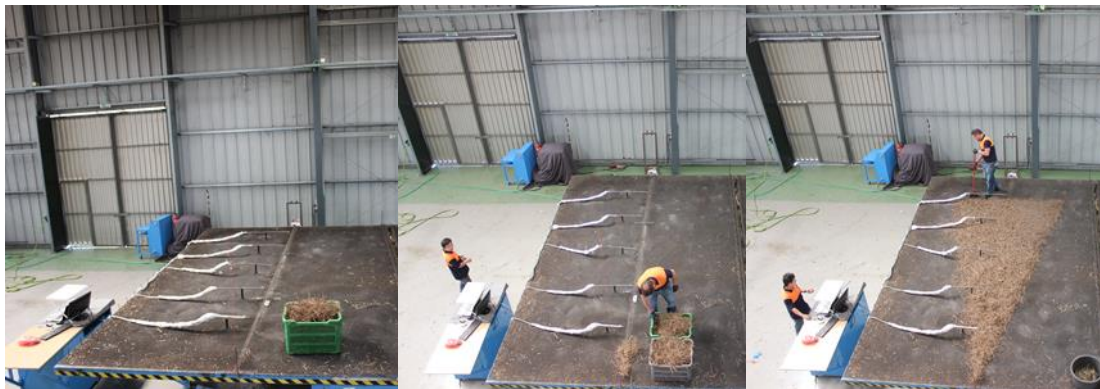


Figure 3.2: Preparation of the tests.

Then the fuel is weighted according to the area of experiment to full fill it respecting the fuel load m_c and according to the moisture content of the fuel m_f as will be explained next. The fuel is spread uniformly on the table. With a ruler a visual inspection of the fuel bed height is made in several points typically in seven points.

Fuels

In this work the laboratory experiments were carried out with three different fuel beds composed of dead needles of *Pinus pinaster* (**PP**), straw of *Avena sativa* (**ST**) and shrubs (**SH**) which is a mix of branches of *Erica umbelatta*, *Erica australis*, *Ulex minor* and *Chamaespartium tridentatum*. The characteristic properties of these different fuels are presented in Table 1.

Table 1: Characteristic Properties of the different fuels

Fuel	Symbol	Fuel bed	Residence	Bulk	Particle	Particle Surface to	Flame
		Height	Time	Density	density	Volume Ratio	Height
		h_f	t_o	ρ_b	ρ_p	σ_f	H_f
		(m)	(s)	(kg.m ⁻³)	(g.cm ⁻³)	(cm ⁻¹)	(m)
Straw	ST	0.14	42.8	4.23	0.35	50.3	0.7
Pine needles	PP	0.04	54.2	14.50	0.53	41.0	0.3
Shrubs (lab.)		0.15	65.6	3.92	0.50	69.0	1.2
Shrubs (field)	SH	0.91	286	3.64		-	-
Shrubs (Canberra)		0.4	5000	1.75		-	-

The fuel load m_c in all tests was $0.6 \text{ kg}\cdot\text{m}^{-2}$ (dry basis) like the test reported in Van Wagner (1968). In each test the moisture content value m_f of the fuel bed and the corresponding value of the basic ROS R_o were measured, these are given in Table 4. The way to get these data will be explained in the following.

Moisture content

The shape, size, density, chemical composition, fuel moisture content (FMC), among others, are important properties of the fuel beds that affect fire behaviour. The FMC (m_f) is one of the properties of the fuels that has a great importance on the fire behaviour especially in its rate of spread. According to Chandler *et al.* (1983), Byram (1959), Pyne *et al.* (1996) m_f determines the possibility of a forest fuel ignites and how much is available to make part of the combustion process (Viegas *et al.* 2013b; Fernandes 1997). Moisture content of the fuel was measured for each test or groups of tests with an A&D ML50 moisture analyser (Figure 3.3), this machine allows to know the quantity of water inside the fuel in a period of 10 minutes (Viegas *et al.* 2010), and before each test this value is determined and the quantity of fuel used is corrected in order to compensate the quantity of water inside the fuel. In this way it was granted that the fuel load used in each experiment, remains constant in all the study program.



Figure 3.3: Moisture analyser A&D ML50.

Measurement of the time of residence

The residence time t_o is a measure of the dynamic properties of the fuel bed and that is characteristic of each fuel (Viegas 2006a). It can be defined for example by the duration of the combustion reaction at a given place inside the fuel bed. This residence time was measured, according to the methodology presented by Xie *et al.* (2014), with K type

thermocouples placed in the middle of fuel bed to record the fire front advance and temperature. Temperature were collected with a frequency of 1 Hz by the array of thermocouples, the system of acquisition will be better explained bellow. When the fire front arrives near the thermocouples the temperature suffers a gradual increase then when it reaches the thermocouple the temperature increases sharply and after the passage of the fire front it decreases. The time in which the temperature remains above a certain threshold (of 350°C according to Xie *et al.* (2014)) corresponds very closely to the residence time. In Figure 3.4 the evolution of the temperature that allows the measurement of the residence time for the test CF43 ($\alpha=0^\circ$, $\theta=30^\circ$) *PP* is shown.

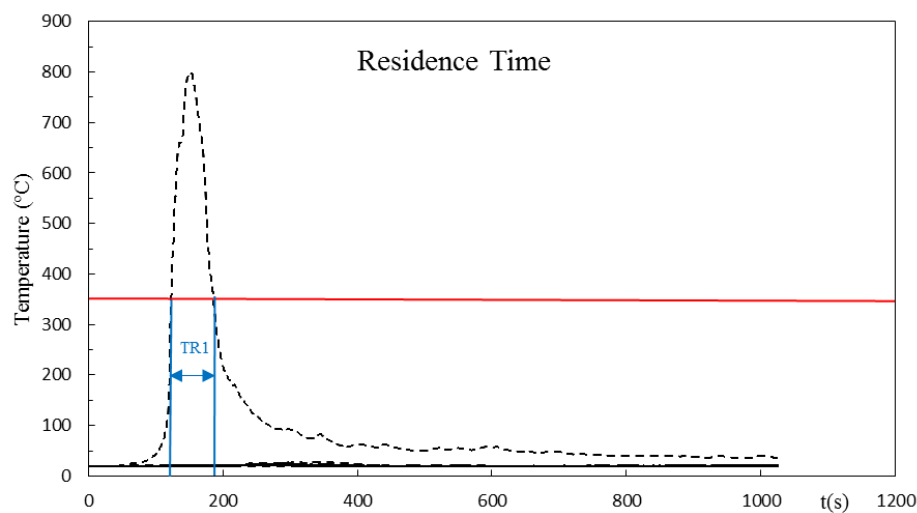


Figure 3.4: Example of measurement of the residence time t_0 .

Although the values presented in the following table are averages for each type of fuel was noticed, during the execution of the work, it was noticed that the residence time of the flames is dependent of the slope conditions (Dupuy *et al.* 2011; Xie *et al.* 2014). Despite of the observation and the hypothesis formulated, for convenience in the present work the average values still being used as reference following the common practice of assuming that the residence time is constant for a given fuel.

Table 2: Characteristic Residence time for the different fuels

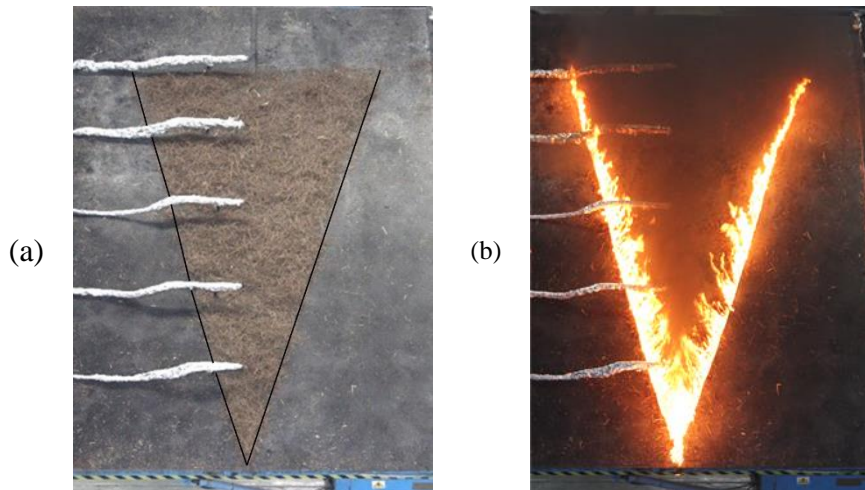
Fuel	Residence time t_0 (s)
Straw	42.8
Pine needles	54.2

Shrubs (lab.)	65.6
Shrubs (field)	286
Shrubs (fire)	5000

In Table 2 it is possible to observe, that the straw is the fuels with the lowest time residence time which is a characteristic of fine fuels. In the middle we have *Pine needles*, that represent the fine to medium fuels. At last the different residence time values of shrubs for laboratory and the field experiments. This difference is due to the dimensions of the twigs that compose the fuel bed between the shrubs of the field with larger dimension, and the shrubs collected to the lab that in the process of harvesting are cut and consequently their dimension was reduced.

Ignition procedure

The ignition of the two fire lines was made by two persons to assure that they start burning simultaneously. For this purpose two wool thread soaked in a mixture of petrol and diesel oil were used along the border of the fuelbed. Quickly the lines are set on fire by the operator Figure 3.5. The simultaneous ignition of such large fire lines is a delicate process particularly in tests with high values of slope angle.



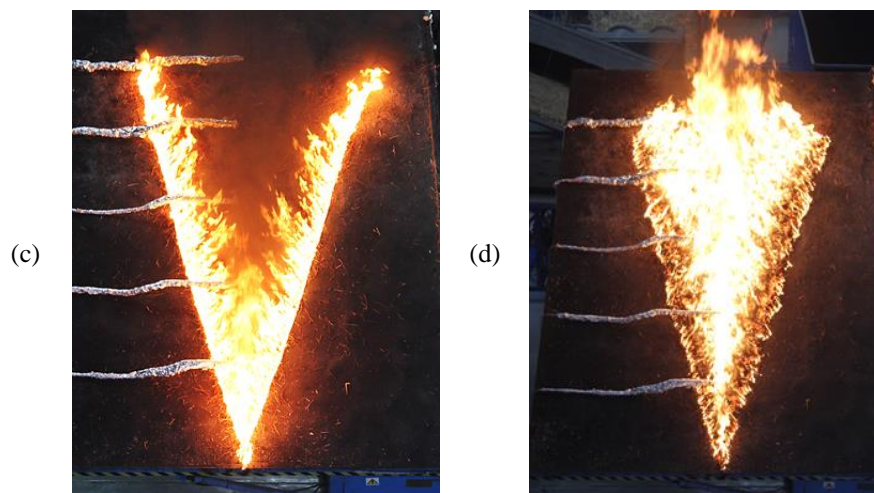


Fig. 4

Figure 3.5: General view of Combustion Table DE4 during the preparation and the performance of test CF63. (a) Reference image before the test. The Pitot tubes can be seen on the left side of the table. (b) At ignition: $t=0s$; (c) $t=2s$; (d) $t=18s$.

As these tests proceed very rapidly any slight delay in one of the ignitions or the failure of the ignition line to burn entirely as a straight line could affect the development of the test namely its symmetry conditions. Problems with the ignition possibly accounted for some of the scatter that was observed in the experimental data.

ROS measurements methodology

During the research program the results of R_D evaluation using thermocouple data or IR images were compared and it was found that both methodologies were equivalent (Viegas *et al.* 2013) but as the image analysis allowed a better temporal and spatial resolution of the processes it was the one adopted.

Thermocouples

The temperature was measured with a rate of acquisition of 1Hz using a multi-point system of 25 K type thermocouples, fibber glass and metallic shielded, with seven filaments with a diameter of 0.2mm, were placed at 20cm intervals connected to a NI cDAQ-9174 with a TC module NI 9213 that allows synchronous data-logging (Figure 3.6). From the thermocouples data and the time interval required for the fire to travel from one position to the next the ROS of the fire along OX axis was estimated as well. The presence of the fire front was assumed for values of temperature above 350°C that was considered as a sign of the existence of flame at the place and time of measurement.

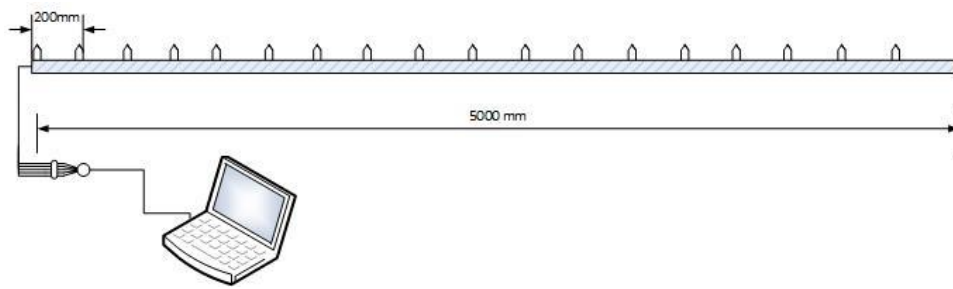


Figure 3.6: System of 25 K type thermocouples.

Infrared Images

In order to have an overall assessment of the fire front evolution during the experiment and also to analyse the spatial distribution of temperature along the fuel-bed infrared images (IR) from each experiment were recorded, using an infra-red camera FLIR ThermaCam SC660 (Figure 3.7) . The image acquisition rate was also 1Hz (Figure 3.8). Using IR methodology the position of the fire perimeter at given time frames was assessed and from these images the ROS at various positions of the fire perimeter namely at point *D* were estimated. Once again the threshold of 350°C was used to avoid the obstruction of the view by the plume of the fire. This adjustment of the threshold can be set even after the recording of the images.



Figure 3.7: Infrared Camera.

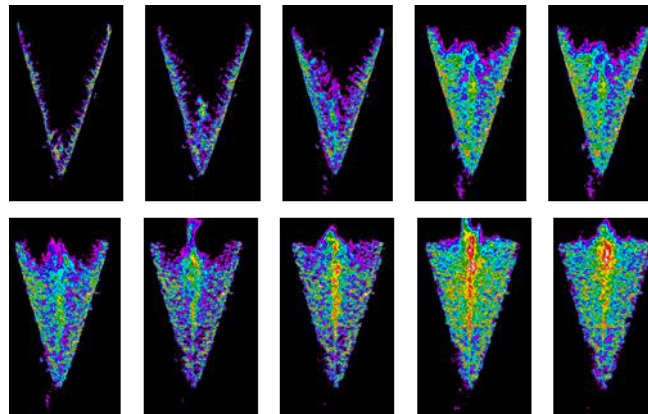


Figure 3.8: Infrared frames from a junction fire test. CF 01 (30°, 30°) PP. The time between frames is of 4s.

The procedure is the same presented in André *et al.* (2013) and which is explained here. Any digital frame of the film of the IR camera is stored on the PC hard disk frame, with the name corresponding to time t , then each frame is imported into the CAD software MICRO- STATION. On this program a specifically written macro allows the capture of the fire line, as follows. Making use of the screen cursor and the PC mouse, the user marks a discrete sequence of points along the leading edge of the fire front in the top plane of the fuel bed (at the flame's base). Afterwards, for each point, the Cartesian coordinates of the frame are converted into true physical Cartesian coordinates in the plane of the combustion table. This conversion encompasses a simple but non-trivial image calibration technique in which the camera is assimilated to a pin-hole optical system without aberration. Eventually, the fire line is described by an ordered set of points, in a Cartesian system OXY defined in the top plane of the fuel bed (parallel to the plane of the table), where: the origin O is the bottom left corner of the table, axis OY is the bottom edge of the table and the axis OX points up-slope. This simple semi-manual procedure was found to be effective in the measurement of the rate of spread (André *et al.* 2013).

The height of the flames and the angle between the fire fronts were measured as well in order to use the radiation heat flux prediction model. Besides this all the tests were recorded with a Sony high definition video camera and temporized shots were also taken with a Cannon photographic high performance digital camera.

Basic rate of spread

For each test or groups of tests a separate experiment using the same fuel bed was performed to determine the basic rate of spread R_o corresponding to the same experimental

conditions, to be used as a reference. The determination of the R_0 consists in burning an adjacent table of 1m by 1m, near the main test rig, in conditions of no wind and no slope, burn the same fuel, with the same proprieties, igniting for that a linear fire front in one of the extremities of the table. This experiment should be performed for each experiment the much closer as possible of the main experiment. Strings of cotton disposed above the fuel bed, gapped with a fixed value of 10 cm are cut during the advance of the fire front which allows to measure the basic rate of spread.



Figure 3.9: Determination of the basic rate of spread R_0 in a fuel bed of pine needles.

Rate of spread of a linear fire front in a slope

To allow the non-dimensional representation of the rate of spread R'_2 , the average rate of spread R_2 of a linear fire front spread in in fuel bed in slope conditions was determined. Auxiliary experiments were performed, with fuel beds of dead pine needles, straw and shrubs with a load of 0.6 kg/m^2 . The ignition was produced using, like in the main experiments, a wool thread soaked in gasoline and petrol (Diesel oil) to assure an instantaneous ignition at the base of the fuel bed. The rate of spread was measured with strings of cotton disposed above the fuel bed, gapped with a fixed value of 20 cm that are cut during the advance of the fire front which allows to measure the rate of spread in slope condition R_2 , presented in the Table 3.3.

Table 3.3 Characteristic rate of spread R_2 for different slopes and fuels.

α°	Fuel		
	PP	SH	ST
	$R_2(\text{cm.s}^{-1})$		
0	1.00	1.00	1.00
10	1.27	-	-
20	2.67	1.90	1.07

30	5.00	2.54	3.57
40	5.02	4.34	13.53

Pitot tubes

The pitot tubes type S were locally built following standard designs and calibrated in a wind tunnel with ambient temperature flow using high precision pressure sensors. The value of the flow velocity U as a function of the squared root of the signal (in voltage dV) that comes from the pressure transducers, gives us an almost linear relation (cf. Figure 3.10).

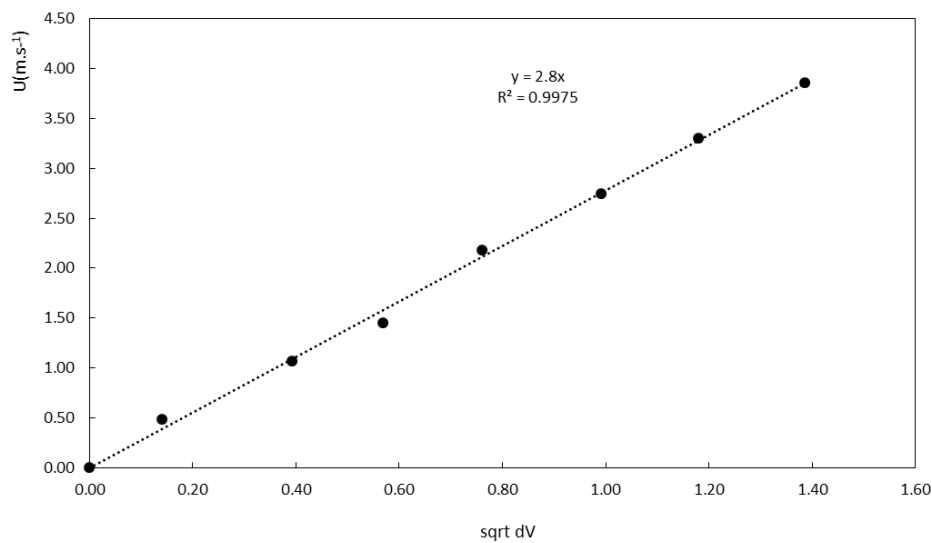


Figure 3.10: linear relation between The value of the flow speed and the squared root of the signal, in voltage, of the pressure transducers.

The flow velocity was measured at various positions along OX axis with S type pitot tubes specially designed to measure pressure differences in high temperature flows namely inside flames. In order to compensate the difference due to the increment temperature near the flames in relation to the ambient temperature the equation adopted was the following:

$$U_i(m.s^{-1}) = 2.80 \times \left(\left(\frac{T_i}{T_a} \right) \cdot dV_i \right) \quad 48$$

The Pitot tubes were placed along the centre line at a distance of 15cm above the table surface (cf. Figure 3.11) so that the tube was always above the fuel bed but inside the flame zone.

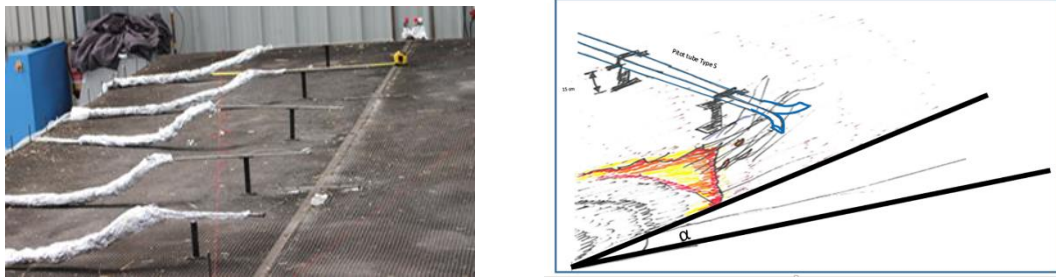


Figure 3.11: Photography of the pitot tubes and schematic representation.

In some tests three tubes were used at 1, 3 and 6m from the origin, with pitot tubes designated respectively as P1, P2 and P3; in other tests five tubes were used at 1, 2, 3, 4 and 5m from the origin. The number of pitot tubes used in each test is indicated in Table 4. Each Pitot tube was connected by pipes to a differential pressure transducer Gems 5266-50L Very Low Range Differential Pressure Transmitter (0 to 50 Pa). These transducers were connected to the NI cDAQ-9174 with a voltage module NI 9205 that performs the data-logging of the signal also with a frequency of 1Hz. The transducers are bi-directional so that when the flow is up-slope along the OX axis the signal is positive and when it is in opposite it is negative. With the data collected by this method using the values of synchronous temperature measurements by the application of a calibration it was possible to estimate the flow velocity induced by the fire phenomena. It is noticed that sometimes the flow is not aligned with pitot tubes axis of measurement, but if this drift of the flow in relation to the axis of the pitot is lower than 30° the error of measurement is very small and can be neglected.

3.3. Field Experiments

The field tests were performed in the Gestosa test field of ADAI in the Lousã Mountain (cf. Viegas *et al.* 2006), with V shaped plots with the dimensions indicated in Figure 3.12. The plots were prepared cutting shrub vegetation in the plot borders in order to have the desired V shape. The fuel height varied from 0.5 to 1.2m, the average slope of these plots is 30° and the initial angle between the fire fronts was 30° .

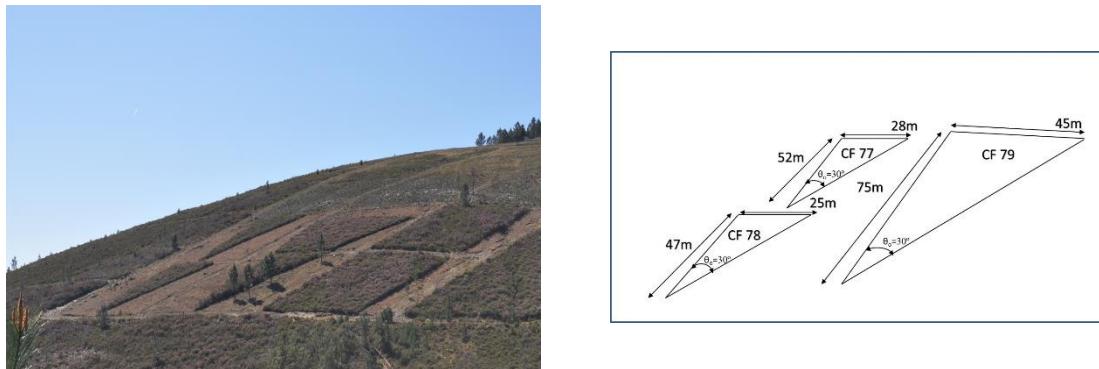


Figure 3.12: Overview of Gestosa field experiments in 2012. (a) General view (b) Dimensions of the plots.

In order to assure a simultaneous ignition of the two fire lines along their entire length pyrotechnic systems were used (Figure 3.13).



Figure 3.13: Ignition of the two fire fronts along their entire length with the pyrotechnic system in the field.

Due to the presence of lateral wind during the experiments full symmetrical conditions were not obtained but the overall results were not much different from what should be expected nominally symmetrical conditions. During these tests infrared IR and visible range images were recorded to allow fire spread analysis. One again thermocouples were placed along the central axis of the plots as in the laboratory experiments to measure the temperature evolution and consequently the rate of spread in the centre line.

The same analysis performed to laboratory experiments, seeking for the measurement of the rate of spread especially in the converging point D, was applied to these field test. The measurements made use of the IR images and the thermocouples placed along the centre line of the V shape plots burned.

In the field experiments there were not measured the flow generated inside the fire.

As shown in the Figure 3.14 in all the experimental test in the field of junction fires conduct to the formation of vertical fire whirls, sometimes more than one per experiment.



Figure 3.14: Digital photos in the experimental tests in the field of junction fires with formation of firewhirls.

Also auxiliary plots are burned in down-slope direction of propagation, with linear ignitions, to achieve the basic rate of spread in the field experiments.

3.4. Real Fire

The real fire case occurred during the merging of two large fires in the vicinity of Canberra in January 2003, creating a very intense junction fire phenomenon that actually triggered our interest on this problem. In mid-afternoon of the 18th January 2003 the flanks of Bendora and McIntyre's Hut fires merged on undulating ground covered with grass, shrubs and groups of trees under a strong wind of the order of $25\text{m}\cdot\text{s}^{-1}$. The merging of these fires developed very rapidly towards Canberra and even produced a tornado near one of its flanks. The evolution of the fire perimeters of the three fires on that day between 14.30h and 15.45h is shown in Figure 2.3. In this figure the main McIntyre's Hut fire is designated as MIH N (McIntyre's Hut North), the junction or tongue fire is designated as MIH S (McIntyre's Hut South) and the Bendora fire as BF. More details on these fires can be found in Doogan (2006); Sharples *et al.* (2012). The inclusion of this case in the present study extends widely the range of analysis of the junction fire problem. The same analysis of the rate of spread of the fire fronts was made in the real fire. In this case the data were collect from the scans made by aerial means flying over the fire and that allowed the reconstruction of the fire evolution. To estimate the basic rate of spread R_0 values we used the zones of

backward propagation of the fire which have the same order of propagations ROS as R_o , (Rossa 2009).

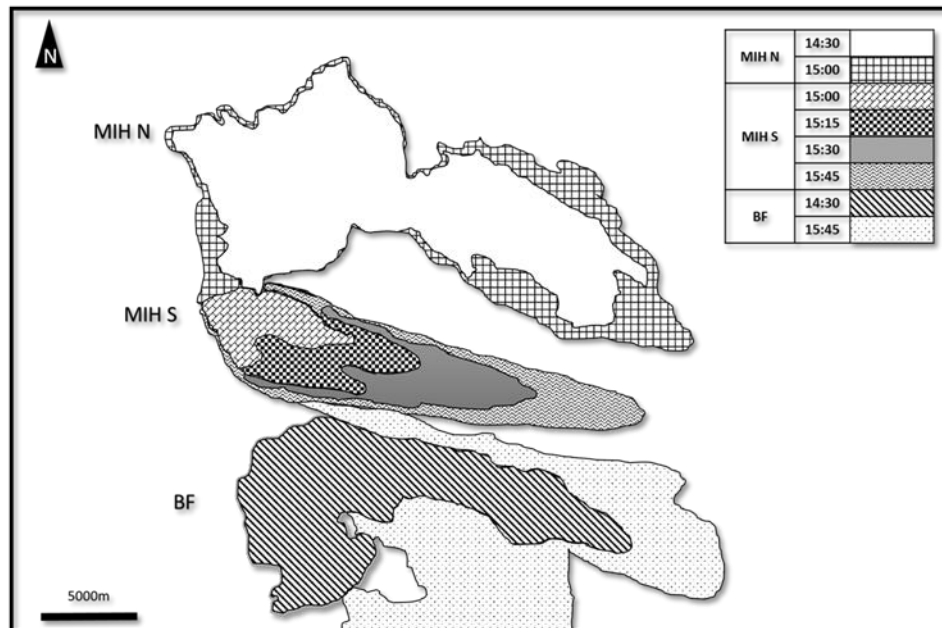


Figure 3.15: 18th January 2003, Junction fire phenomenon between the flanks of Bendora and McIntyres large fires. Schematic view of Canberra 2003 fires (Adapted from Cheney (2005))

3.5. Measurement of Radiative heat flux

Measurement of radiative heat flux for validation of the numeric calculation of density of incident radiation flux q was made through a laboratory bench test for different angles θ_o between the plates that are the source of heat as can be seen in Figure 3.16

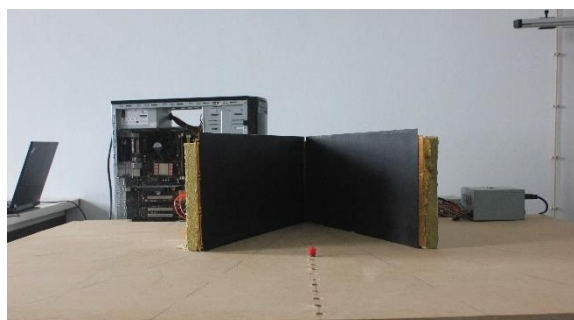


Figure 3.16: Bench test with the black heat plates.

Two steel plates (0.2m×0.6m) painted in black, were used. Three heating electrical resistances (Kapton heater mat) with 120 W of power with the dimensions of 0.2 x0.2m² were fixed to each plate. The plates represents the two fire fronts, as they are a source of

heat, with a constant temperature of 50°C of temperature. The heated plates were placed on the top of a graduated board of wood with drawn lines making angles between 20 ° to 180 ° between each other. This board has 1.50 x1.50 m² and has holes with 0.05m spacing between each hole along the axis of symmetry of the graduation lines of the angles. This drilling allowed the insertion of a heat flux sensor of Vatell of the model TG2000-0, with a resolution of 0.64 mV.(W⁻¹.cm⁻²), to measure the heat flux along the several positions from the interception point to the edge for the several angles between the fire fronts, as the sensor represents the elements of fuel being heated. The flat board was at an almost constant temperature of 20°C.

The sensor is connected to a model 9211 (± 80 mV) from National Instruments that is plugged in a chassis 9174 also from NI, this allows the continuous measuring of the signal of the sensor with a frequency of 1 Hz and loading and processing the data to a computer directly. For each sample the sensor remains 60s in this positions.

The data collected are compared with computational simulations for the same conditions here described. The discussion of the results will be made in Chapter 4, section 4.7.

3.6. Parameters of experimental tests

In Table 4 the characteristics of the tests performed in the experimental program including the laboratory scale, field scale tests and the real fire as well as the reference and the main parameters of the tests are given.

Table 4: Tests performed under the work program.

<i>Ref.</i>	<i>Designation</i>	<i>Scale</i>	<i>Fuel</i>	<i>mf</i> %	<i>R₀</i> <i>cm.s⁻¹</i>	<i>α</i> °	<i>θ</i> °	<i>Number of Pitot tubes</i>
1	CF01	Lab	PP	11.48	0.23	30	30	-
2	CF02	Lab	PP	11.24	0.24	40	30	-
3	CF03	Lab	PP	11.86	0.18	0	45	-
4	CF04	Lab	PP	11.48	0.22	0	15	-
5	CF05	Lab	PP	11.21	0.24	0	30	-
6	CF06	Lab	PP	10.74	0.25	10	45	-
7	CF07	Lab	PP	10.74	0.25	10	30	-

8	CF08	Lab	PP	10.38	0.2	10	15	-
9	CF09	Lab	PP	11.98	0.26	20	45	-
10	CF10	Lab	PP	12.36	0.22	30	20	-
11	CF11	Lab	PP	11.11	0.23	20	15	-
12	CF12	Lab	PP	15.47	0.19	0	20	-
13	CF13	Lab	PP	14.94	0.21	0	10	-
14	CF15	Lab	PP	11.67	0.27	20	20	-
15	CF16	Lab	PP	11.67	0.27	0	30	-
16	CF18	Lab	PP	11.85	0.27	30	20	-
17	CF19	Lab	PP	13.6	0.24	20	45	-
18	CF20	Lab	PP	13.6	0.24	30	45	-
19	CF38	Lab	ST	20.62	0.57	30	30	3
20	CF39	Lab	ST	14.41	0.62	30	20	3
21	CF40	Lab	ST	16.14	0.77	30	45	3
22	CF41	Lab	ST	12.23	0.73	20	30	3
23	CF42	Lab	ST	18.62	0.54	0	30	3
24	CF43	Lab	PP	17.37	0.15	0	30	3
25	CF44	Lab	PP	20.91	0.17	20	30	3
26	CF45	Lab	PP	19.05	0.17	30	30	3
27	CF46	Lab	PP	19.76	0.18	30	20	3
28	CF47	Lab	PP	19.48	0.18	30	45	3
29	CF48	Lab	SH	23.91	0.19	30	45	3
30	CF49	Lab	SH	23.91	0.2	0	30	-
31	CF50	Lab	SH	21.65	0.21	30	30	3
32	CF51	Lab	SH	18.76	0.39	20	30	-
33	CF52	Lab	SH	18.76	0.39	30	20	-
34	CF53	Lab	PP	15.61	0.24	20	30	3
35	CF54	Lab	PP	15.74	0.22	30	30	3
36	CF55	Lab	PP	15.74	0.22	30	30	3
37	CF56	Lab	SH	13.63	0.39	30	30	3
38	CF61	Lab	PP	10.01	0.23	0	30	5
39	CF62	Lab	PP	12.96	0.22	20	30	5
40	CF63	Lab	PP	11.73	0.31	30	30	5
41	CF66	Lab	PP	12.96	0.3	30	45	5
42	CF67	Lab	PP	10.8	0.26	0	30	5
43	CF68	Lab	PP	10.47	0.18	40	30	5
44	CF70	Lab	PP	10.44	0.18	30	30	5
45	CF71	Lab	PP	11.11	0.2	20	30	5

46	CF72	Lab	PP	14.28	0.3	20	30	5
47	CF73	Lab	PP	12.11	0.33	20	30	5
48	CF74	Lab	PP	12.36	0.38	30	40	5
49	CF75	Lab	PP	13.25	0.38	30	40	5
50	CF77	Field	SH	-	1.7	30	30	-
51	CF78	Field	SH	-	1.7	30	30	-
52	CF79	Field	SH	-	1.7	30	30	-
53	CF80	Fire	Canberra 2003	-	33.3	-	30	-

Chapter 4.

Results and Discussion

4.1. Fire Front Evolution

4.1.1. Overall evolution

In this section the overall evolution of the fire front during tests recorded with an infrared camera FLIR SC 660 camera will be addressed. Sample results are shown in Figure 4.1 and Figure 4.4. Focusing our attention on the advancement of fire fronts, a very slow lateral development can be observed by comparison with the areas close to the intersection zone. It is possible to observe that the major area between the fire lines is burned by the advance of the fire front near the intersection point of the two lines D . The overall spread of the fire lines consists of a rotation of each line so that the angle θ between them increases until they become a straight line ($\theta=180^\circ$).

The general development of the fire line(s) was analysed by images (containing information about the whole movement of the fire line) taken during the experiments. In the study the rate of spread will be the main parameter of analysis, as it is one of the basic parameters of the fire that can easily be used to characterize the behaviour of the fire and compare with other situations. It is widely known that the rate of spread is mainly affected by the slope, wind, fuel moisture content, fuel complex structure and width of the flame front. However, this work shows that the rate of spread can be also influenced by the geometry of the fire front.

Below we will see the effects of slope, angle between the fire fronts, fuel and scale in the evolution of the overall pattern of the fire perimeter.

Slope

In Figure 4.1 the evolution of the fire perimeter for three different slope values of 0° , 20° and 30° , the other parameters were fixed are presented. In order to make a better use of the drawing area of the evolution of the fire perimeter, it was chose not to put the dimensions and legend in these graphs. So in all of them the vertical scale corresponds to the OX axis and the horizontal scale to the OY axis. The units of the values in the scales are always given in meters. The time corresponding to each perimeter is indicated near of the correspondent line.

By the analysis of the three figures it is possible to verify that the fire perimeter advance increases with the slope angle (from Figure 4.1 a) to c)) as fire spread is higher in the central axis OX for larger values of α and consequently the adjacent points suffer a stronger advance. This results in an enlargement of the instantaneous angle θ between the fire fronts achieving values close of 180° at the end of the length of the fuelbed.

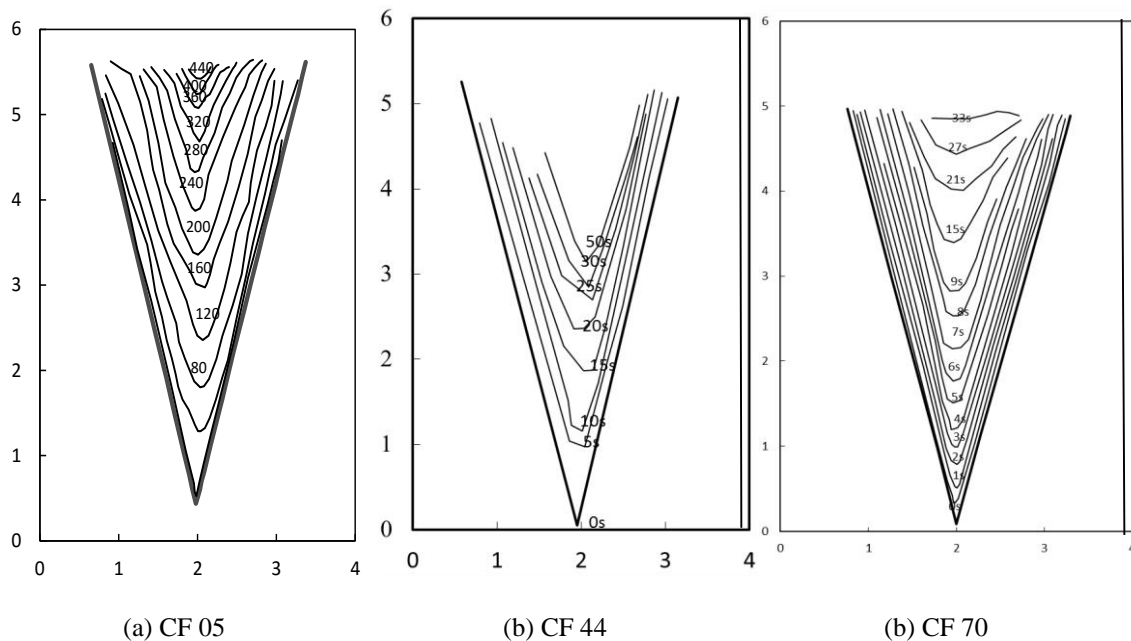


Figure 4.1. Evolution of the fire perimeter according to data obtained with IR images: Tests (a) CF 05 **PP** ($\alpha=0^\circ$); (a) CF 44 **PP** ($\alpha=20^\circ$) (c) CF 01 **PP** ($\alpha=30^\circ$). With the angle θ_0 fixed in the value of 30° The time corresponding to each perimeter line is indicated in the figure.

Taking into account the images presented it is also possible to see that the most rapid advance of the fire perimeter occurs progressively for larger distances along OY axis with increasing value of the slope angle.

Fuel

In Figure 4.2 the evolution of the fire perimeter for tests with $\theta_0=30^\circ$ and $\alpha=30^\circ$, for three different fuels used in the work, PP, ST and SH, is shown.

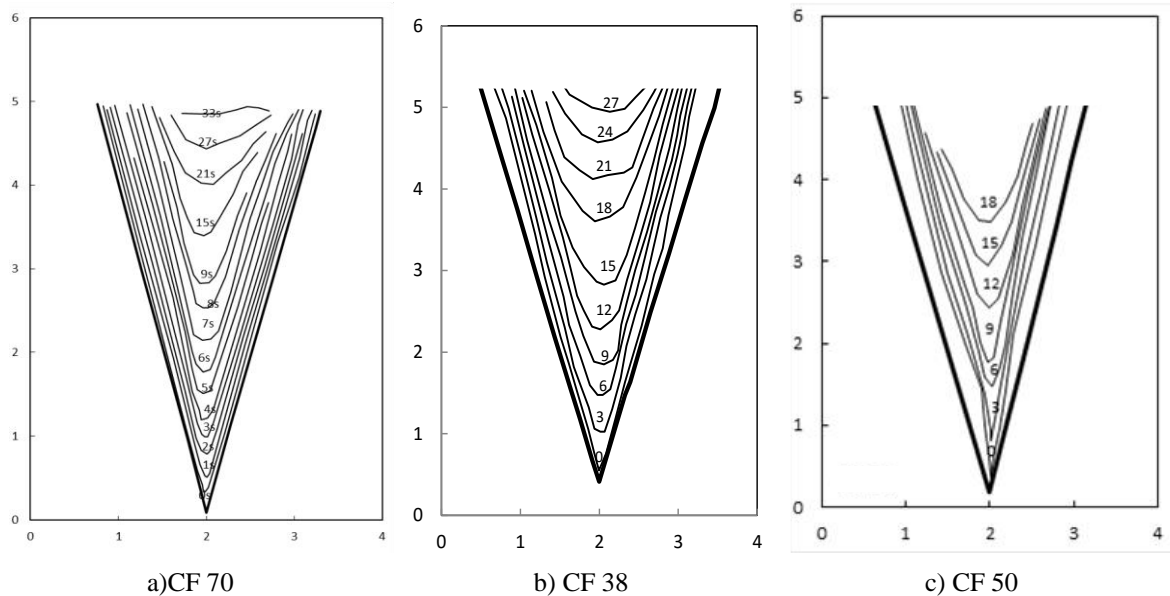


Figure 4.2: Evolution of the fire perimeter according to the images obtained with IR camera for tests with $\theta_0=30^\circ$ and $\alpha=30^\circ$. (a) CF 70 **PP**; (b) CF 38 **ST**; (c) CF 50 **SH**. The time corresponding to each perimeter is indicated on figure.

The perimeters of advancing fire fronts did not show any meaningful difference between fuels, displaying similar patterns although there are slight differences due to particle dimensions. In general we can consider that there is no great influence of fuel on the fire fronts advance pattern.

Initial angle between the fire fronts

In Figure 4.3 the growth of the fire perimeter for tests on a horizontal fuel bed made of **PP** performed with different values of the initial angle θ_0 between the fire fronts ($\theta_0=10^\circ$, 20° , 30° ; 45°) is shown.

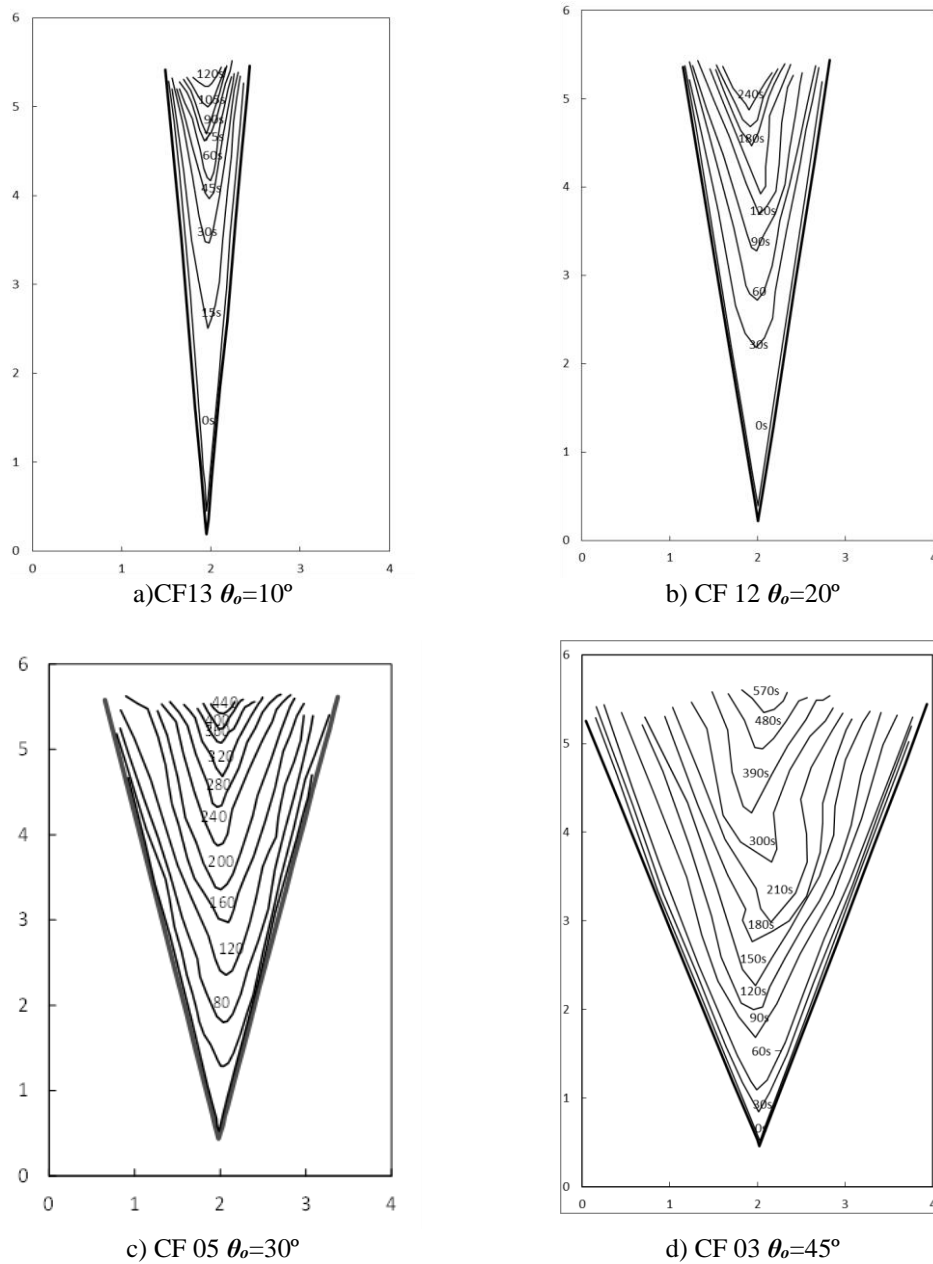


Figure 4.3: Evolution of the fire perimeter according to the images obtained with IR camera for tests with $\alpha=0^\circ$ and θ_0 changing from 10 to 20°, 30° and 45°. The time corresponding to each perimeter is indicated in the figures.

By analysis of the previous figures it is possible to recognise that the initial angle between the fire fronts plays an important role leading to different spreading conditions. Keeping the other parameters fixed it is observed that for smaller angles θ_0 fire progresses very rapidly at the intersection zone compared to the lateral spread. As the angle θ_0 increases the advance of point D is made less rapidly.

Scale

In Figure 4.4 the evolution of the fire perimeter for two tests one at laboratory scale and other at field scale with the parameters $\alpha=30^\circ$ and $\theta_o=30^\circ$ with fuel SH are shown.

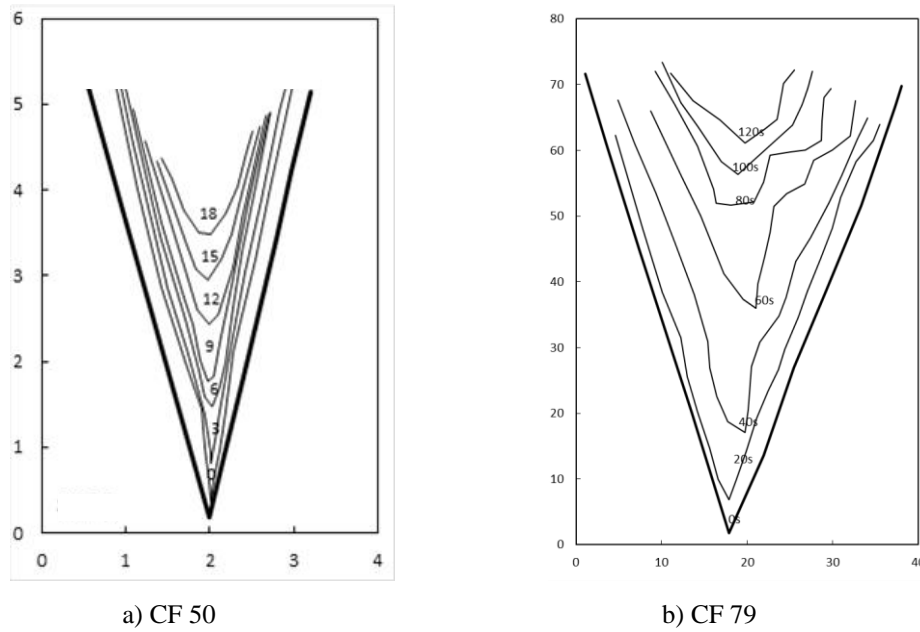


Figure 4.4: Fire line perimeters plots at laboratory scale and at field scale for $\alpha=30^\circ$ and $\theta_o=30^\circ$ with fuel SH.

From the observation of the images of the Figure 4.4 plotting the spread of fire fronts at laboratory and field scales in spite of the fact that the dimensions of the test areas are quite different it is not possible to observe significant differences in the pattern of spread at the two scales. Similar results were achieved for other tests. This rough conclusion indicates that the scale has not a relevance effect on the final results and therefore the laboratory tests results can be used to develop models that are valid for other scales. One reason for this is the fact that the problem of junction fires is defined by a single geometrical parameter that is the initial angle θ_o between the fire lines which has no dimensions.

4.1.2. Fire Line Rotation

The evolution of the instantaneous angle between fronts as function of the elapsed time is shown in Figure 4.5. a) for tests with a slope angle $\alpha=0^\circ$ and in Figure 4.4 b) for $\alpha=30^\circ$, in both cases the angle between the fronts increase rapidly to values around 60° and

afterwards there is a slower growth phase to the limit value of 180° . It was observed that this limit was only reached for tests with the fuelbed made of *PP*. It is expected that for longer tables, the tests with other fuels would also show a similar linear fire front at the end of the merging fronts. It is also noticed that this tendency to achieve a linear fire front, is more evident and faster for $\alpha=0^\circ$ than for $\alpha=30^\circ$. This is due to the fact that sometimes the fire front is not completely linear and therefore the measurement of the angle can be affected by the assumption of a linear fire front. The error induced in fitting straight lines to the fire fronts can explain some punctual decreasing values on the angle between the fire fronts in course of the time that are observed in Figure 4.5.

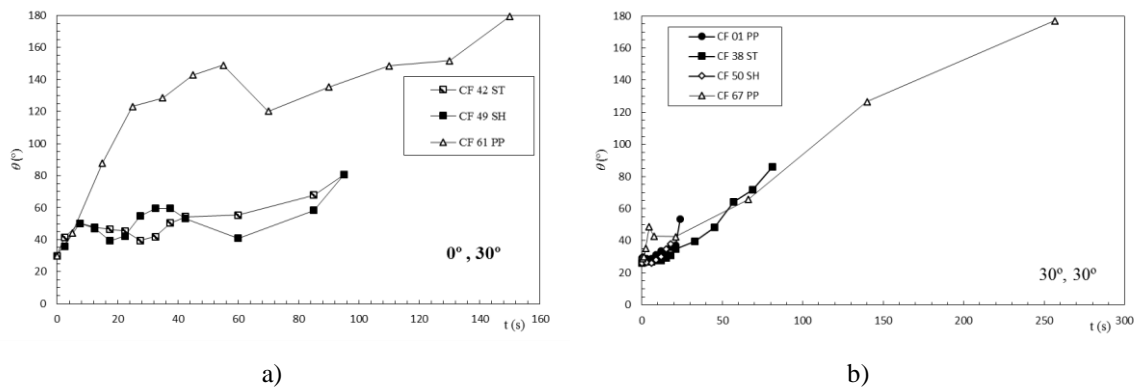


Figure 4.5: The evolution of the instantaneous angle between the fire fronts θ as a function of the time for the three fuels (PP, ST and SH). Case a) with a slope angle $\alpha=0^\circ$; Case b) Case a) with a slope angle $\alpha=30^\circ$.

The analysis of the angle θ evolution indicates that the two fire lines rotate mainly with a negative velocity ω as was already reported in (Viegas *et al.* 2012). This is a different behaviour regarding the one presented by (Viegas 2002b) in which it was reported that a fire line propagating in an up slope terrain rotates with a positive velocity ω . In both cases the velocity of the elements of the fire line will be affected by the component of the convection flow that transports heat along the fire line. This heat will be available to the adjacent elements of the fire line. As more energy is available at this adjacent element the combustion reaction will be more intense, the flame length will be higher and consequently the rate of spread will be higher in the upper parts. This leads the angular velocity to a positive value.

The explanation for these contradictory results stays on the fact that in junction fires the special configuration, in a sharp *V* shape, will preclude the transport of heat to the upper parts. The radiative and specially convective mechanisms of heat transfer will create a large amount of energy directed towards the converging point (cf. Figure 4.19) at the initial phase.

As a result these parts near the merging point will be accelerated more than the others and a negative rotational velocity ω ($^{\circ}.\text{s}^{-1}$) will arise from this process. Results of the normalized fire line rotational velocity ω' (51).

$$\beta = \left(90 - \frac{\theta}{2}\right) \quad 49$$

Here β is defined by the Equation (49) and represents the average angle between the fire fronts and the OY axis. When $\beta = 0^{\circ}$ the two fire fronts merged to become a linear fire front perpendicular to the spread direction of Point D displacement, that means axis OX (Figure 4.6).

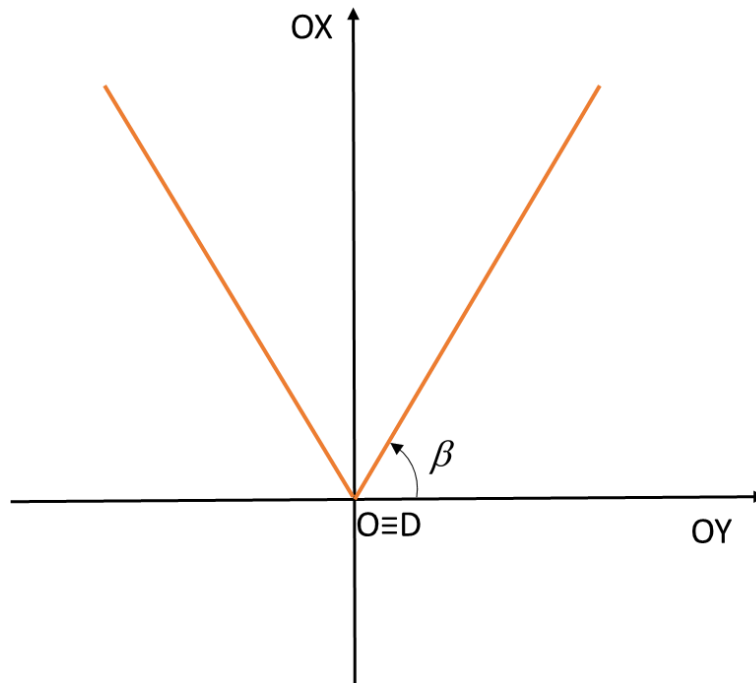


Figure 4.6: Schematic representation of the angle β that represents the average angle between the fire fronts and the OY axis.

If the two fire fronts converge with θ tending to 180° , virtually parallels, β assumes a value tending to 90° .

$$\omega = \frac{d\beta}{dt} \quad 50$$

$$\omega' = \frac{\omega}{R_o} \quad 51$$

As can be observed in Figure 4.7 a) ($\alpha=0^\circ$) the normalized rotational velocity ω' is minimum for $50^\circ < \beta < 70^\circ$ while for $\beta > 80^\circ$ its value is close to zero for the case. In Figure 4.7 b) ($\alpha=30^\circ$) the normalized rotational velocity is minimum for $70^\circ < \beta < 80^\circ$ and then for $\beta > 80^\circ$ tend to reaches values close to zero

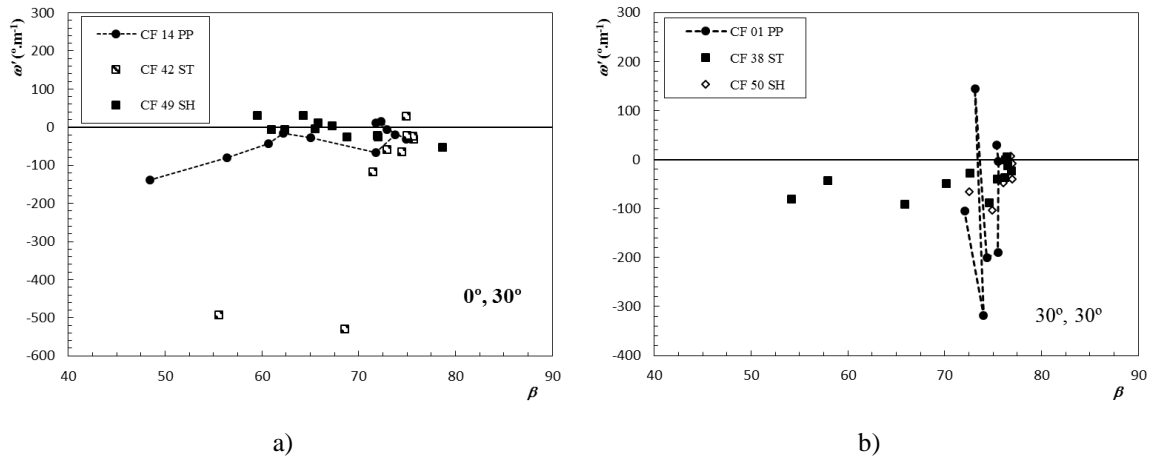


Figure 4.7: Variation of the reference rotational velocity ω' of the fire lines as a function of the inclination angle β , for the three fuels. Data points corresponding to tests with PP fuel beds with various values of slope angle are marked with lines.

Despite the data shown a deeper study of this problem is necessary to analyse it more properly possibly with a larger fuelbed length in order to make a full assessment of the fire line evolution.

4.1.3. Evolution of intersection point

The displacement of the intersection point D is crucial to understand the junction fire behaviour since this is the location where junction fires have a larger effect and the maximum rate of spread R_D is always observed. As referred in Chapter 3 two methodologies of assessment of the velocity of the intersection point R_D were used. For simplicity from now on R_D will be shortly abbreviated to R .

The two methodologies used were the IR image analysis and a beam of K type thermocouples. In order to assess the accuracy of each method in the determination of x_D and R'_D as a function of time a series of tests with PP were performed, with a $\theta_0 = 30^\circ$, for $\alpha=0^\circ$, 20° and 30° using both measuring techniques. As can be seen in Figure 4.8 the agreement between both sets of data is quite good for $\alpha=0^\circ$. However in the other two cases some discrepancies were observed, while the general behaviour is similar. For $\alpha = 20^\circ$ (Figure 4.8 b) and $\alpha = 30^\circ$ (Figure 4.8 c) it seems that there is a displacement along the time axis. It

should be noticed that the initial spread in these tests is very fast and very much dependent on the ignition conditions so we have to assume that slight differences between individual realizations of these tests may yield different results. It was found that TC technique allows a better discrimination of fire spread in the initial phase of development. Since the fire accelerates in relatively short time it is difficult to access this phase with IR images. Both techniques are therefore complementary as the TC technique provides a good assessment of the fire displacement along OX axis while IR provides an overall picture of fire evolution.

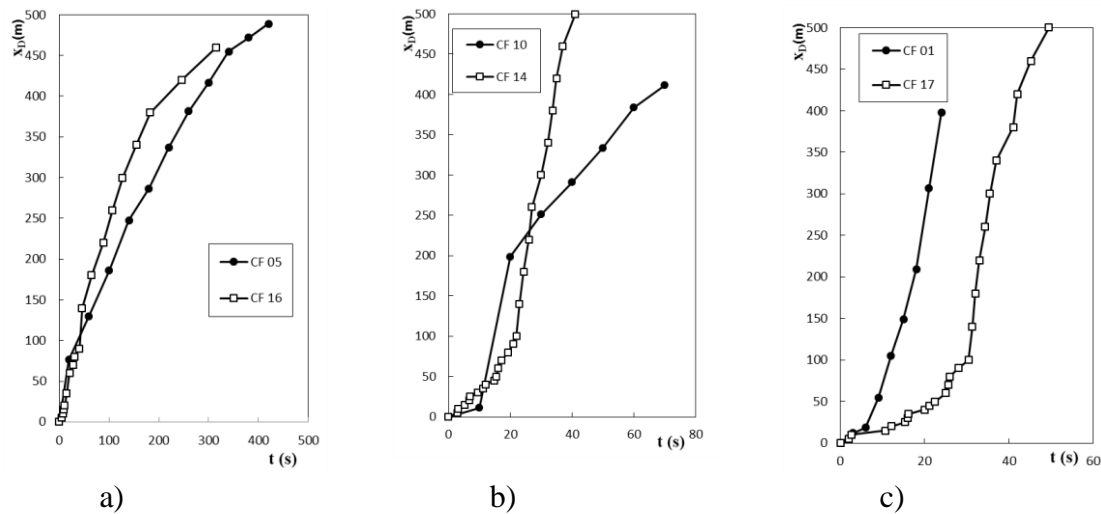
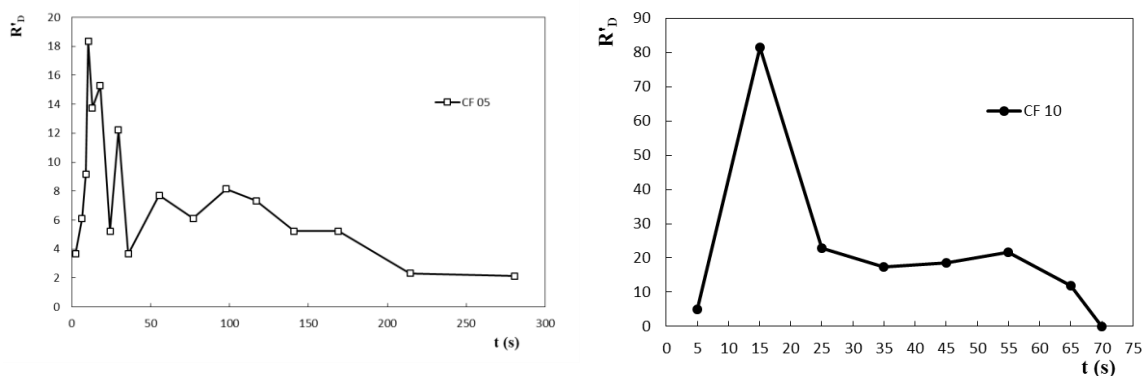


Figure 4.8 Comparison between the evolution of displacement distance x_D as a function of time measured by IR and by TC techniques for tests with PP fuel bed for three different fuel bed slopes, a) 0° of slope, b) 20° of slope and c) 30° of slope. With fix value of initial angle of the fire fronts $\theta_0 = 30^\circ$

In Figure 4.9 three typical curves, based on data from the previous figure are presented, showing the evolution of the non-dimensional rate of spread of junction fire tests with PP fuel bed for three different fuel bed slopes, $\alpha = 0^\circ$, $\alpha = 20^\circ$ and $\alpha = 30^\circ$. The value $\theta_0 = 30^\circ$ was fixed. These curves are characterized by a sudden acceleration phase until it reaches a maximum value which is followed by a decreasing phase. The duration and magnitude of each stage depends on the initial boundary conditions.



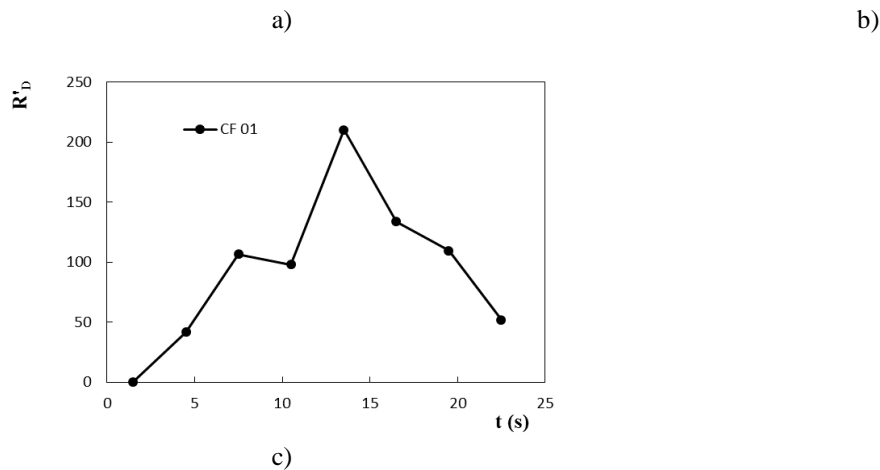


Figure 4.9 Characteristic curves showing the evolution of the non-dimensional rate of spread of junction fire *PP* fuel bed for three different fuel bed slopes, a) 0° of slope, b) 20° of slope and c) 30° of slope. With fix value of initial angle of the fire fronts $\theta_0 = 30^\circ$.

4.2. Role of Slope

In order to analyse the role of slope sample results of R_D as a function of t or x for tests with three values of slope angle, α , are shown in Figure 4.10 and in Figure 4.11. To isolate the effect of slope from the effect of fire fronts initial angle θ_0 this was fixed at 30° in all the tests presented in these figures. The increasing and decreasing phases of the rate of spread described in Chapter 2 are clearly shown in these figures. However it was notice that in a horizontal surface ($\alpha=0^\circ$) the acceleration phase is very short both in space and time while the deceleration phase is more evident in these tests. The contrary happens for $\alpha=30^\circ$ in which case the deceleration phase is not evident this meaning that on some experiments the fire accelerated over the entire length of the combustion table possibly without reaching its maximum value. For $\alpha=20^\circ$, both phases occurrence of acceleration and deceleration can be observed. The value of R_D increases with the slope angle α and the same happens with the distance or time that is required to reach it. It is considered that wind has a similar effect on R_D as slope.

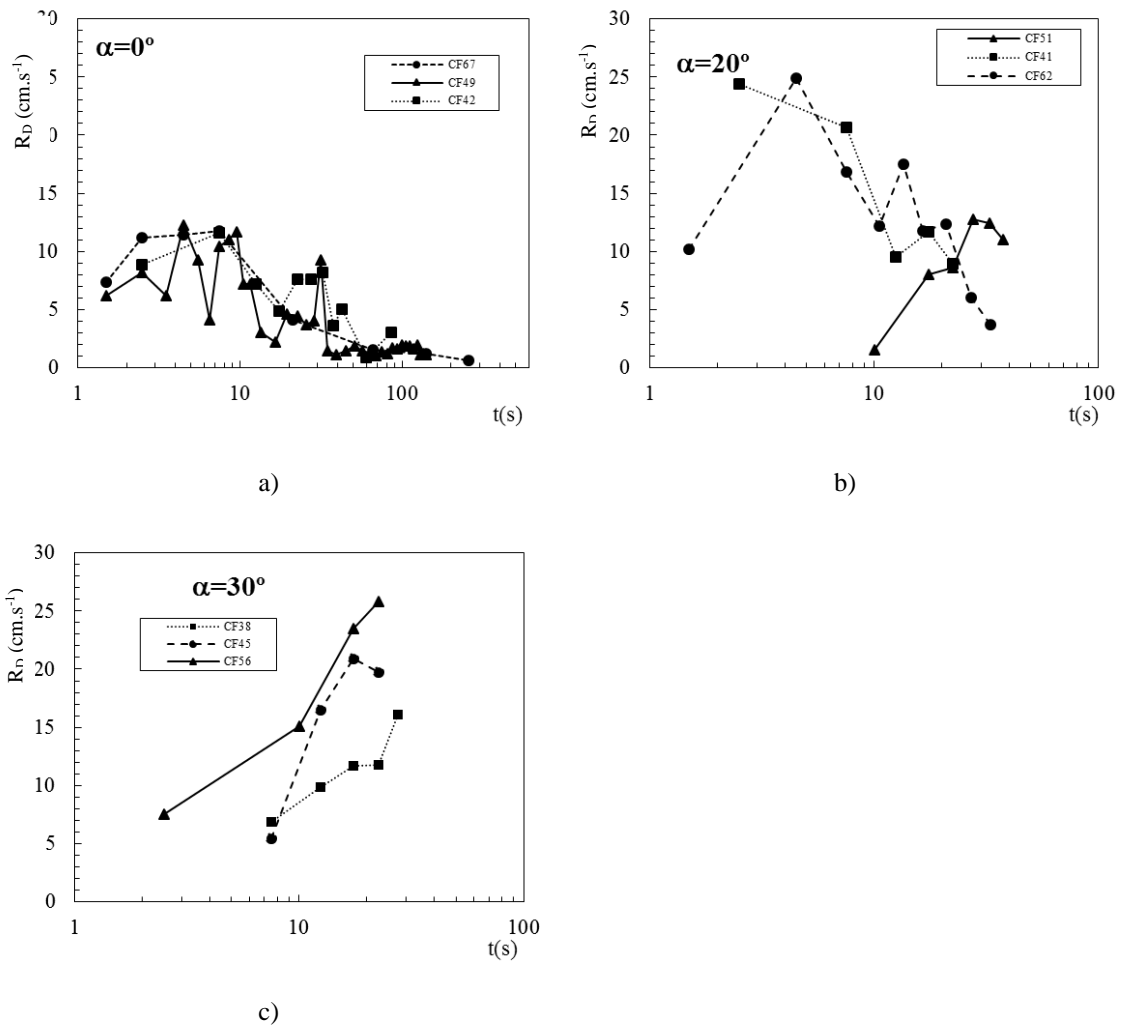
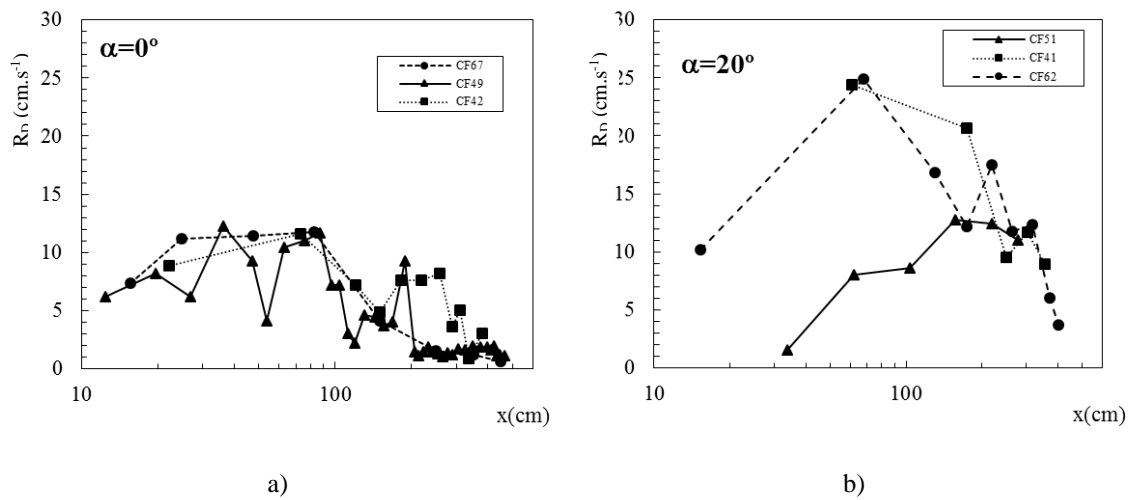
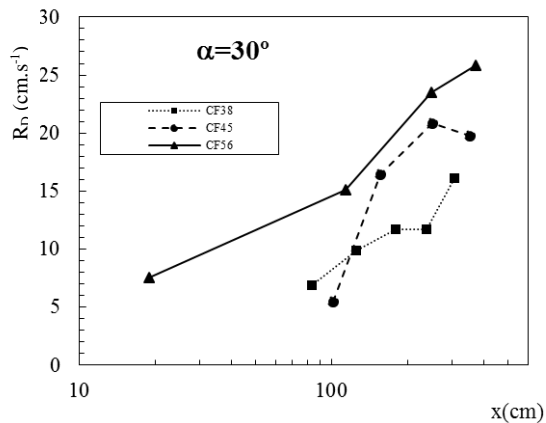


Figure 4.10: Evolution of the values of R_D for three different fuels and slope values as a function of time and (● PP; ■ ST; ▲ SH)





c)

Figure 4.11: Evolution of the values of R_D for three different fuels and slope values as a function of distance. (● PP; ■ ST; ▲ SH)

4.3. Role of Fuel

Three different fuels were used in the present study, as described in Chapter 3. The different fuels introduce slight changes due to fuel particle properties that will carry different characteristics to the fuelbed as explained before. In this section the possible influence of each type of fuel on the junction fire phenomena will be analysed.

To do so we look to the data presented in previous section, in both Figure 4.4 and Figure 4.5. These data were presented for three different configurations wherein the initial angle between the fire fronts remains fixed, with $\theta_0 = 30^\circ$. The terrain configurations were split by the slope angles α (0° , 20° and 30°) and to each set the results for the three fuels were presented. In Figure 4.4 a), all fuels drive to an acceleration tendency followed by deceleration trend, with some fluctuations in all the cases. Although the experiment CF49 (**SH**) reveals the highest R_D value of 12.23 cm.s^{-1} , this is an experiment displaying additional fluctuation.

Considering Figure 4.4 b) for $\alpha = 20^\circ$ the experiment CF 62 (**PP**) exhibits the highest value of R_D with a peak value of 24.93 cm.s^{-1} , in this experiment the trend begins with an acceleration followed by a deceleration phase. The experiment CF 41 (**ST**) presents a peak value of $R_D = 24.40 \text{ cm.s}^{-1}$ very close to the peak value of the set, although the trend of this test was always of deceleration. The experiment CF 51 (**SH**) shows a very consistent

acceleration phase, reaching a peak value of 12.74 cm.s^{-1} and starting the deceleration phase after that. It was observed that the fluctuation in this set of three tests decreases considerably.

In the set correspondent to the Figure 4.4 c) ($\alpha=30^\circ$) all the experiments behaves in the same way, exhibiting only an acceleration phase. In relation to the peak values of R_D , although initially experiment CF 56 (**SH**) presents the highest value with the evolution of time this role was shifted to the experiment CF 63 (**PP**) which presents the maximum rate of spread $R_D=26.28 \text{ cm.s}^{-1}$, this maximum is followed by a slight deceleration, that is considered as a fluctuation only. The experiment CF 38 (**ST**) presents the same trend of the others although it drove to lower values of rate of spread R_D .

Despite of the differences between the fuels the overall fire behaviour is equivalent with a similar evolution of the ROS curves, by sets. The slight differences of few seconds in the dynamic behaviour that can be observed between the tests for $\alpha=20^\circ$ and 30° for PP and SH tests can be attributed to ignition conditions. A delay of few seconds in the ignition completion may affect the variation of R_D as a function of either t or x .

In the following figures of this section derived representations of R_D as a function of t and x will be presented.

The first derived representation consists of dividing the dimensional rate of spread R_D by the basic rate of spread R_o achieving a non-dimensional rate of spread of the fire front R'_D . In Figure 4.12 the values of R'_D as function of the non-dimensional time t' will be plotted. This representation was a useful tool for the analysis of the eruptive fire behaviour in (Viegas 2006b). In the present work on junction fires this non-dimensional analysis is used again interpret the behaviour of the several fuels in the acceleration phase as will be discussed later. With this manipulation the trend of the three fuels shown in Figure 4.12 a) were collapsed in an apparent single law with a synchronized behaviour of the set of experiments that shows a short increasing (acceleration) phase until R reaches their maximum.

The maximum values R'_M for each test are now described. For experiment CF 49 with shrubs we have t' of 0.06 and a $R'=61.15$, for experiment CF 67 with pine needles for t' of 0.14 and a $R'=45.81$ and finally for experiment CF 42 with the fuel straw reaches is maximum for value of $t'=0.18$ and $R'=21.44$. After that, all the experiments starts a long deceleration phase until their R' values come closer to the reference propagation of a fire front of $R'=1$, which corresponds to the first value of the vertical axis of R' .

In the Figure 4.12 b)) it is visible that the collapse of the curves for the different fuels was not so effective however it is possible to find a common pattern of reduction of the decreasing phase. The acceleration phase until the maximum occurrence is near of $t^*=0.10$ for straw and pine needles experiments. However experiment CF 51 with shrubs seems to have a faster response to the change of slope, presenting a clear increasing phase until to $t^*=0.41$ starting a short decreasing phase after that.

The last set of experiments in Figure 4.12 c) of higher slope angle is also a very consistent group with all the experiments for all the fuels revealing the same pattern of behaviour of a clear acceleration tendency. We concluded that probably the maximum R'_D may not be achieved in these experiments as they the rate of spread continues to increase.

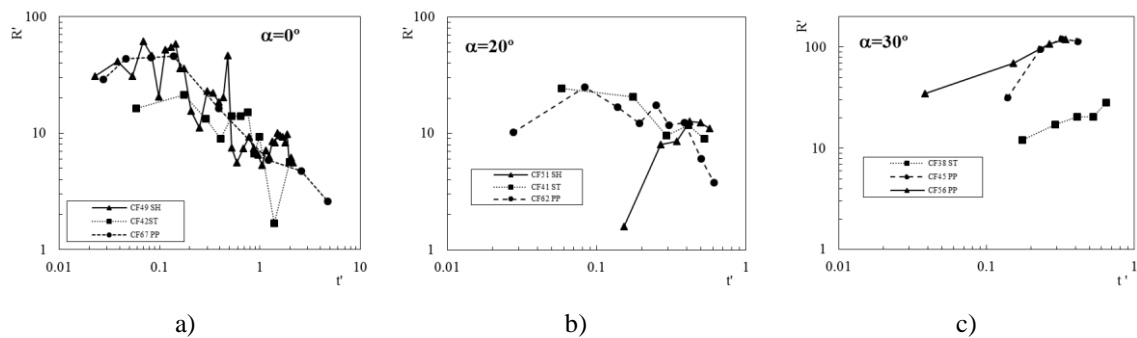


Figure 4.12: Non-dimensional rate of spread R' as function of non-dimensional time t' , for the three different fuels with the initial angle between the fire fronts θ_0 of 30° and the value of the angle of slope α varies, from 0° in a), 20° in b) and 30° in c).

Moreover the non-dimensional rate of spread R'_2 , defined in Chapter 2 as a function of the non-dimensional distance x' is presented in Figure 4.13. This representation brings some advantages because the division trough R_2 collapse in a better way the velocities. On other side the representation as a function of x' provides a better collapse of the rate of spread evolution curves in the several experiments.

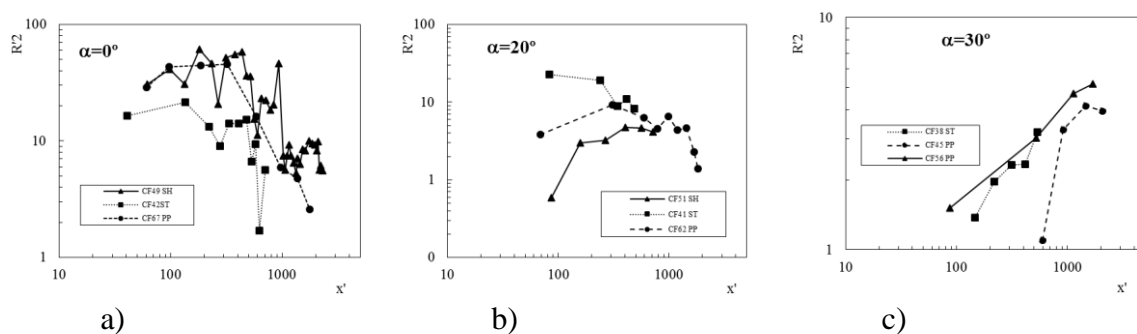


Figure 4.13: Non-dimensional rate of spread R'_2 as function of non-dimensional time t' , for the three different fuels with the initial angle between the fire fronts θ_0 of 30° and the value of angle of slope α varies, from 0° in a), 20° in b) and 30° in c).

Finally a representation involving the maximum value of ROS concept will be presented. For that in Figure 4.14 the non-dimensional form of $t^*(2)$ and $R^*(7)$ are used.

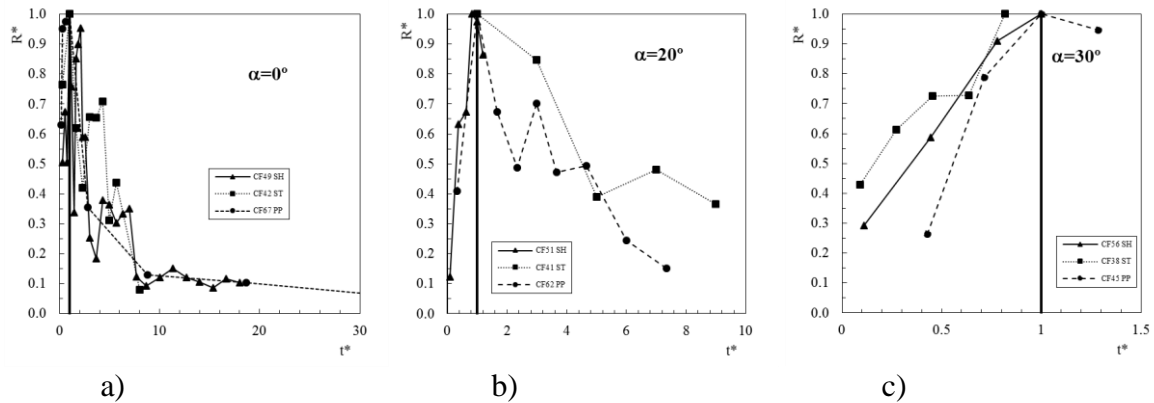


Figure 4.14: Non-dimensional rate of spread $R^*=R_D/R_{DM}$ as function of non-dimensional time $t^*=t/t_M$, for the three different fuels with the initial angle between the fire fronts θ_0 of 30° and the value of angle of slope α varies, from 0° in a), 20° in b) and 30° in c).

Despite of the different fuels, it is possible to observe a similar response in all the tests with varying slope, independently of the fuels tested. In the case of no slope (Figure 4.14 a)) a well-defined decreasing tendency was emphasised in all of experiments. In Figure 4.14 b) for $\alpha=20^\circ$ the three different fuels present values which were collapsed in similar values despite of the experiment with ST that only shows its decreasing phase. The Figure 4.14 c) presents an increasing phase with a very good agreement among the experiments with the different fuels. The entire fuelbed was consumed in a short time and the decreasing phase only appears for the test with PP (CF 45). This condition allows a simplification of analysis, making possible the extrapolation between the results obtained for one type of fuels to the others using the right parameters. In the section 4.5 on the scale effect data that reinforce this assumption will be presented.

4.4. Role of initial angle between the fire fronts

As introduced in Chapter 2 the angle between the fires fronts θ_0 is one of the most important parameters on the fire spread. This geometric parameter will affect the initial boundary conditions of the development of the fire. In (Viegas *et al.* 2012) the effect of the initial angle between the fire fronts for non-slope conditions in the rate of spread of the

merging point D was presented. In this section the effect of θ_o on the rate of spread of the merging point D for several slope conditions will be analysed. The results presented in Figure 4.15 are from experiments with dead pine needles of *Pinus pinaster* (PP).

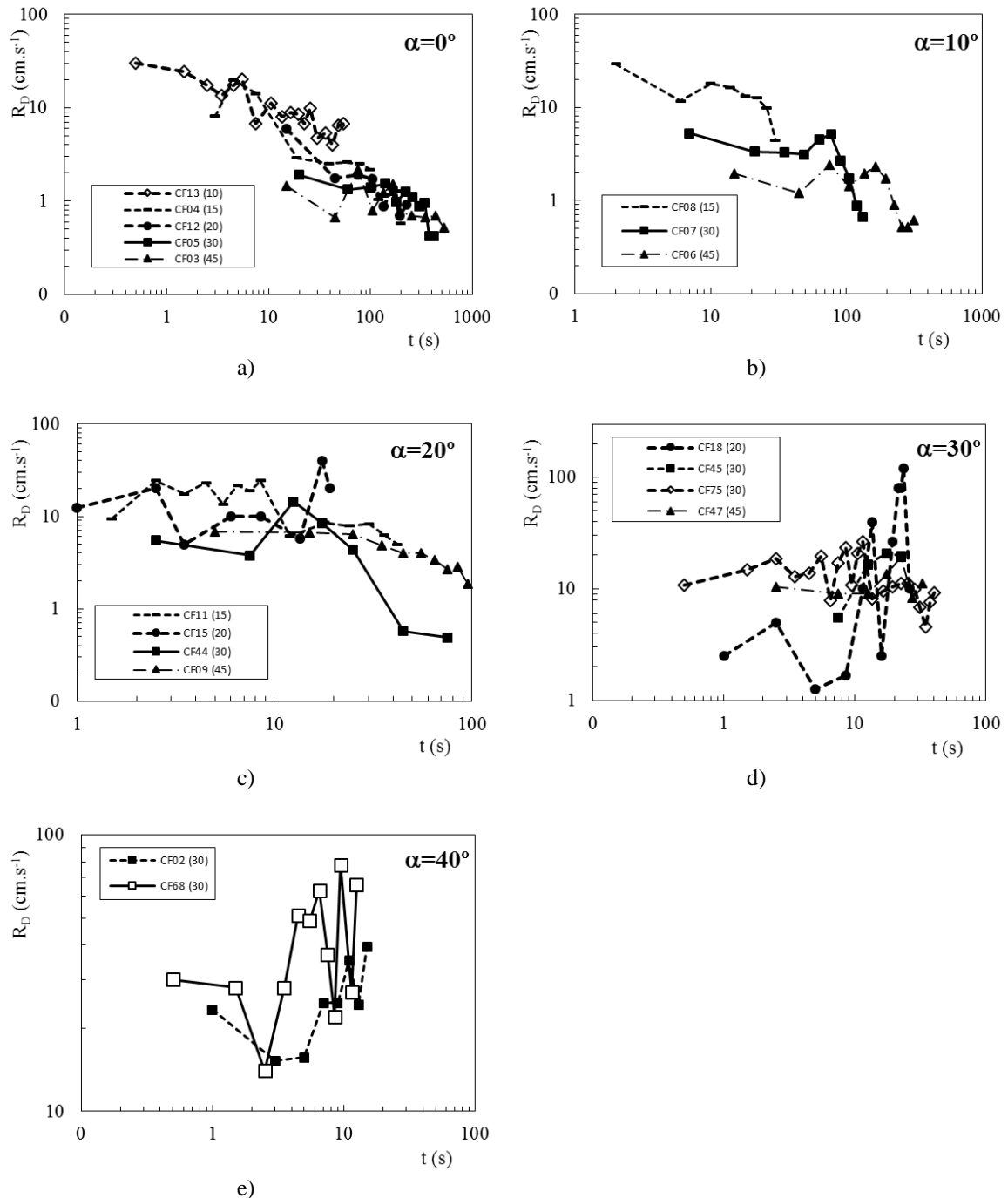


Figure 4.15: Rate of spread R_D as function of the initial angle between the fire fronts θ_o , for different conditions of slope angle, a) 0°, b) 10°, c) 20°, d) 30° and e) 40°. All the experiments are performed with PP.

By the analysis of the figures above it is possible to observe that excepting one value for $\alpha=20^\circ$ the maximum values of R_D were reached for the lower values of the initial angle between the fire fronts and decreasing for wider angles. This is strongly evident for non-slope conditions as can be observed in Figure 4.15 a). For complex conditions, with $\alpha>0^\circ$, the effect of small θ_o leads to higher values of R_D . An example of this can be observed in the experiments with 10° of slope angle (Figure 4.15 b)). In the case of Figure 4.15 c) and d) with 20° and 30° of slope, respectively, the effect of the initial angle θ_o , was not so evident. In fact, the Figure 4.15 e) slope of 40° only contains tests with angle θ_o , equal to 30° not allowing the same analysis made before. Despite this it was decided to keep this graph in this set of images to give an overall view of the entire process.

4.5. Scale effect

The present work was referred before covers a wide range of space and time scales as it is illustrated by the data shown in Figure 4.16 a) and b) (that we bring back from Chapter 2) in which the results of laboratory experiments performed with shrubs ($\alpha=30^\circ$ and $\theta_o=30^\circ$), field experiments and the Canberra 2003 fire are presented.

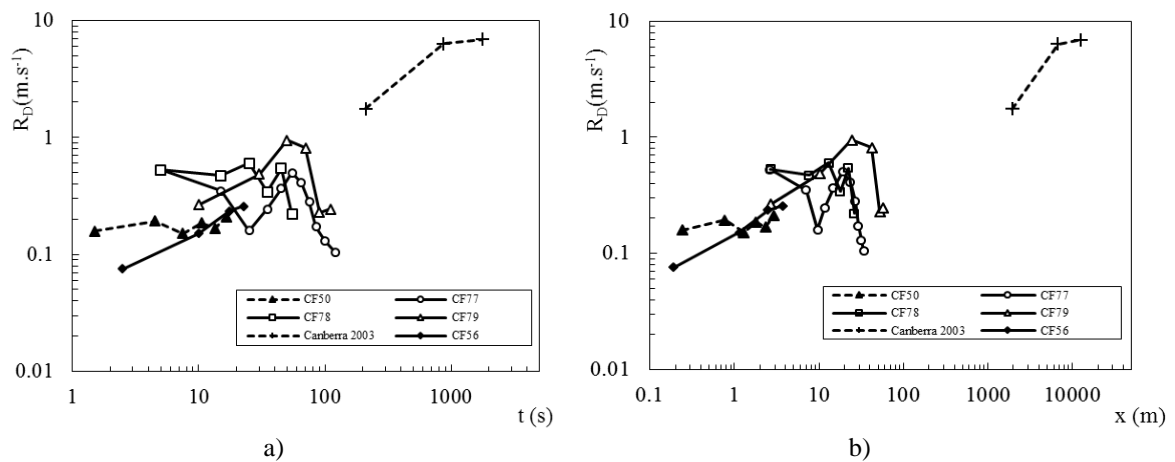


Figure 4.16: Rate of spread R_D as function of the distance (a) and as function of time (b) for tests with shrubs, including laboratory, field and a real case.

Typical dimensions of laboratory experiments are of the order of 5m (total length of the fuelbed), the field experiments are of the order of 25 to 60m while the Canberra fire event covers a distance of the order of 16000m. As can be seen in these figures the values of the ROS cover three orders of magnitude (between 0.08 and $8\text{m}\cdot\text{s}^{-1}$). On the other hand space

and time scales cover more than three and five orders of magnitude respectively. The fact that time varies in less orders of magnitude (between 0.5 and 2220s) in relation to space is already an important indication of the relatively high values of the ROS associated with junction fires. In spite of the presence of wind in the field experiments and in the Canberra fire event, the overall behaviour of the fire is quite similar and it is quite clear that the value of R_M increases with the effect of slope and/or wind on the basis of the previously mentioned analogy between slope and wind.

The similarity of the fire behaviour in this range of scales is shown more clearly in Figure 4.17 a) and b) where the non-dimensional form of (3) and (4) were used.

$$x' = \frac{x}{R_o \cdot 1s} \quad 3$$

In these figures the two characteristic phases (acceleration and deceleration) of junction fires are put in evidence. For $x < x_M$ ($t < t_M$) in the acceleration phase the value of R increases from a close to zero value to around one; for $x > x_M$ ($t > t_M$) the value of R_D decreases in a fashion that is remarkably similar for the three scales considered. These results show that the development of junction fires can be observed at various scales with some differences due to the dependence on the overall boundary and initial conditions. In spite of the fact that the intensity of the processes namely the corresponding values of the ROS and fire line intensity depend on the scale of the fire the physical processes are similar in all scales and therefore they can be studied at the laboratory scale where the control of the involved parameters and the measurements is much easier to perform. A more detailed analysis of the evolution of R^* with x^* and t^* will be made in sub-section 4.8.4.

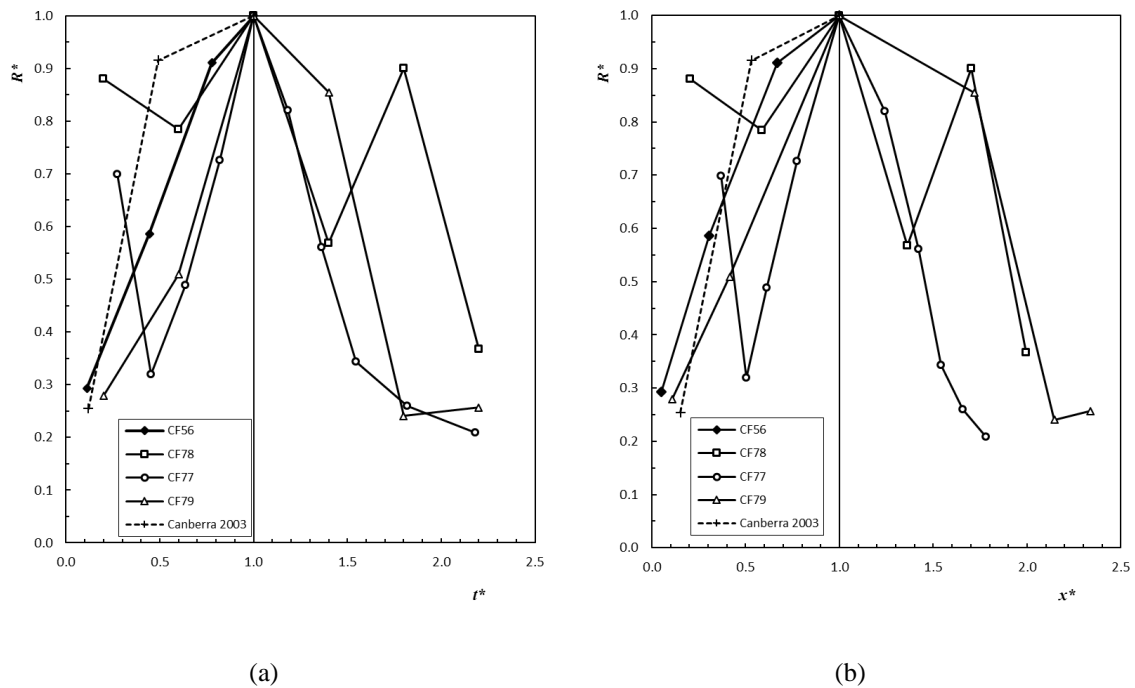


Figure 4.17: Evolution of R'_M in non-dimensional form for test with shrub vegetation at laboratory, field and real fire scales (a) as a function of t^* and (b) as a function of x^* .

Despite of the similar results it is important refer that the values obtained from the field and real fire cases can be affected by some imprecisions on the determination of the boundary conditions such as slope or equivalent wind.

We are aware that in the field the slight wind registered (about $5\text{km}\cdot\text{h}^{-1}$) can create some distortion of the angle θ_o effect. In same way the comparison with the case of the fire of Canberra 2003 can be affected by the assumption made in which the wind registered in this event of Canberra will create a similar effect to a slope of 30° . Also due to fact that we only dispose of a small number of measurements not allowing to be sure that the fire reaches is maximum during the time of analysis this may affect the shape of the curve and its parameters.

4.6. Acceleration phase

In order to analyse the evolution of the fire spread during the acceleration phase following Viegas (2006) we use the non-dimensional forms t' and R' expressed in Equation (1) and Equation (5) respectively.

Some sample values of the evolution of R' as a function of t' for various tests performed with *PP* are shown in Figure 4.18. Despite the scatter in the data the values of R' follow a similar trend of variation tending to quite large values for $t' \approx 0.3$. As a reference, the corresponding curve for eruptive fire behaviour proposed by Viegas (2006) for *PP* fuel bed is shown in this figure as well. It seems that this curve describes well the trend of the data points supporting the assumption that was made that the initial acceleration of the fire is due to convective flow induced by the fire in the same manner as for eruptive fires. The values of the relative error are in order of 45.91%. Therefore a parallelism between the acceleration phase of the junction fires and the eruptive fire behaviour is made. The rapid acceleration of the fire attributed to the development of convective flows generated by the fire itself, in the configuration of two oblique fronts making a small initial angle between them. With the evolution of the fire front, the geometry that causes this rapid acceleration will change and also the mechanisms inherent to the spread of fire. This leads to the analogy with the eruptive behaviour is only restricted.

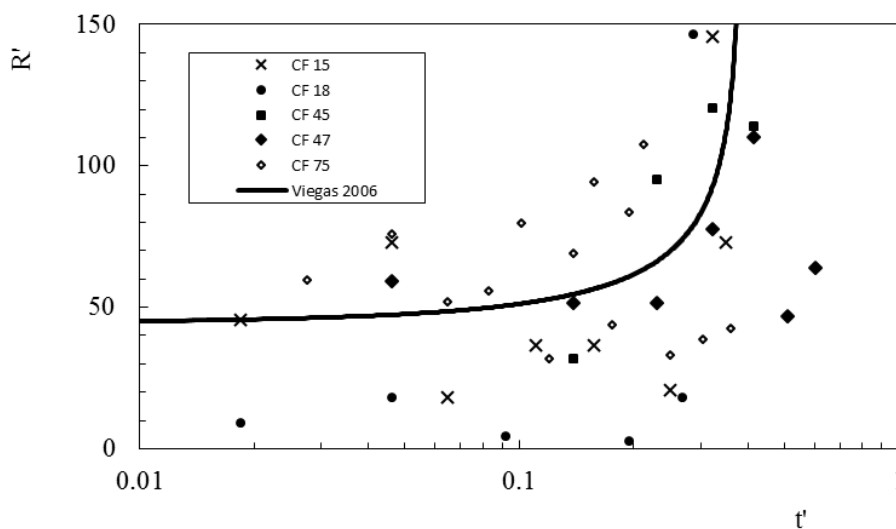


Figure 4.18: Evolution of the non-dimensional ROS R' as a function of t' during the acceleration phase for some tests. The full line corresponds to the eruptive model of Viegas (2006) for *PP* fuel beds.

In Figure 4.19a schematic representation of the evolution of the induced flow during of a junction fire is given.

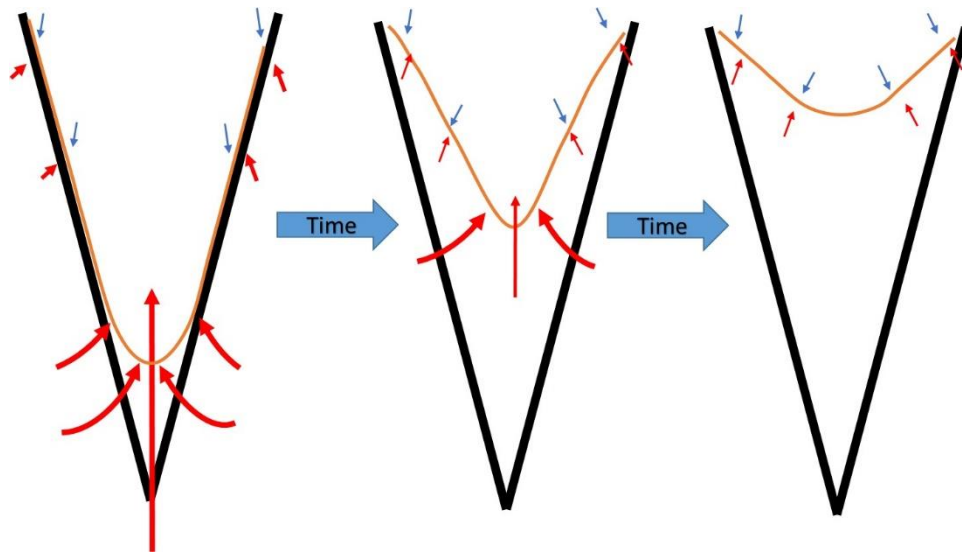


Figure 4.19: Convective flows in junction fires for different angles between the fire fronts in the course of time.

Below will be made the discussion and assessment of the data collected regarding the convective flow developed during the acceleration phase.

Flow assessment

To assess the role of convection in fire evolution we shall analyse the flow velocity measured by the Pitot tubes during four tests with *PP* performed with different values of slope angle α . We recognize that many more measuring points would be required to describe completely this very complex and time changing flow, but we assume that the single point measurements that were performed can already provide a useful insight on the convective processes inside the flames. To facilitate the interpretation of these measurements the evolution of the flow velocity U_i values measured at each station as a function of the distance $s_F = x_D - x_i$ between the Pitot tube and the fire front are shown in Figure 4.20 a), b) c) and d) for tests with *PP* with $\alpha = 0^\circ, 20^\circ, 30^\circ$ and 40° respectively. Negative values of s_F correspond to velocity measurements made before the passage of the fire. As can be seen in these figures before the passage of the fire front ($s_F < 0$) the flow velocity is practically equal to zero or slightly negative (corresponding to inflow towards point *D*) and then increases when the fire front approaches the position of the pitot tube reaching maximum values when the fire front is at some distance from the pitot decreasing afterwards. The peak values of U_i are registered usually by pitot tube P3 and increase with slope angle α . This flow velocity is of course

induced by the fire and it is consistent with the hypothesis of a partial eruptive behaviour of the fire during this acceleration phase.

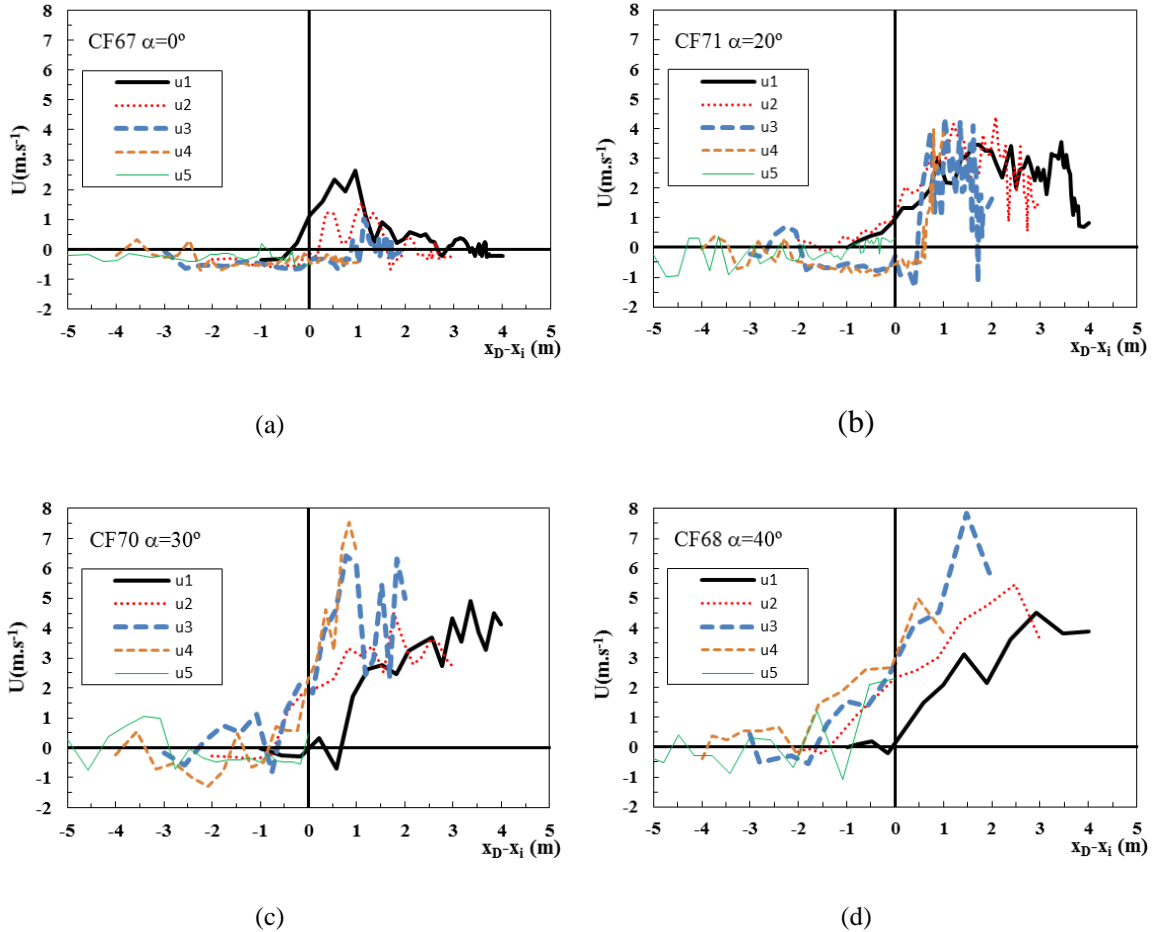


Figure 4.20: Flow velocity measured at each Pitot tube as a function of the distance $s_F=x_D-x_i$ between the fire front and the Pitot tube position for tests with *PP* for: (a) $\alpha=0^\circ$, (b) $\alpha=20^\circ$, (c) $\alpha=30^\circ$ and (d) $\alpha=40^\circ$.

The analysis of the evolution of the flow velocity at the fire front before and after the fire reaches its peak value R_M is of particular relevance. The value of $U^*=U_i/U_M$ in which U_i is the value of the flow measured at the exact time when the fire was passing by the Pitot tube position ($s_F=0$) and U_M is the value of the flow at the time instant of R_M occurrence.

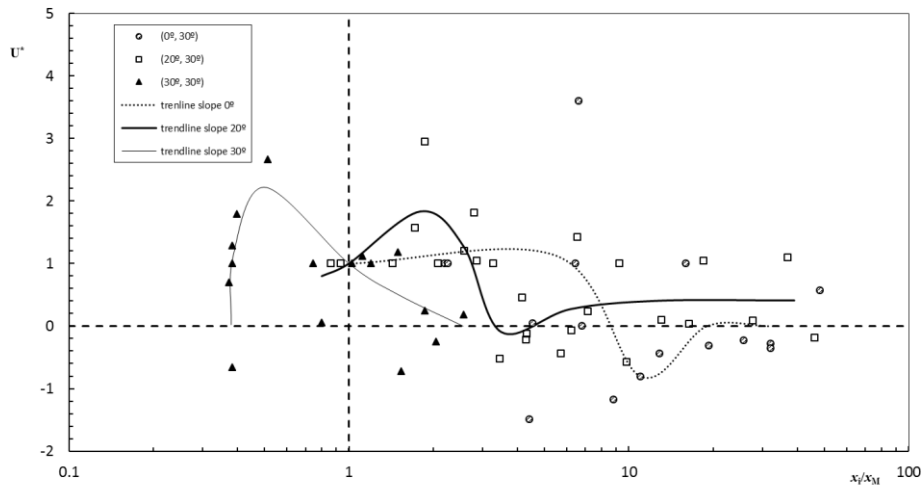


Figure 4.21: Flow velocity U^* measured when the fire front passed by the Pitot tube as a function of the relative distance in relation to the position x_i/x_M . The line is only indicative of the trend to the overall distribution of flow velocity for each set of slope.

In Figure 4.21: Flow velocity U^* measured when the fire front passed by the Pitot tube as a function of the relative distance in relation to the position x_i/x_M . The line is only indicative of the trend to the overall distribution of flow velocity for each set of slope. Figure 4.21 the values of U^* as a function of x_i/x_M were plotted, the parameter x_i is the ordinate of the pitot position (that coincides with the fire front) and x_M is the distance travelled by the fire fronts until R_M occurrence. In this figure only results from tests with PP and the initial configuration angle θ_0 equal to 30° , for slope α of 0° , 20° and 30° were plotted. The parameters of the tests used in Figure 4.21 can be seen in Table 4.

In spite of the dispersion of data some trends can be identified as indicated by the lines built from the connection of the average values of the data sets and that are indicative of the flow velocity field at the fire front.

For different slope conditions the trend of the curves are slightly different. With the increase of the slope angle α the maximum relative flow velocity which is essentially positive occurs gradually earlier and its magnitude increases. On the other hand the contrary flow, correspondent to the negative values of the flow registered decreases in magnitude and eventually even cannot be noticed for higher slope angles as is the case 30° .

A more detailed description of each curve is given just below. For $\alpha=0^\circ$ the flow velocity registered starts to be positive and has a smooth increase until the maximum and

then at a certain distance $x \gg x_M$ decreases becoming negative with a magnitude similar to the positive maximum after that the value of U^* stabilizes and becomes almost zero. This fire induced flow velocity decrease means that the flow reaches a maximum value and then starts to decrease and eventually blows in the opposite direction slowing the fire which is consistent with the present observations.

For $\alpha=20^\circ$ the flow velocity is positive and continues to increase until the maximum value and then decreases becoming slightly negative at a certain distance $x > x_M$ after that the value of U^* stabilizes at a positive value close to zero.

For $\alpha=30^\circ$ the flow velocity is essentially positive the maximum is reached sharply for $x < x_M$ and after that the flow starts to decrease to values close to zero, no negative flow is registered. This behaviour is consistent with the evolution behaviour of the rate of spread registered for tests with high slope angles $\alpha=30^\circ$ or 40° that have in the majority only increasing phases of the ROS.

4.7. Deceleration phase

In this work a model of radiation to explain the variation of the ROS for the final deceleration phase of the fire is proposed. Although it is known that both convection and radiation still to affect the fire evolution on this phase.

In order to assess the relative roles of convection and radiation during the deceleration phase we analysed the data points corresponding to $x > x_M$ (or $t > t_M$) from a series of tests. A sample of these results is shown hereby in order to illustrate our perspective.

To evaluate the role of radiation flux on a typical element of the fuelbed surface we analysed the evolution of the angle θ between the two fire lines for tests with $\alpha=0^\circ$. The results of $\theta(t)$ obtained for tests performed with *PP*, *ST* and *SH* are shown in Figure 4.22. As can be seen in this figure the overall angle θ varies between 30 and 180° corresponding to the alignment of the two fire lines in a direction perpendicular to *OX* axis. The experiments made with *ST* and *SH* do not provide such a good definition of the fire fronts and of their angle θ . This is the reason why the curves for these two fuels are not equal to the ones obtained with *PP*.

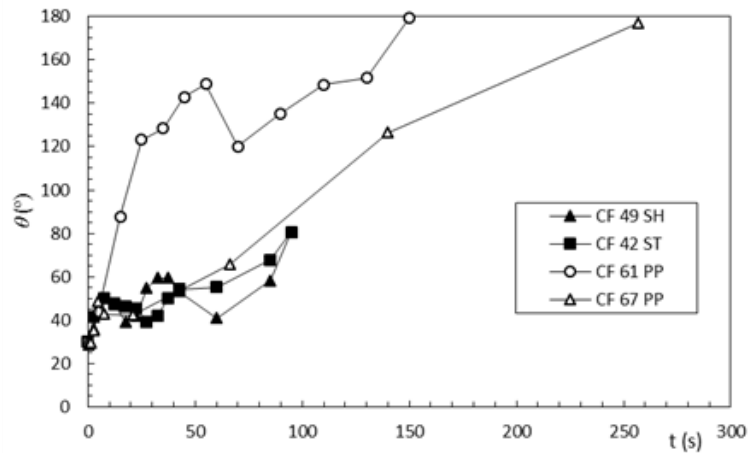


Figure 4.22: Evolution of the angle between the fire fronts as a function of time for tests performed with different fuels in zero slope conditions ($\alpha=0^\circ$).

For each value of θ according to the computation performed using the model described in 2.2.3 we can determine the corresponding value of the density of incident radiation flux q . These computed values were validated through small scale tests performed in laboratory where we measured the heat flux emitted by two metal plates at a constant temperature of 50°C as described in Section 3.5. The comparison between the numerical simulation and the laboratory experiments is presented in the Figure 4.23, for the same conditions of geometry and temperatures. As can be observed, if we neglect the fluctuations of the laboratory results the values are quite similar for the simulations and the experimental data both in order of magnitude as in tendency. For the junction fire configurations (20° and 40°) the heat flux decreases with the inverse of the distance. For the case of $q=20^\circ$ there is an edge effect around 60 cm due to the limited length of the plates but this feature is well reproduced both by the numerical model and by the laboratory measurements. For the linear fire front configuration (180°) the tendency is the same in both sets of data with decrease of the flux with the inverse of the square of the distance. In all numerical simulations of the flux the value for 5 cm is very low. This is due to the low view factor that results from the calculus on the element dA_2 that is very close to the large surface A_1 .

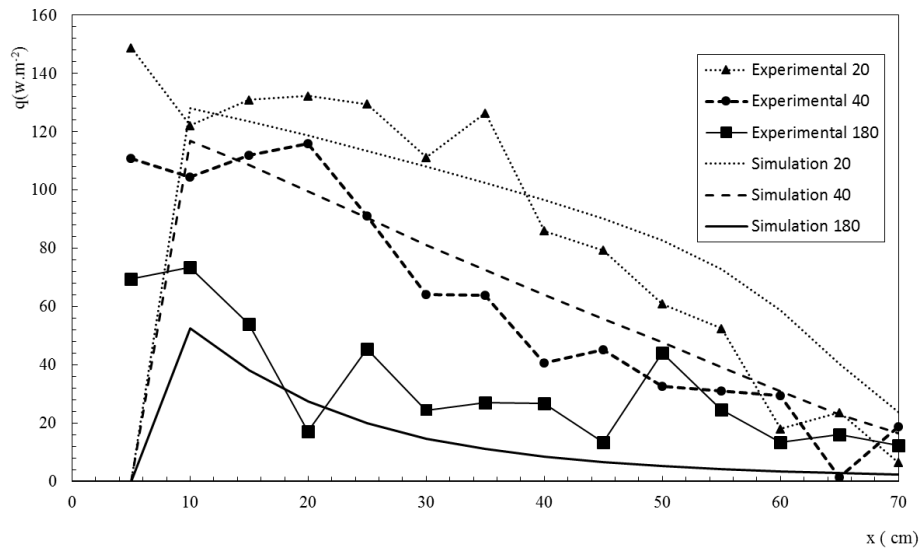


Figure 4.23: Comparison of the values of q by experimental measurements and by simulation. The angle between the two surfaces is indicated in the legend.

With the computed values of the heat flux q and knowing the value of R_D that corresponds to each data point we can establish a relationship between R_D and q as shown in Figure 4.24.

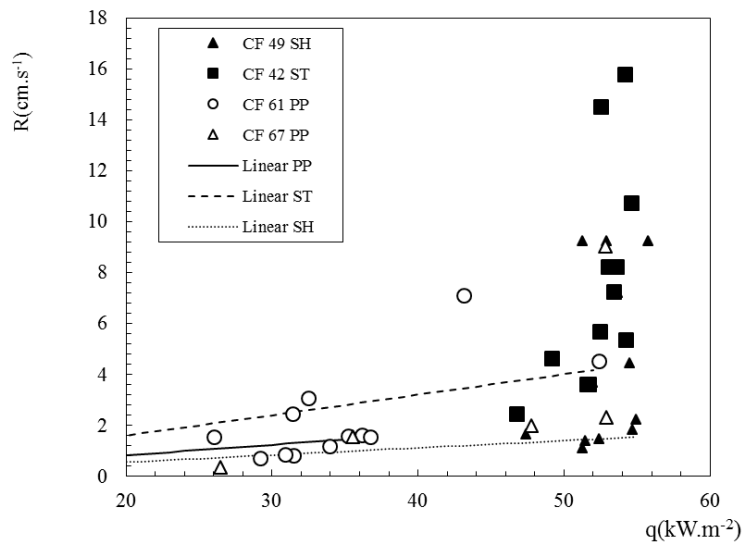


Figure 4.24: Rate of spread in the deceleration phase as a function of the calculated density of radiant heat flux for tests performed with different fuels in zero slope conditions ($\alpha=0^\circ$).

We now return to the propagation heat flux Equation (42) that establishes a linear relationship between the ROS and the propagation flux aiming the assessment of the relative roles of radiation and convection in fire propagation during the deceleration phase.

Comparison between the value of R_D and q for each data point in Figure 4.24 shows two different regimes in the evolution of $R_D(q)$: (i) for low values of q the values of R_D increase more or less linearly with q ; (ii) for values of $q > 50 \text{ kW.m}^{-2}$ the values of R_D increase very rapidly with q and a linear behaviour is no longer observed.

As was referred in 4.6 in the initial stages of fire deceleration ($t > t_M$) the flow velocity at the fire front is still positive with relatively high values and therefore the contribution given by the convection to fire spread cannot be neglected. In the final stages of fire deceleration the linear relationship between R_D and q can be accepted.

For convenience we write (42) and (43) as:

$$R_D = k_1 \cdot q = k_2 \cdot \frac{h_f \cdot \xi}{\varepsilon_R \cdot Q_{ig}} \cdot q \quad 52$$

In this equation R_D is expressed in (cm.s^{-1}); q in (kW.m^{-2}); Q_{ig} (kJ.kg^{-1}) and h_f in (m). The values of Q_{ig} were calculated using the model proposed in Pastor *et al.* (2006). The values of h_f , ξ , ε_R and Q_{ig} for each fuel are given in Table 5. The units of k_1 and k_2 can be deduced from Equation (52) and are not indicated in the Table.

Using the data shown in Figure 4.24 linear correlations were established between R_D and q for $q < 50 \text{ kW.m}^{-2}$, the corresponding values of k_1 are given in Table 5.

As the fuel beds considered in the present study have the same fuel load the value of k_2 should be the same for all of them.

Table 5: Values of Parameters for each fuelbed.

Fuelbed	k_1	Q_{ig}	ε_R	ξ	$k_2 \times 10^4$
	*	kJ.kg^{-1}	-	-	*
PP	0.0415	701	0.90	0.0115	1.94
ST	0.0803	909	0.91	0.0114	3.47
SH	0.0281	1043	0.94	0.0142	7.64

* The units can be deduced from Equation (52).

Using the previous results of k_2 can be evaluated the results given in Table 5. Even not being equal the values of k_2 are of the same order of magnitude. Taking into account all the assumptions that were made in the adoption of the model proposed (Equation 52), we take this result as an indication that the model of radiation can be adopted to explain the variation of the ROS for the final stages of fire deceleration phase. We are aware that the role of negative flow ahead of the fuelbed cooling it and reducing the combustion reaction inside the fuelbed at this phase cannot be discarded. In the initial stage of deceleration radiation alone cannot be accepted as a main driver of fire propagation. More tests have to be performed in order to better validate the present conclusions.

4.8. Predictive Mathematical Models

In this Section we aim at developing general empirical laws of fire behaviour, which can be used to predict the evolution of a junction fire episode, namely the evolution of R as a function of the independent parameters namely time, t , distance x , slope angle α and angle between fire fronts θ_o . In order to achieve this sub-models for the maximum ROS reached (R_M), for x_m and for t_m are proposed initially. Finally a model for the entire evolution of the ROS as a function of either x^* or t^* will be introduced.

4.8.1. Maximum ROS (R_M) analysis

The analysis of the R_M is presented as the first step to define some base modelling functions of the evolution of this parameter as function of the initial angle between the fire fronts θ_o and the slope angle α . In this analysis only data from experiments performed with needles of *Pinus pinaster*, **PP** were used. Values of non-dimensional maximum rate of spread R'_M were used to avoid influences of moisture content m_f on the data. Two models will be used to fit the rate of spread R'_M independently and the results achieved will be compared.

Model 1

A relationship between the evolution of the maximum rate of spread R'_M (average values) depending on the initial angle between the fire fronts θ_o , in series in which the slope

value remains fixed ($\alpha= 0, 10, 20$ or 30°), like those presented in Figure 4.25, was firstly analysed.

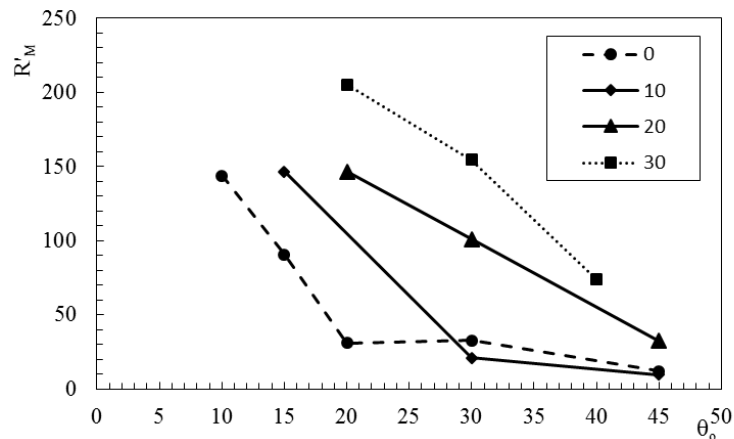


Figure 4.25: Values of R'_M as function of the initial angle between the fire fronts for series in which the slope value remains fixed ($\alpha= 0, 10, 20$ or 30°).

It was noticed that each of these data sets can be well fitted by an exponential function of the type formulated in Equation (53).

$$R'_M = a_1 \cdot e^{-b_1 \cdot \theta_0} \quad 53$$

The values of the parameters a_1 and b_1 for each series of constant slope tests were set and are presented in Table 6. These values were used to create the model defined in 56. The values of b_{1G} were obtained by making the average of a_1 and b_1 respectively.

Table 6: Parameters a_1 , b_1 , and R'_{M0} for the exponential functions of R'_M .

$\alpha(^{\circ})$	$a_1=R'_{M0}$	b_1	R^2
0	211.8	0.066	0.874
10	471.2	0.091	0.943
20	553.4	0.062	0.971
30	618.0	0.051	0.938

The parameter a_1 that we designate as R'_{M0} for each value of the slope angle is the limit value of R'_M when $\theta_0 \rightarrow 0$. The values of R'_{M0} as function of the slope angle α are plotted in Figure 4.26.

The evolution of $R'_{M0}(\alpha)$ can be adjusted (in the range $0^\circ < \alpha < 30^\circ$) by the second order polynomial function given in Equation 54. The correlation is quantified by the parameter $R^2=0.987$, that is an indicator of good fitting of this equation.

$$a_1 = R'_{M\theta} = -0.4867\alpha^2 + 27.61\alpha + 219.79 \quad 54$$

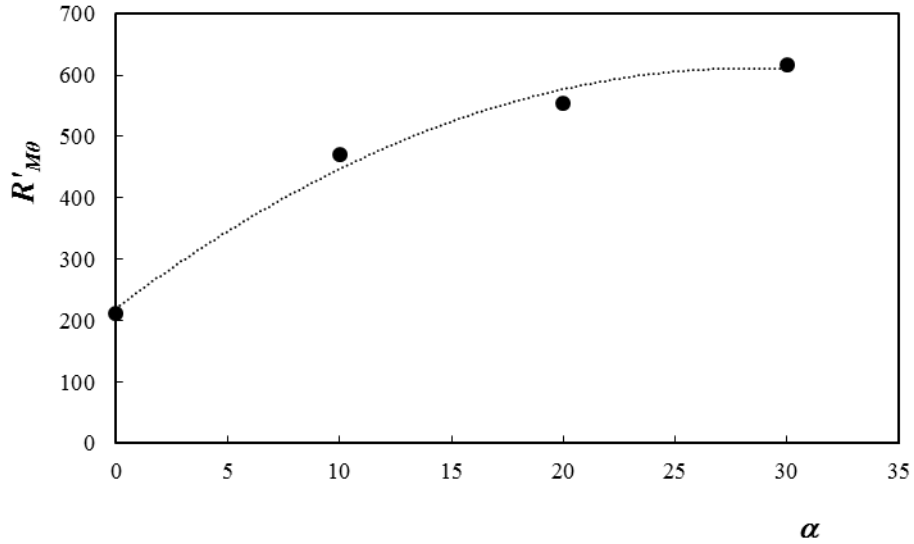


Figure 4.26: The evolution of $R'_{M\theta}$ with α .

The parameter b_I as a function of α was plotted in Figure 4.27. The evolution of b_I (α) shows a decreasing tendency with α can be adjusted by a linear function given in Equation (55). The correlation is quantified by the parameter $R^2=0.320$ that is a low value. This is not very relevant as the value of b_I is practically constant.

The average value of b_I called b_{IG} equal to 0.067 will be used in the development of the model 1.

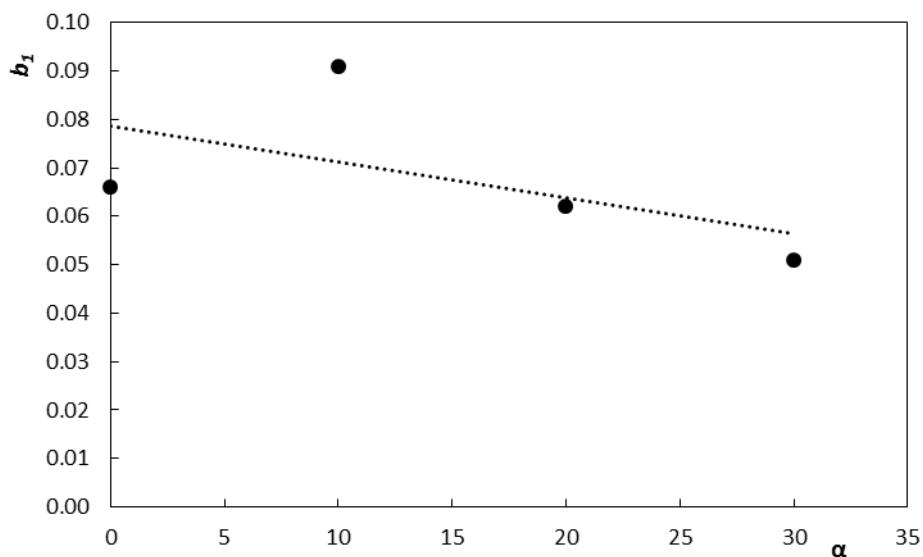


Figure 4.27: Evolution parameter b_1 of the Model 1 with the slope angle α .

$$b_1 = -0.00074\alpha + 0.0786 \quad 55$$

We now introduce the following function ψ_1 defined by:

$$\psi_1 = \left(\frac{R'_M}{R'_{M\theta}} \right)^{\left(\frac{b_{1G}}{b_1} \right)} \quad 56$$

All the other parameters in Equation 56 were defined before.

As can be observed in Figure 4.28 the function ψ_1 follows an exponential law given by 57 that is our model 1 in a normalised form.

$$\psi_1 = e^{-b_1\theta_0} \quad 57$$

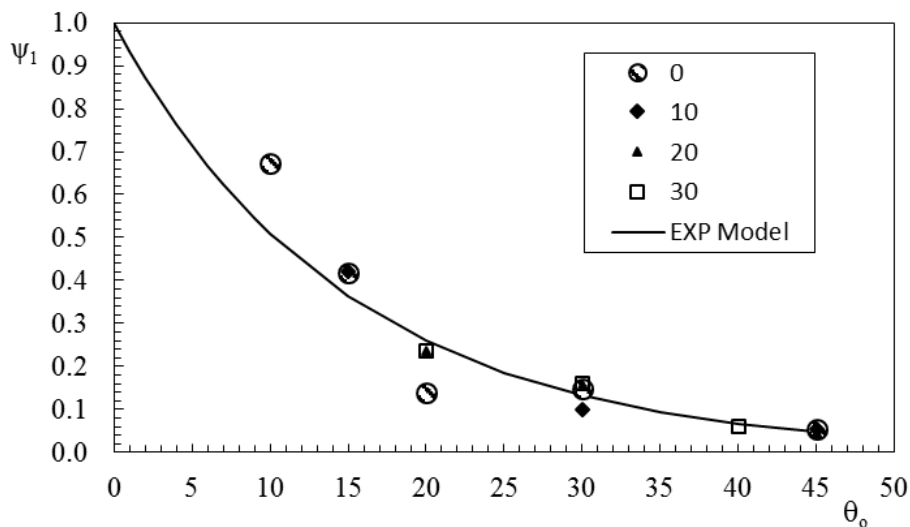


Figure 4.28: Evolution of ψ_1 with the initial angle between the fire fronts θ_0 , for PP , fitted with a negative exponential law.

By the analysis of the data presented in this form it was confirmed that the maximum ROS achieved in a junction fire strongly depends on the angle θ_0 .

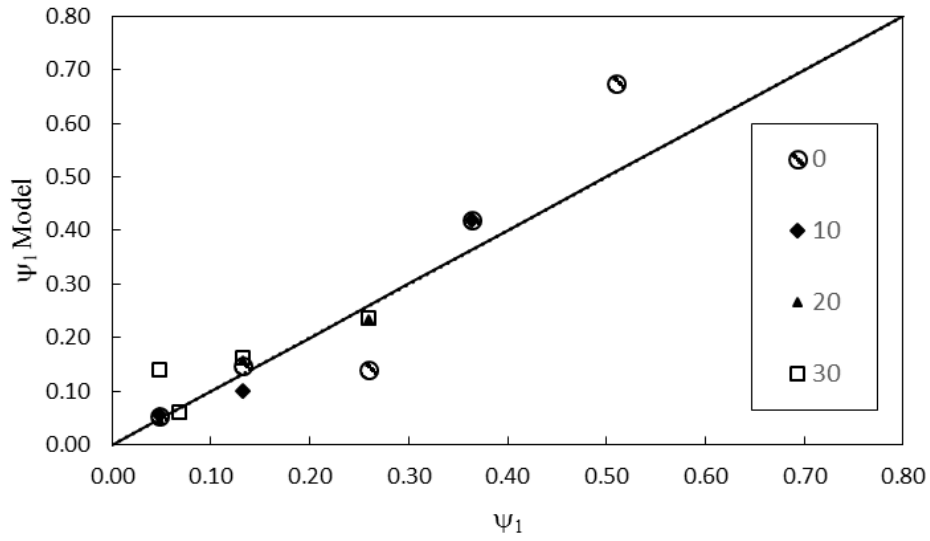


Figure 4.29: Perfect fitting of the values of the model with the ψ_1 experimental data.

The fit between the values of ψ_1 given by Equation (56) and by the model (Equation (57)) are shown in Figure 4.29. The comparison with the perfect fit equation provides a R^2 value of 0.86.

The model 1 defined by Equation (57) can be given in an explicit form as:

$$\begin{aligned}
 R'_M(\alpha, \theta_o) &= \left(e^{-b_1 \alpha \theta_o} \right)^{\left(\frac{b_1}{b_1 \alpha} \right)} \times 219.8 + 27.6\alpha - 0.49\alpha^2 = \\
 &= \left(e^{-0.067\theta_o} \right)^{\left(\frac{-0.00074\alpha + 0.0786}{0.067} \right)} \times 279.8 + 27.6\alpha - 0.49\alpha^2
 \end{aligned} \tag{58}$$

Model 2

Alternatively a relationship between the evolution of the maximum rate of spread R'_M depending on the slope angle α , in series of tests in which the initial angle between the fronts remained fixed ($\theta_o = 15, 20, 30$ and 45°) was analysed, as shown in Figure 4.30.

It was noticed that each data set can be well fitted by a power law function of the type formulated in Equation 61.

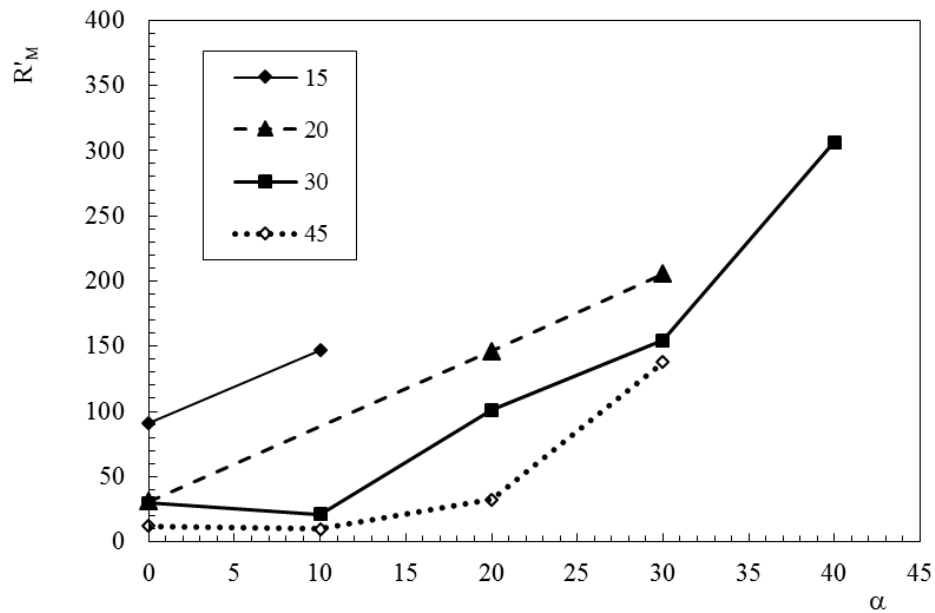


Figure 4.30: Values of R'_M as function of the angle of slope α for series in which initial angle between the value remains fixed ($\theta_o = 15^\circ, 20^\circ, 30^\circ$ or 45°).

It was aimed to approach all the series with a single power law. To do so some mathematical operations were necessary. We defined the auxiliary parameter $R'_{M\alpha}$ that is the value of R'_M for $\alpha=0^\circ$, for each series presented before. In Figure 4.31 the relation between parameters $R'_{M\alpha}$ and α are shown.

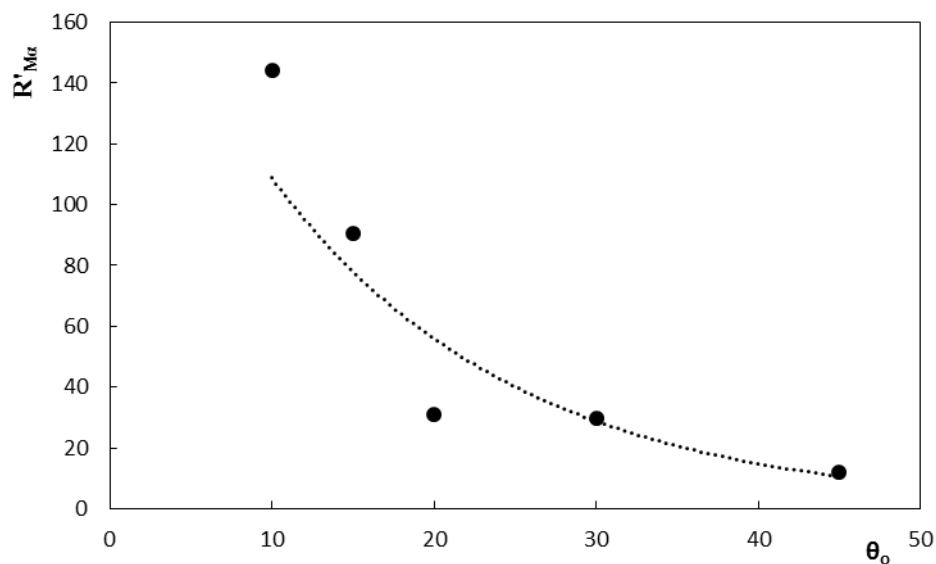


Figure 4.31: $R'_{M\alpha}$ as function of θ_o .

This evolution was fitted by an exponential law as defined by equation (59). The correlation coefficient R^2 for this fitting is 0.879.

$$R'_{M\alpha} = 211.48e^{-0.066\theta_o} \quad 59$$

Now we introduce the function ψ_2 defined by equation (60).

$$\psi_2 = \frac{R'_M}{R'_{M\alpha}} - 1 \quad 60$$

With this formulation all data points are observed to collapse in a single curve that passes through the origin. Negative values of ψ_2 were excluded from the analysis. These values are plotted in Figure 4.32 and can be approached by the following power law:

$$\psi_2 = a_2 \cdot \alpha^{b_2} \quad 61$$

The values of the model parameters $a_2=0.0055$ and $b_2=2.049$ were obtained by the fitting a power law, to the entire set of processed data.

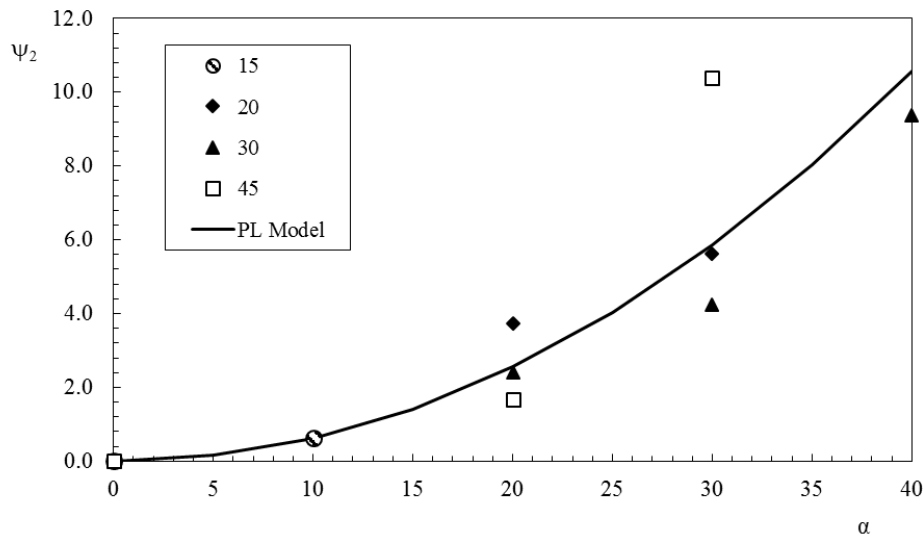


Figure 4.32: Evolution of ψ_2 as function of the initial angle slope α . For series with a fixed initial angle between the fronts ($\theta_o = 15, 20, 30$ and 45°), with fuel *PP*. Fitted with a Power law model.

The Model 2 defined by Equation (61) can be given by the explicit form as:

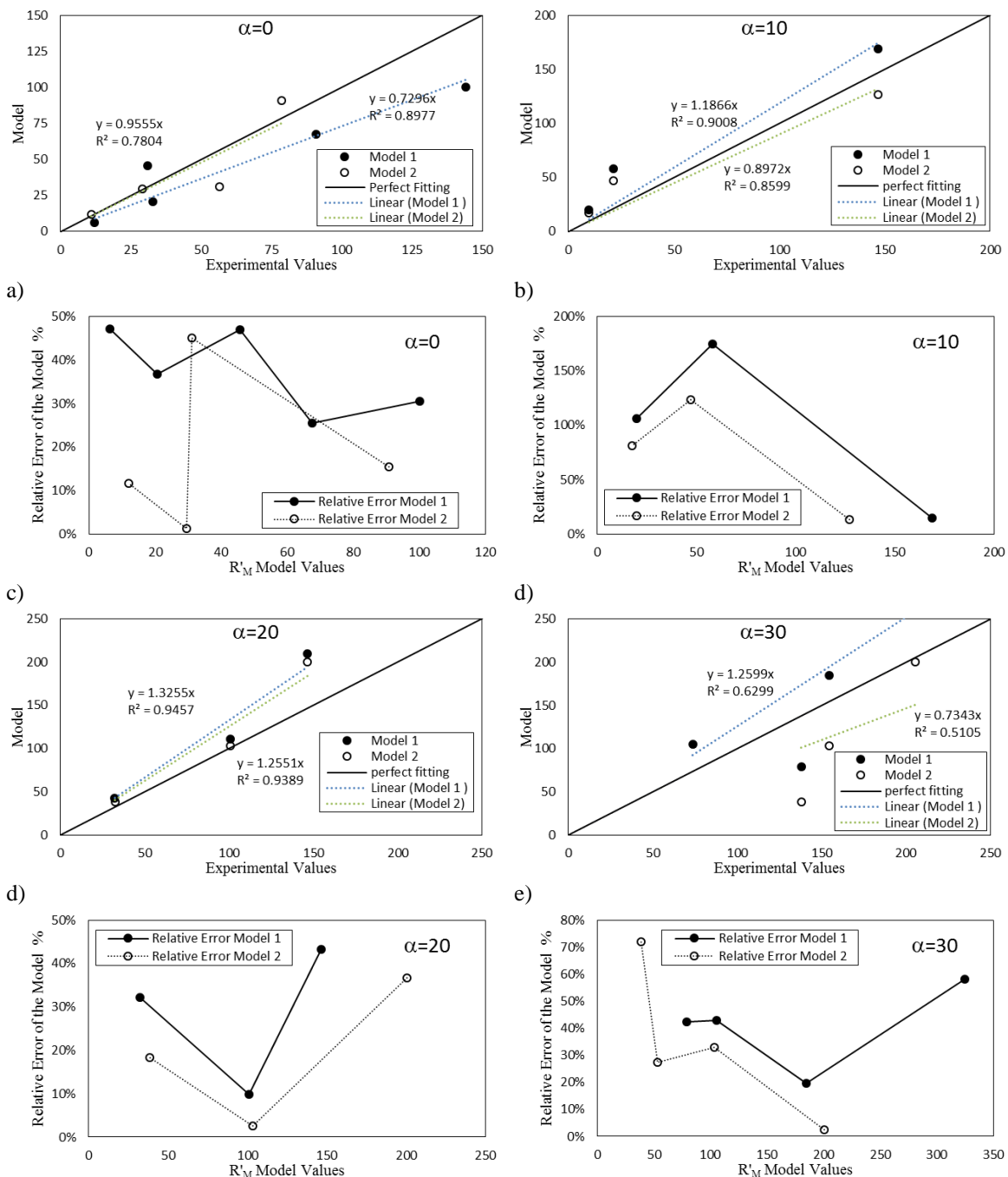
$$\begin{aligned} R'_M(\alpha, \theta_o) &= (a_2 \cdot \alpha^{b_2} + 1) \times 211.48e^{-0.066\theta_o} = \\ &= (0.0055\alpha^{2.049} + 1) \times 211.48e^{-0.066\theta_o} \end{aligned} \quad 62$$

Comparison of the Models

It is expected, that starting from the same source of data the two models should achieve similar results. To confirm this a comparative analysis of perfect fitting between the

experimental data and the estimated data of the models was made. For each angle of slope this representation of the estimated values of the models as a function of the experimental data was made as shown in Figure 4.33. The value of the relative error for each prediction, as defined in Equation (63), is represented below for each plot, for the models 1 and 2.

$$\varepsilon_R (\%) = \frac{\left| (V_{Exp} - V_{Model}) \right|}{V_{Exp}} \times 100 \quad (63)$$



f)

g)

Figure 4.33: Perfect fitting analysis of the models and relative Error assessment.

The value of the reduced R^2 and the relative error average for each model in each configuration are presented in Table 7.

Table 7: R^2 ϵ_R and ϵ_A for each model for different values of α .

α	R^2 value		ϵ_R (%) average	
	Model 1	Model 2	Model 1	Model 2
0	0.898	0.780	37.38	18.35
10	0.901	0.860	98.71	72.78
20	0.946	0.939	28.49	19.22
30	0.630	0.511	40.81	33.70

The models give a good prediction of the junction fire maximum non-dimensional rate of spread R'_M . Models 1 and 2 are very similar as can be observed by the joint representation with the perfect fitting (cf. Figure 4.33 a), b), e) and f)). The values of R^2 show a good correlation between the experimental set of data and the values given by the models, excepting for slope values of 30° to which the correlation coefficient decreases for values lower than 0.7. Anyway model 2 globally presents better values of the relative error that is the parameter that quantifies the quality of the predictions of the model.

The values of the relative error are relatively high especially for values of R'_M lower than 100. For values of R'_M larger than 100 the relative error decreases to values below 50%.

4.8.2. Time t'_M taken until R_M is reached

A model that offers a relationship between the non-dimensional time t'_M taken by the fire fronts to reach the maximum non-dimensional rate of spread R'_M as a function of parameters α and θ_o will be tested.

In Figure 4.34 values of t'_M as a function of θ_o for different conditions of slope angle α are shown. This figure includes the output results of three models.

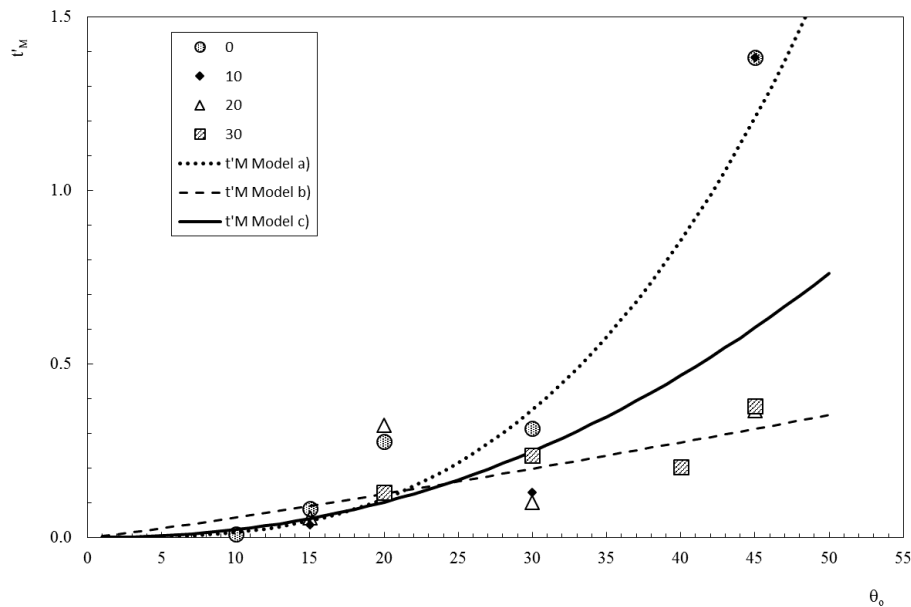


Figure 4.34: Time t'_M as a function of the angle θ_o and the models for this parameter. Models a, b and c corresponds to the parameters of Table 9 used in Equation 64 as following described.

Looking at the experimental data points we realise that t'_M increases strongly with the angle, θ_o , especially for lower values of α . A power law fitting (64) was used to describe the global evolution of the experimental data as a set.

$$t_M = a_3 \cdot \theta_o^{b_3} \quad 64$$

The parameters a_3 and b_3 obtained from the fitting of each series were listed in Table 8.

Table 8: Parameters a_3 and b_3 for different values of α .

$\alpha(^{\circ})$	a_3	b_3	R^2
0	0.000014	3.054	0.92
10	0.000006	3.138	0.90
20	0.004055	1.138	0.36
30	0.005642	1.055	0.79

Since the values of a_3 and b_3 show some similarities between sets it was decided to group the experimental data in three groups according the α values and determine the new parameters and statistical parameters for the merged groups of data (Table 9). The representation of the fitting curves can be found in Figure 4.34.

Table 9: Parameters a_3 and b_3 for the three groups of data.

Set	Group of α values	a_3	b_3	R^2	Mean $\varepsilon_r(\%)$
a)	(0 and 10 $^{\circ}$)	0.0000170	2.935	0.88	184.89
b)	(20 and 30 $^{\circ}$)	0.00429	1.127	0.46	152.37

c)	(0,10, 20 and 30°)	0.000142	2.195	0.70	150.85
----	--------------------	----------	-------	------	--------

Groups a) and c) allowed to create models that have a good correlation between the experimental data points (for the different slope conditions) and the data provided by the models as confirmed by the good values of R^2 of the order of 0.88 and 0.70 respectively. On the other hand the group b) showed a bad correlation between the data as described by the low value of R^2 equal to 0.46.

The model derived from group c) was adopted due to its lower value of the mean relative error. In this way the model adopted for t'_M is the following.

$$t'_M = 0.000142 \times \theta_o^{2.195} \quad 65$$

The curve of the model of t'_M obtained with this function corresponds to the one plotted in Figure 4.34 with a bold line.

The model reproduces the evolution of experimental data points quite well. Only for values of θ_o equal to 45° in the series of $0 < \alpha < 10^\circ$ a wider gap from the model curve in relation to the experimental points exist.

4.8.3. Distance x'_M until R'_M is reached

A model to predict the tendency of the non-dimensional distance x'_M travelled by the intersection point D of the fire fronts up to reach the maximum rate of spread R'_M as a function of the parameters α and θ_o will be proposed just as an indicative of the tendency for this parameter.

This formulation assumes that the value of x'_M must be proportional to the product of the rate of spread R'_M by the time t'_M , as expressed by Equation (66).

$$x'_M \sim R'_M \cdot t'_M \quad 66$$

Substituting R'_M by the formulation of Model 1 (Equation 58) and t'_M by the expressions achieved in Equation (64) we will find the Equation (67) for x'_M . Notice that alternatively the Model 2 could have been used as well.

$$x'_M \sim \left(e^{-0.067\theta_o} \right)^{\left(\frac{-0.00074\alpha + 0.0786}{0.067} \right)} \times 279.8 + 27.6\alpha - 0.49\alpha^2 \times \left(0.000142 \times \theta_o^{2.195} \right) \quad 67$$

The input value for α used in this equation was the average value of 15° , although other values in the range of the slopes tested could be used. To adjust the model of x'_M to the experimental data points, of Figure 4.35, a constant k_x was used. Through the best fitting between the experimental data points and the values of the model the k_x value was set in Equation (68) in 43, maximizing the R^2 and minimizing the ϵ_R , ($R^2=0.0375$ and $\epsilon_R=390.48$). If different values of α were used the process would remain the same and only the value of k_x could be different. In this way the model used to approximate x'_M to the experimental data it was:

$$x'_M = k_x \cdot R'_M \cdot t'_M \quad 68$$

In the Figure 4.35 the curve of the model for x'_M with the experimental data points as a function of θ_o was plotted.

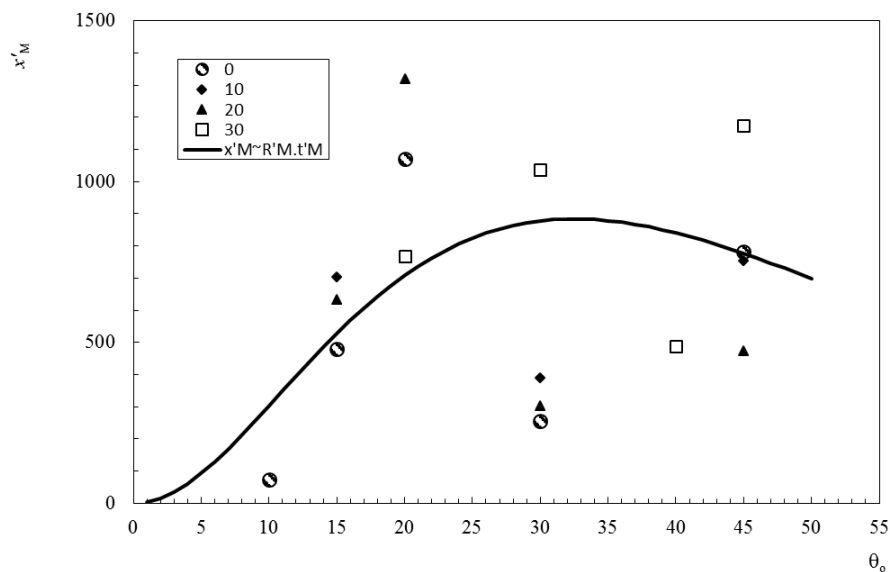


Figure 4.35: Model for the distance x'_M as function of the angle θ_o and experimental data.

The analysis of the data plotted contrast from the previous ones, because these do not reveal a monotonic trend of evolution with the angle θ_o . This difference of behaviour is explained by the fact of the R'_M decreases exponentially with the angle between the fire fronts θ_o but in the opposite direction the time t'_M increases with θ_o , the tendency curve proposed put this in evidence.

The tendency curve given by the model has its maximum for values of the angle θ_o of 30° the differences between the model and the experimental data points can be attributed to the fact of that x'_M was simply described by the direct relation of the two parameters time and rate of spread. A second factor is the very sensitive response of the model to the input parameters.

4.8.4. Analytical Model Formulation

Based on the results obtained in the previous points an empirical model of prediction of the evolution of the rate of spread as a function of time $R^*(t^*)$ or as function of distance $R^*(x^*)$ for junction fires is presented in Figure 4.36.

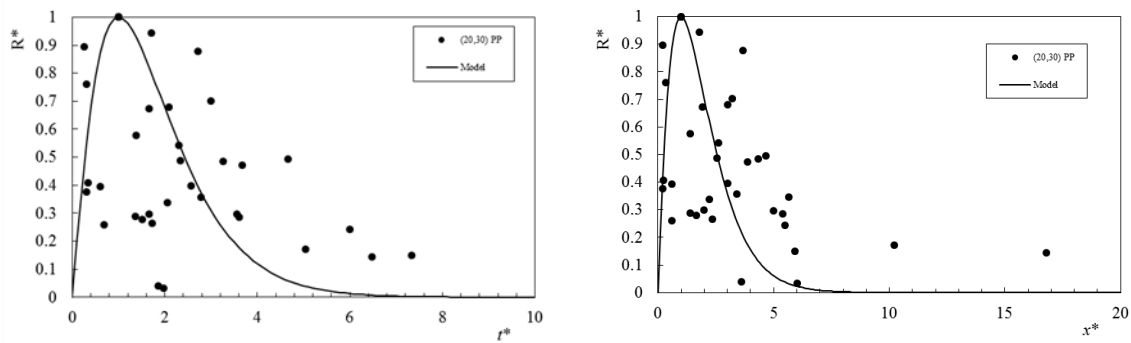


Figure 4.36: Exemplificative figures of the evolution of R^* as function of t^* or x^* .

From the analysis of the overall evolution of the data points for $R^*(x^*)$ or $R^*(t^*)$ shown in Figure 4.36 it was realised that they can be expressed by a function of the type:

$$y = x^a \cdot e^{b(1-x^c)} \quad (69)$$

This function should satisfy the following conditions:

$$x=1 \rightarrow y=1 \quad \text{and} \quad x=1 \rightarrow y'=0$$

The second condition imposes the following relationship between the three parameters:

$$a = b \cdot c$$

As a consequence only two of the three parameters of Equation (69) are free. Moreover due to the reduced number of data points that we dispose it was chosen to limit the number of parameters of the model to a single one. To do that the value of b was set equal to 1 from which results that $a=c$. Therefore the model adopted will be the following:

$$y = x^a \cdot e^{(1-x^a)} \quad (70)$$

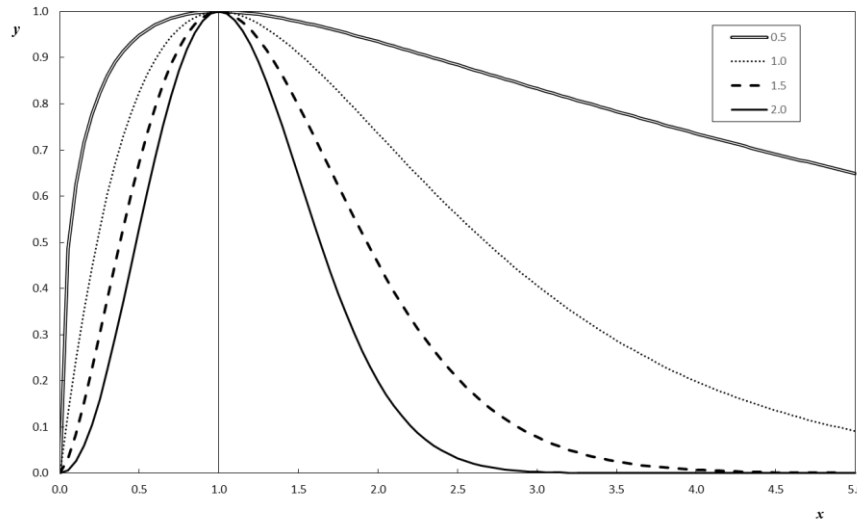


Figure 4.37: Tuning of the mathematical model for different values of the parameter a .

In Figure 4.37 several curves were plotted to illustrate the evolution of the curve through the parameter a . As can be observed for lower values of a , the values of the function y increases rapidly as function of x to values of x close to zero. For values of x larger than 1 the function decreases slowly. When the value of the parameter a increases the values of the function increases more slowly in the initial phase and decreases more rapidly for values of x larger than 1.

The models has two formats one for R^* as function of t^* and other in function of x^* as is proposed below:

$$R^*(t^*) = t^{*A} \cdot e^{(1-t^{*A})} \quad 71$$

$$R^*(x^*) = x^{*B} \cdot e^{(1-x^{*B})} \quad 72$$

It was decided to adopt the letter A when the model of R^* is defined as function of time t^* and to use the letter B when model of R^* is expressed as a function of x^* to designate the parameter previously denominated as a in the general function expressed by Equation (70).

Slope effect

The first set of plots presented assess the fitting of the model for different values of slope (0, 10, 20, 30 and 40°) for tests with initial angle θ_0 fixed in 30° and with fuel PP , as function of t^* .

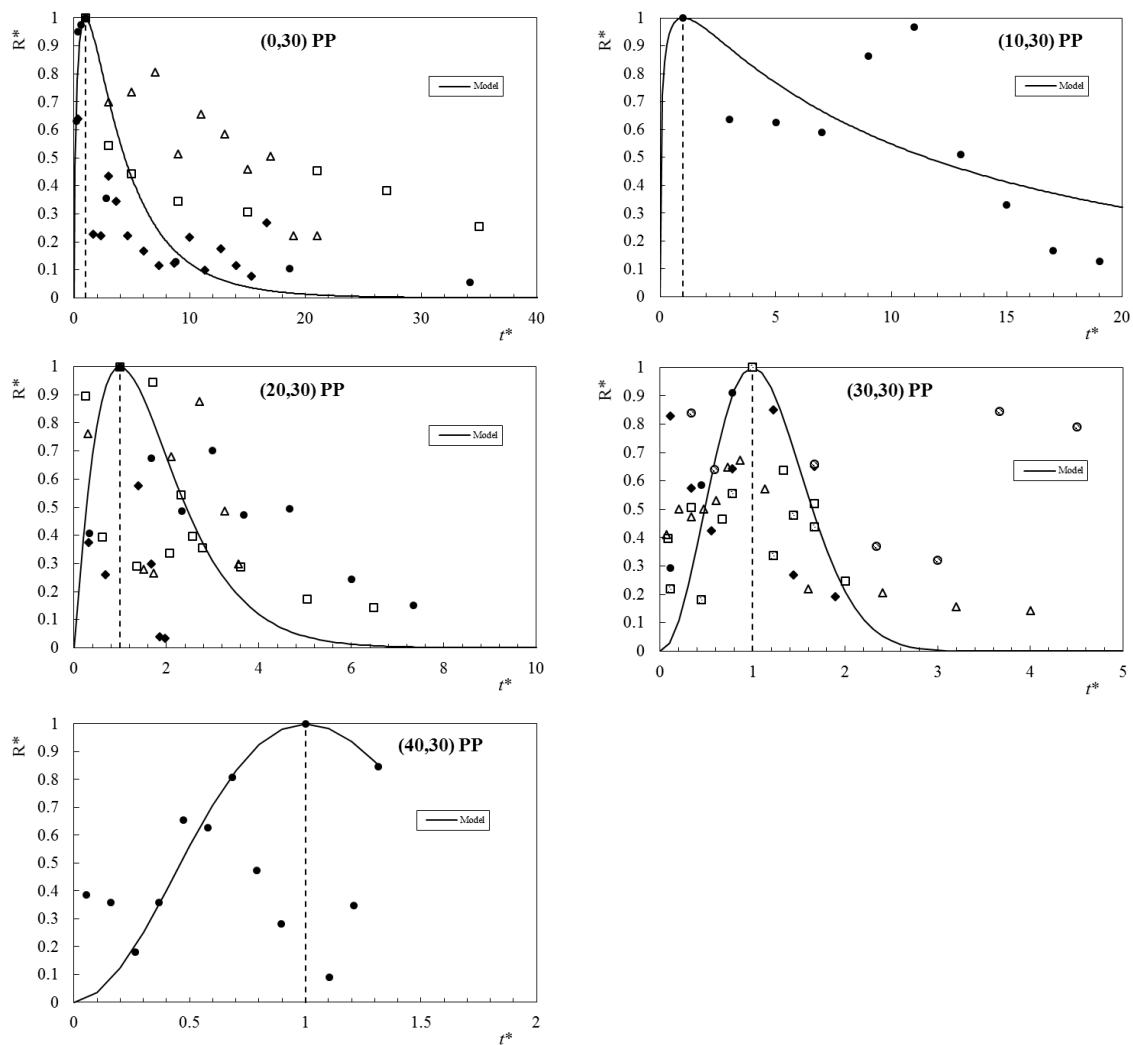


Figure 4.38: Fitting of the model curve, for different values of slope ($0, 10, 20, 30$ and 40°), for the case of tests with initial angle θ fixed in 30° and with fuel **PP**, as function of the non-dimensional time t^* .

By the analysis of the set of plots of the Figure 4.38, it is possible to realise that as previously seen the different slope conditions lead to different evolutions of the curves of the rate of spread $R^*(t^*)$. In the cases with small slopes the acceleration phases are shorter and the deceleration phases are longer. For higher slopes the acceleration phases are well defined and relatively wider and the deceleration phases are shorter or does not exist at all. Nevertheless the proposed empirical model proved to be able to adapt itself and predict satisfactorily each of these situations only changing the single parameter in a short range. For the curves of $R^*(x^*)$, for different slope conditions, the same can be observed (Figure 4.39).

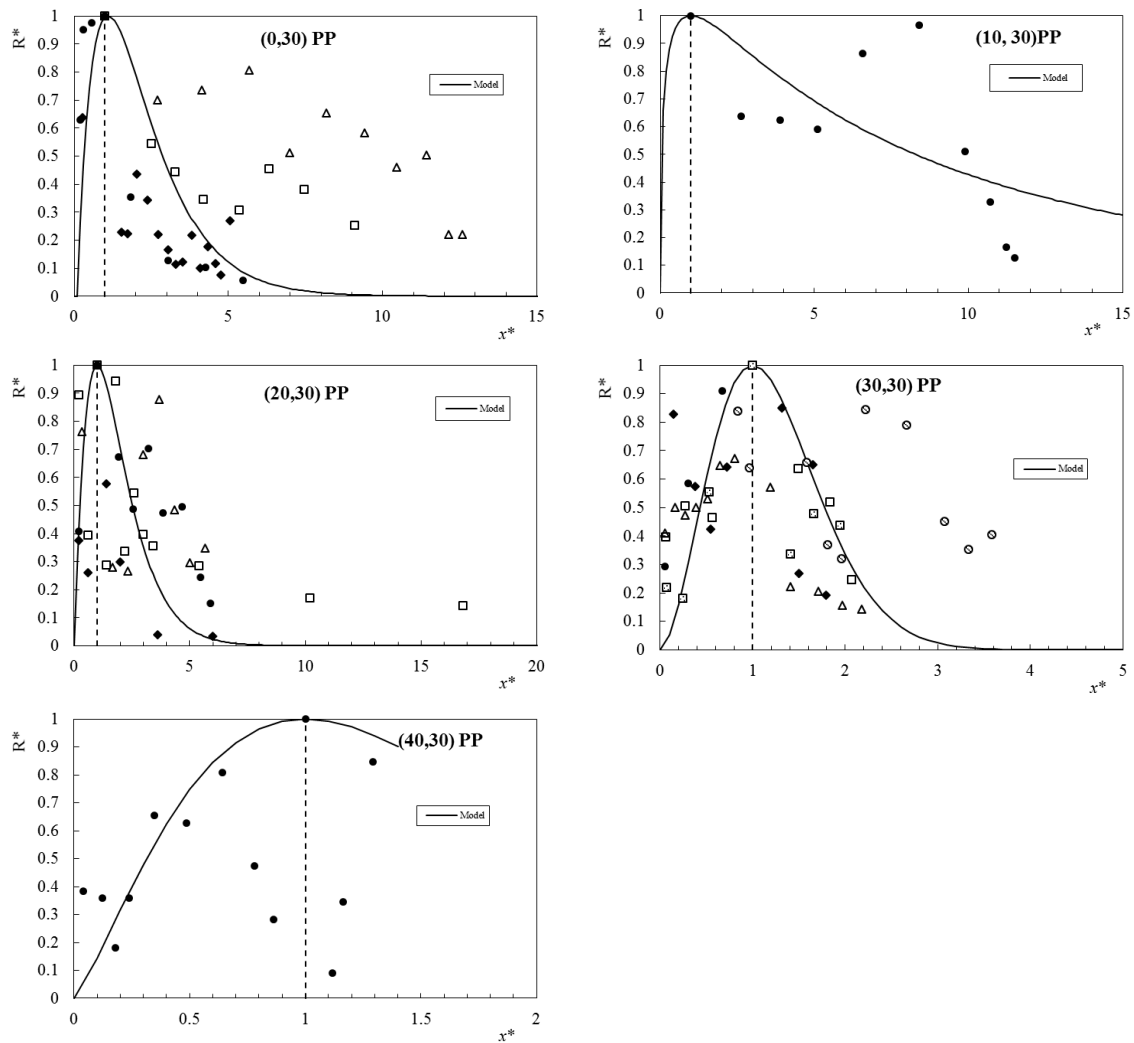


Figure 4.39: Fitting of the model curve, for different values of slope (0, 10, 20, 30 and 40°), for the case of tests with initial angle θ_0 , fixed in 30° and with fuel PP, as function of the non-dimensional time x^* .

The values of the parameters A and B for the data points plotted above are given in the

Table 10 and shown in Figure 4.40. A similar behaviour of the two parameters A and B can be observed in this figure.

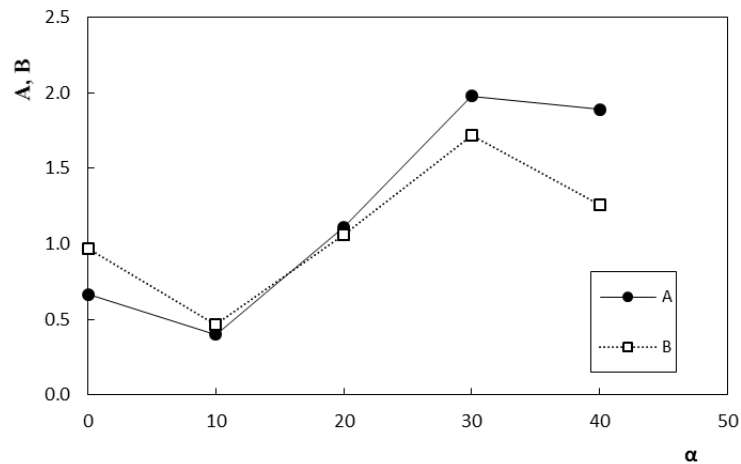


Figure 4.40: Comparison of the fitting parameters values of A and B as function of the slope (0, 10, 20, 30 and 40°) for plots in function of t^* and x^* respectively.

Table 10: Variation of A , B and statistical parameters for the cases presented in the Figure 4.38 and Figure 4.39.

α	A	B	A $\epsilon_R(\%)$	B $\epsilon_R(\%)$	N° of points
0	0.66	0.97	68.72	82.68	55
10	0.40	0.47	34.74	52.19	10
20	1.11	1.06	69.96	79.28	36
30	1.98	1.72	58.24	54.49	40
40	1.89	1.26	92.36	96.77	16

In order to assess the goodness of the proposed model the statistical value of the relative error (ϵ_R) (André 2008) was assessed.

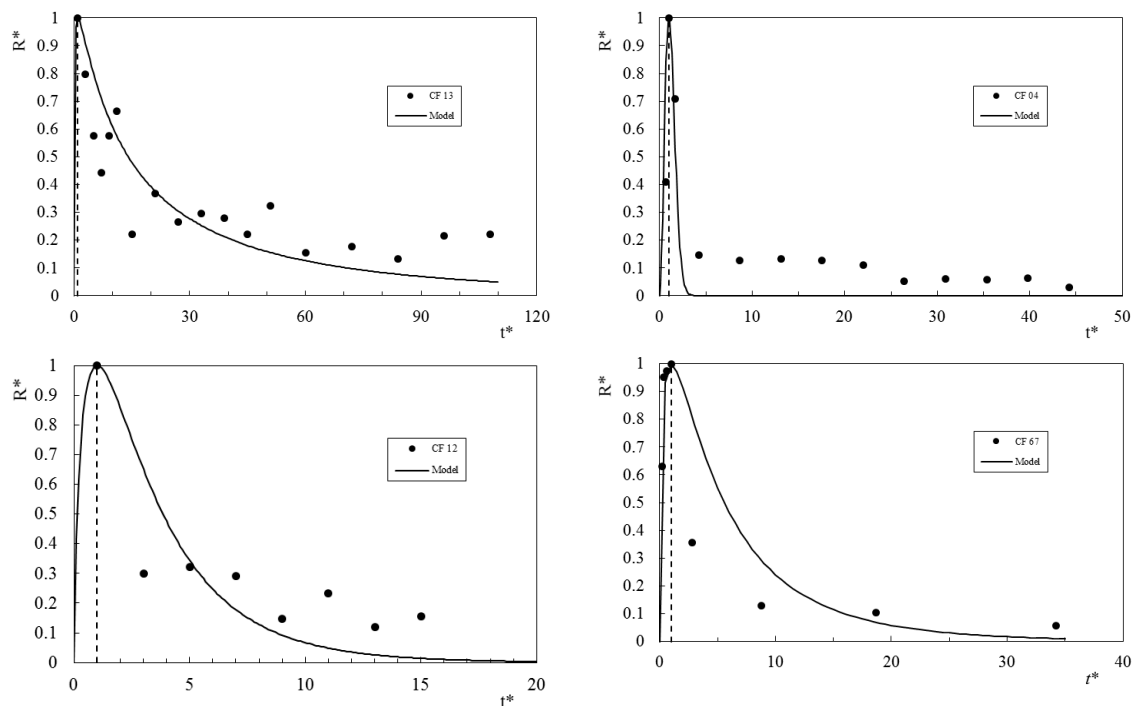
An assessment of relation between the model and the experimental data is firstly given by the visual inspection of the plots of these data. However this qualitative assessment is not enough and so a quantitative assessment of the goodness of the model can be made determining the average value of ϵ_R that gives the quality of adjustment of the model to the experimental data. A good fit was achieved for the chosen parameters which minimize the deviations of the model curve to the experimental points (André 2008). As ϵ_R quantifies the

deviation of predicted values from the actual values if there is no deviation (perfect fitting) then ϵ_R tends to 0. By the analysis of the values of ϵ_R presented in

Table 10 it is possible to see that the adjustment of the model is poor for this set of experimental data. The large number of tests and points create a larger dispersion of the data that can explain these high values. Although this dispersion does not seem to be random but it results also from the simplification of considering the decreasing phase through a simply decreasing law, while the data show some fluctuations in that phase.

Initial angle effect

A similar analysis is now presented for R^* with a slope $\alpha=0^\circ$ and changing the value of the initial angle between the fire fronts θ_0 . This analysis is presented in Figure 4.41 and Figure 4.42 for time t^* and distance x^* respectively. The fuelbed of the tests in analysis was *PP*.



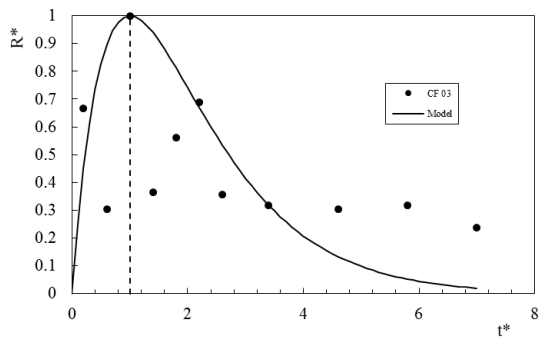


Figure 4.41: Fitting of the model curve with fuel type **PP** and the slope angle fixed in 0° for different values of initial angle between the fire fronts, ($\theta_0 = 10, 15, 20, 30$ and 45°) respectively from left to right and from top to down. As function of t^* .

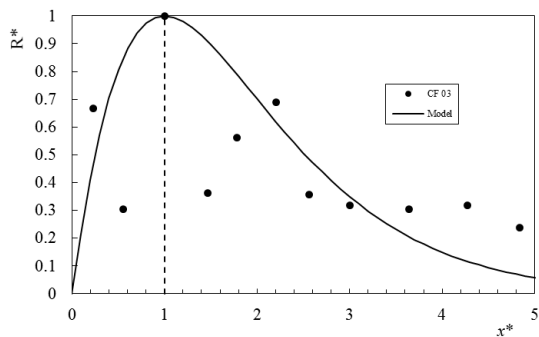
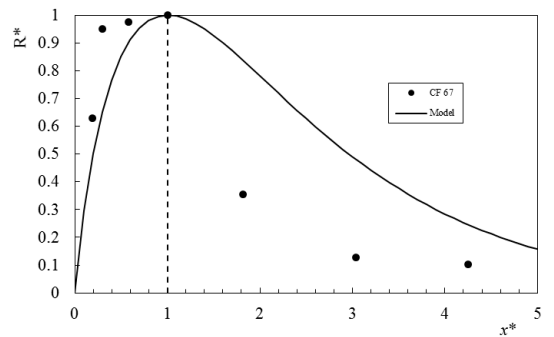
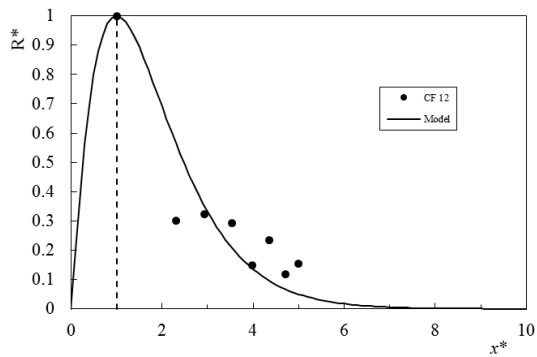
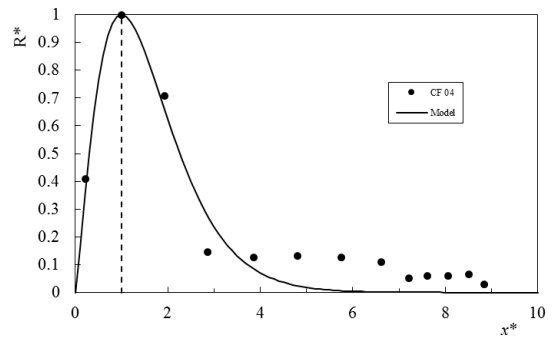
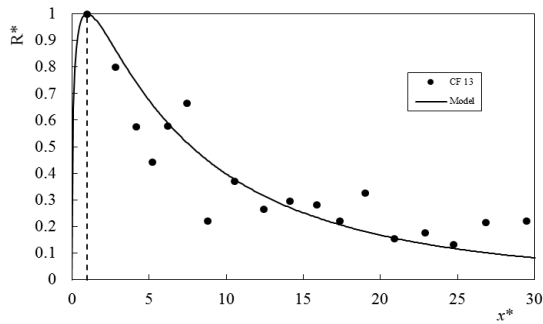


Figure 4.42: Fitting of the model curve with fuel type **PP** and the slope angle fixed in 0° , for different values of initial angle between the fire fronts, θ_0 , ($10, 15, 20, 30$ and 45°) respectively from left to right and from top to down. As function of x^* .

The variations in the experimental data on the rate of spread R^* for different values of angle θ_0 were well described by the empirical model proposed. The values of A and B and the statistical parameters that allowed this conclusion, for the data of the Figure 4.41 and Figure 4.42, are given in the Table 11 and are shown in Figure 4.43.

Table 11: Variation of A , B and statistical parameters for the cases presented in the Figure 4.41 and Figure 4.42.

θ_0	A	B	A $\varepsilon_R(\%)$	B $\varepsilon_R(\%)$	N° of points
10	0.37	0.48	61.50	25.29	18
15	1.81	1.20	66.13	70.09	13
20	0.73	1.09	56.06	38.09	8
30	0.57	0.91	68.72	82.68	8
45	0.99	1.07	87.93	57.02	11

The values of ε_R are in general quite high although lower than in previous cases. The values of ε_R for this formulation as a function of the initial angle θ_0 are of 50% in average. Some exceptions were registered in two cases with values of ε_R larger than 70%.

By the analysis of Figure 4.43 we concluded that the values of A and B have is maximums for θ_0 equal to 15° with no large differences between them. The variation of these parameters of the model with the increment of θ_0 is not monotonic. This correspond well to the different shapes of the curves obtained for each angle condition.

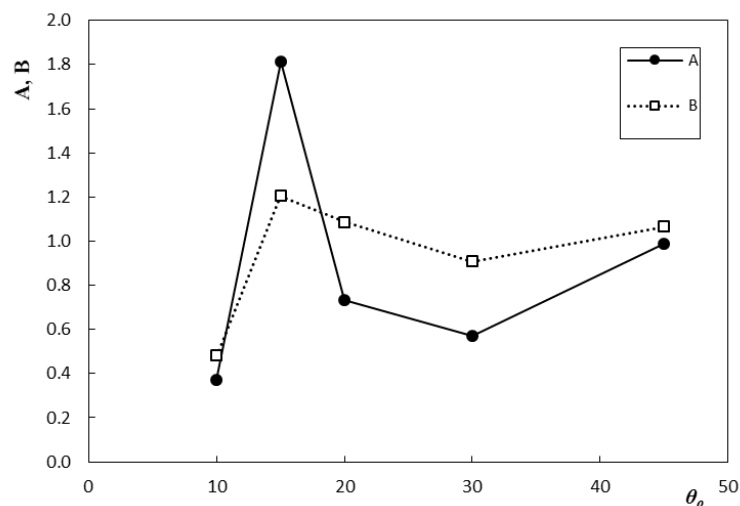


Figure 4.43: Comparison of the values of A and B for the curves with fuel type PP, the slope angle fixed in 0° , for different values of initial angle between the fire fronts, θ_0 .

Fuels effect

For the set of tests with the same parameters but with different fuels the same model was applied and a similar analysis was performed. The method used to compare the model of $R^*(t^*)$ or $R^*(x^*)$ was applied to the different fuels. This analysis was limited to the cases in which the initial angle $\theta_0 = 30^\circ$, because it is the only case for which we have tests with different values of α for the three fuels. The data points and the model curve for the $\alpha=20^\circ$ are shown in Figure 4.43 for each fuel. A similar analysis was performed for the other values of α and the corresponding values of parameters A and B as well as variable statistics are given in Table 12.

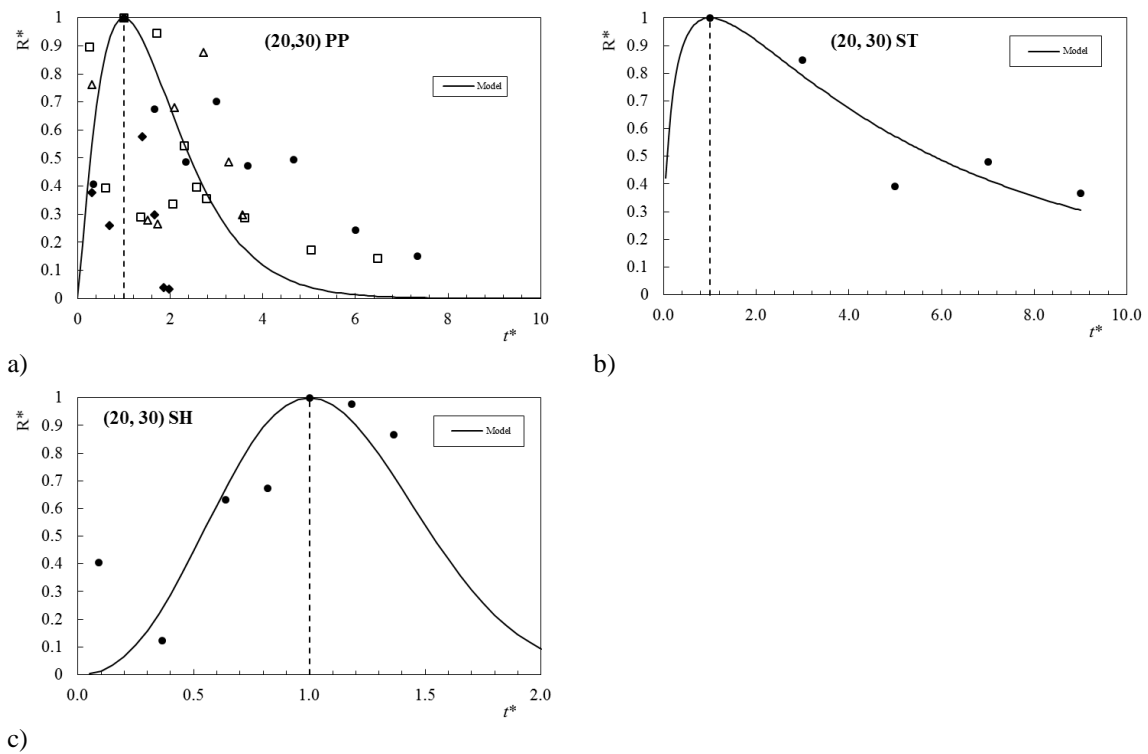


Figure 4.44: Fitting of Model of R^* for the slope angle $\alpha=20^\circ$ with $\theta_0= 30^\circ$ as function of t^* for the three fuels: a) *PP*, b) *ST* and c) *SH*.

The values of parameter A which are contained in the range from 0.3 to 2.4 for each fuel are compared between them and with the average value of the three fuels in Figure 4.45. As expected from previous analysis no large differences were registered between the fuels tested with the value of A increasing with θ_0 for the three fuels. An exception was registered for the point correspondent to 20° of slope, with the fuel type *SH*, which can be considered as an outlier, as all the other points are very coherent between them.

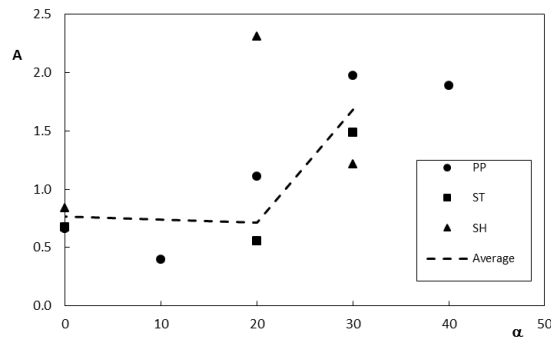


Figure 4.45: Comparison of the values of A as function of the slope (0, 10, 20, 30 and 40°) for the case of tests with initial angle, θ_0 , fixed in 30° for the 3 different fuels. The average values are represented in a dotted line

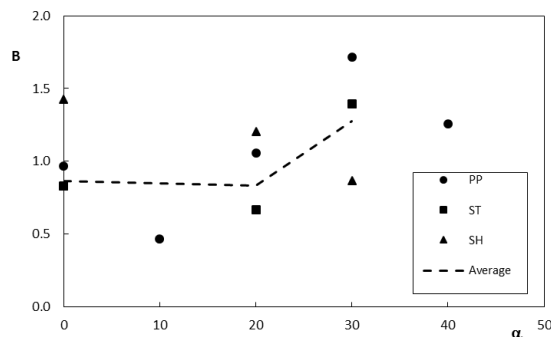


Figure 4.46: Comparison of the values of B as function of the slope (0, 10, 20, 30 and 40°) for the case of tests with initial angle θ_0 fixed in 30° for the 3 different fuels. The average values are represented in a dotted line.

The values of parameter B that are in the range from 0.5 to 2 (Figure 4.46) show a tendency of increase with θ_0 with the exception of the data points corresponding to shrubs SH which show a decreasing evolution.

Table 12: Parameters A and B for each fuel and statistical data.

<i>SH</i>					
α	A	B	A $\epsilon_R(\%)$	B $\epsilon_R(\%)$	N° of points
0	0.84	1.43	62.32	75.77	27
20	2.31	1.21	36.23	45.55	9
30	1.22	0.87	16.19	39.29	6
<i>PP</i>					
α	A	B	A $\epsilon_R(\%)$	B $\epsilon_R(\%)$	N° of points
0	0.66	0.97	68.72	82.68	55

10	0.40	0.47	34.74	52.19	10
20	1.11	1.06	69.96	79.28	36
30	1.98	1.72	58.24	54.49	40
40	1.89	1.26	92.36	96.77	16
ST					
α	A	B	A Reduced R ²	B Reduced R ²	N° of points
0	0.68	0.83	41.80	75.52	11
20	0.56	0.67	16.70	13.38	5
30	1.49	1.40	13.64	28.11	5

The values of ϵ_R registered that allows to assess the goodness of the model to fit the rate of spread R^* as a function of t^* or x^* for the different fuels are in the same ranges of the previous ones analysed. Although we can affirm that the values of the relative error are more satisfactory for the cases with SH and ST what reveals a better precision of the prediction of the model for these fuels.

Scale effect

In section 4.5 two plots (Figure 4.17 a) and b)) of the evolution of R^* as function of t^* and x^* for different scales (laboratory, field and real fires), with the fuel SH, were already shown. Applying the present model to those cases the values of the fitting parameters **A** and **B** that are given in Table 13 and shown in Figure 4.47 and Figure 4.48 were obtained.

Table 13: Fitting parameters A and B and statistical parameters.

<i>Test</i>	<i>Scale</i>	<i>Length Scale (m)</i>	A	B	A $\epsilon_R(\%)$	B $\epsilon_R(\%)$	<i>N° of points</i>
CF 56	Lab.	5	1.22	0.865	16.19	39.29	6
CF77	Field	34.79	2.393	2.486	34.09	29.34	10
CF78	Field	27.09	0.944	0.959	37.55	39.90	6
CF79	Field	59.66	1.957	1.475	35.43	28.38	6
CF80	Canberra	15800	0.973	1.102	9.44	43.68	3

Despite the small variations it was observed that the values of **A** and **B** are contained in a short range (between 0.5 and 2.6) that is the same that was observed before.

The goodness of the fitting of the model was highlighted by the low values of ϵ_R for the majority of the tests that reveals a good precision even for larger scales of analysis (cf. Table 13).

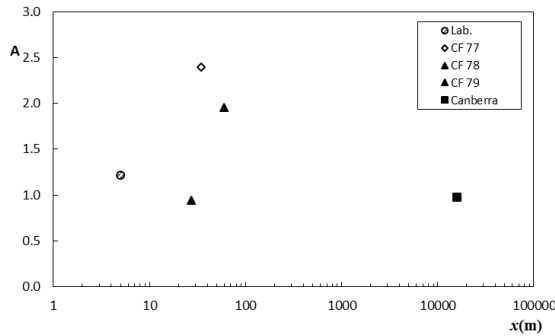


Figure 4.47: Fitting parameter A evolution for different scale lengths with SH as fuel.

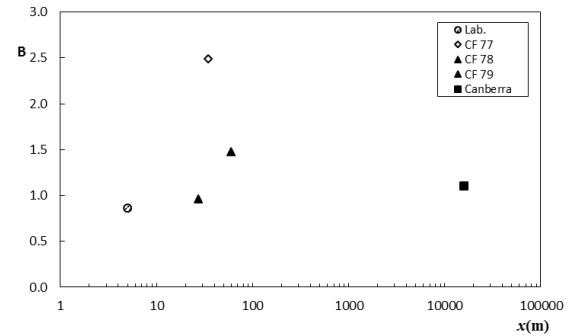


Figure 4.48: Fitting parameter B evolution for different scale lengths with SH as fuel.

From the analysis of Figure 4.47 and Figure 4.48 it was concluded that there is no trend of evolution of the parameters A or B with the length scale of the fire. The values of A and B for the different scales are in the same range of those reported previously.

4.9. General discussion

In this section the aspects that affect the junction fires behaviour and the results achieved will be discussed as a synthesis.

Following the structure of presentation used previously about this type of fires in this chapter the first topic to be discussed is the overall fire front evolution.

The section 4.1 presents the pattern of spread of two fire fronts, in a V shape, by isochrones lines, constructed from the IR images. From these images we can see that in junction fires the advance of the fire is due to the rapid advance of the intersection point D of the two lines. As a consequence the two fire lines rotate tending to be aligned one with the other. The speed of rotation of the fire lines is essentially negative due to the strong convection induced the fire front.

The major part of the study is dedicated to the analysis of the evolution of the intersection point D , due to its large rate of spread. Two complementary techniques employing IR images and thermocouples were used to evaluate its fire spread. Both can be used to assess the evolution of point D but as IR provides data on the overall evolution of

the entire fire front this technique was preferred in the analysis. From these data the characteristic curves of spreading for different initial boundary conditions were constructed. These curves show an acceleration phase followed by a deceleration phase the duration and magnitude of each phase depends of their initial or boundary conditions. This behaviour of the rate of spread is like the signature of the junction fire.

In section 4.2 the effect of the terrain slope on the rate of spread was reported and analysed. It was observed that the maximum value of R_D increases with the slope angle α and the same happens with the distance x_M or time t_M that is required to reach it. The influence of slope in the increasing phase is very high. For no slope conditions the increasing ROS phase is very short and the decreasing phase is prevalent. For the medium slope of 20° both phases are reported more or less with the same extension in time as well as in space. With the slope equal or greater than 30° the acceleration phase is dominant and the deceleration phase is almost meaningless or non-existent due to the limited length of the fuelbed. It was considered that the atmospheric wind has a similar effect on R_D as slope.

Through the analysis of three different fuels (*Pinnus pinaster*; *Avena sativa*; and shrubs composed by a mix of *Erica umbelatta*, *Erica australis*, *Ulex minor* and *Chamaespartium tridentatum*) the effect of fuels on junction fires was evaluated. Despite of the differences between the fuels the overall fire behaviour was found to be the same for all of them with a similar evolution of the ROS curves.

Non dimensional parameters were used to put in evidence the similar behaviour of junction fires for a range of fuels and boundary conditions. The use of R_M , x_M and t_M as characteristic parameters was adopted to develop an overall mathematical model.

On the analysis of the effect of the initial angle between the fires fronts θ_0 it was found that the maximum rate of spread R_D was reached for lower values of θ_0 and decreased for larger values, in all the range of slope conditions tested.

In the present work a wide range of space and time scales from laboratory tests, with few meters, passing by field trials on a scale of tens of meters to the Canberra fire with a scale of thousands of meters were considered. This is a particular strong point of this work, the consideration of fires at multiple scales which helps to support the relevance of laboratory scale measurements. This shows that the phenomena of junction fires is not dependent on the scale of the fire as its geometrical configuration is defined by an angle that is a non-dimensional parameter.

In order to better understand the physical processes associated to the two phases of evolution of the junction fire a study of the convection and the radiation associated to the fire was performed.

For the study of convective processes, the analogy between the acceleration phase and the eruptive model was made. This hypothesis was tested, together with the referred model. It was observed that the acceleration of the fire occurred in time intervals comparable with the ones provided by the eruptive model.

The measurements of the field of velocity of the flow along the propagation axis of the point D, showed the existence of a strong flow favourable to the advance of the fire front at this point. With the evolution of the fire front and consequent alteration of its geometry, an entrance of a flow in the opposite direction of propagation was allowed that produces a gradual deceleration on the advance of the intersection point.

For the acceleration phase the data presented supported the assumption that initial acceleration of the fire must be due to convective flow induced by the fire in the same manner as for eruptive fires.

The junction fires induced flow velocity that will increase the rate of spread, until the flow reaches a maximum value and then starts to decrease and can blows in the opposite direction reducing the rate of spread of the fire.

For the deceleration phase, the hypothesis that the evolution of the process is governed by radiative processes was stated. This hypothesis implies a linear relationship between the rate of spread and the radiative flux emitted by the fire front. This only occurs in the final deceleration phase. This is a result of the strong convective activity that is observed in the initial phase of deceleration.

An analytical global model, forecasting the evolution of rate of spread $R^*(x^*)$ or $R^*(t^*)$ that depends of R'_M , t'_M e x'_M and partial models for each one of these parameters were developed.

For the parameter R'_M two models (Model 1 and Model 2) were proposed to describe the evolution of this parameter through the variables slope and angle between the fronts. These two models are independent of the fuel used in the tests. Although the process of construction of the models have some differences the Model 1 and 2 are very similar between them. A good fitting to the experimental data is provided by both models. However, Model 2 has a relative error slightly lower than Model 1.

For the parameter t'_M a power law model as a function of the parameters θ_o was proposed, for the all the slope conditions studied. The R^2 of this model to the data points was of 0.46.

Through a relation between the model for R'_M (Model 1) and the model for t'_M the x'_M parameter was approximated. The model to predict only the tendency of x'_M was based on the assumption that the distance x'_M is proportional to the product of R'_M by t'_M .

This is a non-monotonic function of the angle θ_o , as the experimental data points confirmed. This behaviour is explained by the fact of the R'_M decreases exponentially with the angle between the fire fronts θ_o but in the opposite direction the time t'_M increases with θ_o .

An analytical model with a single parameter with two formulations: $R^*(t^*)$ and $R^*(x^*)$ as defined by Equations 71 and 72 were proposed. Both formulations were applied to situations with different values of α and θ_o with acceptable results as indicated by mainly good values of ϵ_R registered, with some exceptions as discussed. The model parameter values A and B (respectively for $R^*(t^*)$ or $R^*(x^*)$) remained stable and similar between them, with a small variation range (from 0.5 to 2.6), even when applied to conditions of different fuels and length scales in the range of the present experiments.

It was not included in the scope of the present study the analysis of junction fire scenarios in which the influence of wind or complex topography are the initial conditions.

Chapter 5.

Conclusions

In this study a particular form of extreme fire behaviour that consists in the merging of two fire lines that intersect making a small angle between them, and that is characterised by an initial phase of acceleration in which very high values of ROS are reached followed by a deceleration phase was analysed. We proposed the designation of junction fire to this form of fire behaviour.

The main parameters that govern the development of junction fire were described and the dynamic behaviour of the fire was put in evidence. It was shown that in the case of having symmetrical boundary conditions the analysis of the advance of the intersection point D of the two fire lines is adequate to describe the overall properties of the junction fire. It is observed that the rate of advance of this point can reach extremely high values, the highest that have been recorded in our laboratory or field experiments with similar fuels and in real fires as well.

The work was essentially based in experimental laboratory tests in which the type of fuel (burning fuelbeds of pine needles PP, straw ST and shrubs SH) the slope of the fuelbed (from 0 to 40°), the initial angle between the fire fronts (for 10°, 15°, 20°, 30° and 45°) were varied in the indicated ranges. These laboratory tests were complemented with data from field scale tests and a large scale fire. It was found that the junction fire behaviour is similar at all tested scales with small dependence on the fuel bed and on the initial boundary conditions with the exception of the initial angle between the fire lines.

The maximum value of the ROS R_M , the duration t_M of the acceleration phase and the distance x_M travelled by the fire before it reaches its maximum ROS were identified as being relevant parameters in the analysis of the junction fire. It was found that R_M , t_M and x_M values increase with slope of the fuelbed and decrease with the initial angle between the fire fronts.

The acceleration phase of the junction fire was associated to the convective flow developed by the fire due to the high concentration of energy near the intersection point of the fire lines. It was shown that in this acceleration phase the fire develops like an eruptive fire but afterwards it is inhibited by a contrary flow that reduces the advance of the fire front. The deceleration is associated to convection and radiation effects. Using the concept of propagation flux it was shown that only in the final stage of fire deceleration it is acceptable to assume that radiation from the flames is the main mechanism of fire spread.

Different empirical models were proposed to estimate the non-dimensional parameters R'_M , t'_M , x'_M and also an analytical model for the evolution of the non-dimensional ROS $R^*(t^*)$ or $R^*(x^*)$ depending on a single parameter that varies in a limited range for the entire set of experimental data.

As future work more research has to be carried out to explore this important mode of extreme fire behaviour. Experimental tests at laboratory scale to better understand the physical processes involved are required namely considering systematically the roles of wind, of non-symmetric conditions and of a wider set of configurations as for example other values of initial angle between the fire fronts, slope and for complex topographies (canyons).

Measurements of flow velocity at more points are required to better understand the very complex convective flow induced by junction fires.

The radiation measurements near the fire fronts should be extended to validate the simulations performed. Also improvements in the numerical simulations of the radiant flux can be done extending them to slope conditions and through a better description of the flames characteristics as for example their tilt angle or the shape, among others.

Field scale experiments and real fire analysis should be performed in order to extend the range of data points and fill the gap mentioned in the scale analysis.

The analytical model for R^* should be improved through validation with more cases and the development of a physical model using analytical and numerical computational simulation should be attempted.

References

- Alexander ME, Cruz MG (2011) What are the safety implications of crown fires?
International Association of Wildland Fire, Missoula, Montana, USA 4–8.
- Almeida M (2011) Fire Spread by spotting. Doctoral Thesis. University of Coimbra.
- Anderson HE (1969) Heat transfer and fire spread. *USDA Forest Service, Intermountain Forest and Ranger Experiment Station, Research Paper INT–RP–69*.
doi:10.5962/bhl.title.69024.
- André JCS (2008) ‘Probabilidades e Estatística para Engenharia.’ (Lidel)
- André JCS, Gonçalves JC, Vaz GC, Viegas DX (2013) Angular variation of fire rate of spread. *Int. J. Wildl. Fire* **22**, 970–979. <http://dx.doi.org/10.1071/WF12028>.
- Byram GM (1959) Some Principles of Combustion And Their Significance In Forest Fire Behaviour. *Reprinted from: Fire Control Notes* **18**, 47–57.
- Chandler C, Cheney P, Thomas P, Trabaud L, Williams D (1983) ‘Fire in forestry. Volume 1. Forest fire behavior and effects.’ (John Wiley & Sons, Inc.: New York)
- Cruz MG, Butler BW, Alexander ME, Forthofer JM, Wakimoto RH (2006) Predicting the ignition of crown fuels above a spreading surface fire. Part I: model idealization. *Int. J. Wildl. Fire* **15**, 47–60. <http://dx.doi.org/10.1071/WF04061>.

- Doogan M (2006) The Canberra Firestorm Inquests and Inquiry into Four Deaths and Four Fires Between 8 and 18 January 2003. (ACT)
- Dupuy JL, Maréchal J, Portier D, Valette JC (2011) The effects of slope and fuel bed width on laboratory fire behaviour. *International Journal of Wildland Fire* **20**, 272–288. doi:10.1071/WF09075.
- Ellis PF (2000) The Aerodynamic and Combustion Characteristics of eucalypt bark. A Firebrand study. Department of Forestry Australian National University.
- Figueiredo R, Costa J, Raimundo A (2015) ‘Transmissão de Calor - Fundamentos e Aplicações.’ (LIDEL: Coimbra)
- Finney M a., McAllister SS (2011) A review of fire interactions and mass fires. *Journal of Combustion* **2011**,. doi:10.1155/2011/548328.
- Frankman D, Webb BW, Butler BW, Jimenez D, Forthofer JM, Sopko P, Shannon KS, Hiers JK, Ottmar RD (2013) Measurements of convective and radiative heating in wildland fires. *International Journal of Wildland Fire* **22**, 157–167. doi:10.1071/WF11097.
- Incropera FP, Bergman TL, Lavine AS, Dewitt DP (2011) ‘Fundamentals of Heat and Mass Transfer.’ (L Ratts, Ed.). (John Wiley & Sons, Inc.: United States of America)
- Johansen RW (1984) Prescribed Burning with Spot Fires in the Georgia Coastal Plain. *Georgia Forestry Commission* **49**, 1–8. <http://www.treesearch.fs.fed.us/pubs/36481>.
- Johansen RW (1987) Ignition patterns and prescribed fire behavior in southern pine forests. *Georgia Forestry Commission Forest Research* **72**, 6 p.
- Mendes-Lopes JC, Ventura JP, Amaral JP (2003) Flame characteristics, temperature-time

-
- curves, and rate of spread in fires propagating in a bed of *Pinus pinaster* needles. *International Journal of Wildland Fire* **12**, 67–84. doi:10.1071/WF02063.
- Morvan D, Meradji S, Mell WE (2011) Numerical study of the interaction between a head and a backfire propagating in grassland. *Fire Safety Science* **10**, 459–470. doi:10.3801/IAF.
- Pastor E, Agueda A, Andrade-Cetto J, Muñoz M, Pérez Y, Planas E (2006) Computing the rate of spread of linear flame fronts by thermal image processing. *Fire Safety Journal* **41**(8), 569-579. doi:10.1016/j.firesaf.2006.05.009.
- Pyne SJ (1984) 'Introduction to wildland fire: Fire Management in the United States.' (John Wiley and Sons: New York)
- Pyne SJ, Andrews PL, Laven RD (1996) 'Introduction to wildland fire.' (John Wiley and Sons: New York)
- Quintiere JG (2006) 'Fundamentals of Fire Phenomena.' (John Wiley & Sons: Maryland) doi:10.1002/0470091150.
- Raposo J, Viegas DX, Xie X, Almeida M, Naian L (2014) Analysis of the jump fire produced by the interaction of two oblique fire fronts: Comparison between laboratory and field cases. 'Adv. For. Fire Res.' pp. 23–30. (Coimbra)
- Rossa CG (2009) Dynamic Model For Fire Behaviour Prediction. Doctoral Thesis. Coimbra.
- Rothermel RC (1972) A Mathematical Model for Predicting Fire Spread In Wildlan Fuels. *Forest Service -US Department of Agriculture* INT-115.
- Sardoy N, Consalvi JL, Porterie B, Fernandez-Pello AC (2007) Modeling transport and combustion of firebrands from burning trees. *Combustion and Flame* **150**, 151–169. doi:10.1016/j.combustflame.2007.04.008.
-

- Schemel CF, Simeoni A, Biteau H, Rivera JD, Torero JL (2008) A calorimetric study of wildland fuels. *Experimental Thermal and Fluid Science* **32**, 1381–1389. doi:10.1016/j.expthermflusci.2007.11.011.
- Sharples JJ, McRae RHD, Wilkes SR (2012) Wind-terrain effects on the propagation of wildfires in rugged terrain: Fire channelling. *International Journal of Wildland Fire* **21**, 282–296. doi:10.1071/WF10055.
- Tarifa CS, Notario P, Moreno F (1965) On the flight paths and lifetimes of burning particles of wood. *Symposium (International) on Combustion* **10**, 1021–1037. doi:10.1016/S0082-0784(65)80244-2.
- Viegas DX (1997) Convective Processes in Forest Fires. In ‘NATO Adv. Study Inst. Buoyant Convect. Geophys. Flows’, Pforzheim, Germany.(Pforzheim, Germany)
- Viegas DX (2002a) Fire Behaviour Models : An Overview. In ‘fuoco For. Ecol. e Control. Atti del XXXIX Corso di Cult. Ecol.’, 37–47
- Viegas DX (2002b) Fire line rotation as a mechanism for fire spread on a uniform slope. *International Journal of Wildland Fire* **11**, 11–23. <http://www.publish.csiro.au/paper/WF01049>.
- Viegas DX (2006b) Parametric study of an eruptive fire behaviour model. *Int. J. Wildl. Fire* **15**, 169–177. <http://dx.doi.org/10.1071/WF05050>.
- Viegas DX (2006a) Parametric study of an eruptive fire behaviour model. *International Journal of Wildland Fire* **15**, 169–177. doi:10.1071/WF05050.
- Viegas DX (2012) Extreme Fire Behaviour. ‘For. Manag. Technol. Pract. Impact’. (Eds ACB Cruz, REG Correa) pp. 1–56. (Nova Science Publishers, Inc.: New York)

-
- Viegas DX, Almeida M, Miranda AI, Ribeiro LM (2010) Linear model for spread rate and mass loss rate for mixed-size fuel beds. *International Journal of Wildland Fire* **19**, 531–540. doi:10.1071/WF09007.
- Viegas DX, Pita LP (2004) Fire spread in canyons. *International Journal of Wildland Fire* **13**, 253–274. doi:10.1071/WF03050.
- Viegas DX, Raposo JR, Davim D a., Rossa CG (2012) Study of the jump fire produced by the interaction of two oblique fire fronts. Part 1. Analytical model and validation with no-slope laboratory experiments. *International Journal of Wildland Fire* **21**, 843–856. doi:<http://dx.doi.org/10.1071/WF10155>.
- Viegas D, Raposo J, Figueiredo A (2013) Preliminary analysis of slope and fuel bed effect on jump behavior in forest fires. *Procedia Engineering* **62**, 1032–1039. doi:10.1016/j.proeng.2013.08.158.
- Viegas DX, Rossa C (2009) Fireline Rotation Analysis. *Combustion Science and Technology* **181**, 1495–1525. doi:10.1080/00102200903228891.
- Viegas DX, Rossa C, Ribeiro LM (2011) ‘Incêndios Florestais.’ (DX Viegas, Ed.). (Verlag Dashöfer Edições profissionais Unip., Lda.: Lisboa)
- Van Wagner CE (1968) Fire behaviour mechanisms in a Red Pine plantation: field and laboratory evidence. (Ottawa, Canada)
<http://cfs.nrcan.gc.ca/publications/?id=24753>
<http://cfs.nrcan.gc.ca/publications/download-pdf/24753>.
- Wong K-FV (2003) ‘Intermediate Heat Transfer.’ (CRC Press)
- Xie X, Liu N, Viegas DX, Raposo JR (2014) Experimental Research on Upslope Fire and Jump Fire. In Grant CE, Pagni PJ (eds) ‘Fire Saf. Sci. Proc. Elev. Int. Symp.’, 1–13.
-

(Fire Safety Science-Draft Proceedings of the Eleventh International Symposium)

http://www.iafss.org/publications/fss/11/221/view/fss_11-221.pdf.